Silicon Photonic PAM-4 Modulators for Next Generation Intra-Data Center Optical Communication Systems

Rui Li

Department of Electrical & Computer Engineering
McGill University
Montréal, Québec, Canada

March 2018

A thesis submitted to McGill University in partial fulfillment of the requirements for the degree of Doctor of Philosophy

To Mrs. Hong Li, my mother

and

In memory of Mrs. Guoying Wang and Mr. Jinping Li, my grandparents

About the Author

Rui Li received the B.Eng. degree in optical engineering and a Chu Kochen honors degree for top 5% students from Zhejiang University, Hangzhou, China, in June 2013. Since September 2013, she joined the Photonic Systems Group in the department of Electrical and Computer Engineering at McGill University, as a research assistant where she is currently working towards the Ph.D. degree under the supervision of Prof. David V. Plant.

Her current research interests include high-speed silicon photonics modulators for intra-data center applications and intensity-modulation/direct-detection short-reach transmission systems. She has 5 first-author peer-reviewed journal papers and 3 conference papers, including 1 invited talk at the 2017 Conference on Laser and Electro-Optics. Besides, she has co-authored 5 peer-reviewed journal papers and 6 conference papers. She regularly serves as a reviewer for Optics Express, Optics Letters, Photonics Research and other peer-reviewed journals. She also served as the president of Optical Society of America McGill Chapter from October 2015 to November 2016.

Miss Li is a recipient of 2015 – 2018 Silicon Electronic Photonic Integrated Circuits (SiEPIC) scholarship, a recipient of 2015 – 2018 Pervasive and Smart Wireless Applications for the Digital Economy (PERSWADE) scholarship, and a recipient of 2016 and 2017 McGill Graduate Research Enhancement and Travel (GREAT) Awards. She was also awarded the 2013 – 2016 McGill Engineering International Tuition Awards (MEITA). In addition, she was awarded the outstanding undergraduate thesis of Optical Engineering in 2013, excellent students award in 2011 and the first-class scholarship for top 3% students in 2010 from Zhejiang University. When she was an exchange student in the University of Hong Kong from 2011 to 2012, she was awarded the Li & Fung scholarship and Fung scholar fellowship.

Abstract

In recent years, high-speed low-cost modulators have attracted immense research interest to fulfill the ever-increasing intra-data center traffic. Silicon photonics is a mature platform compatible to the complementary metal-oxide-semiconductor fabrication processes, and it has a low cost for large volume integration. Intensity-modulation/direct-detection systems do not need a local oscillator or complicated digital signal processing (DSP), thus they are favored over coherent systems for intra-data center applications. Currently, four-level pulse amplitude modulation (PAM-4) has been accepted for the next generation 400G Ethernet.

In this thesis, two silicon photonic PAM-4 modulators are reported for the next generation intra-data center optical communication systems. They are the dual microring modulators (MRMs) assisted Mach-Zehnder interferometer (MZI) and the dual-drive Michelson interferometric modulator (MIM). Three operating principles of generating PAM-4 optical signals based on the two proposed modulators are investigated. First, by driving the dual MRMs with differential 4-level radio-frequency (RF) signals, low-chirp PAM-4 is achieved. Successful PAM-4 transmission at 92 Gb/s over 1 km of standard single mode fiber (SSMF) and at 40 Gb/s over 20 km of SSMF without chromatic dispersion compensation are presented. Second, based on the resonances overlap of the two microrings and modulation of only one MRM, PAM-4 with large optical modulation amplitudes and extinction ratios are realized. 80 Gb/s PAM-4 transmission over 2 km of SSMF is successfully achieved. Third, dual-drive operation with independent binary RF signals generates PAM-4 optical signals without implementing digital-to-analog converter or DSP, which reduces the power consumption in the optical transmission link. PAM-4 transmission over 2 km of SSMF at 50 Gb/s using the dual MRMs assisted MZI and at 56 Gb/s using the dual-drive MIM are both presented. All the measured bit error rates of PAM-4 transmission based on these three operating principles are below the hard-decision forward-error correction threshold of 3.8×10^{-3}.

Résumé

Au cours des années, les modulateurs haut vitesse à bas coût ont suscité un immense intérêt en recherche, afin de répondre au trafic toujours croissant dans les centres de données. La photonique sur silicium est une plateforme mature compatible avec les procédés de fabrication CMOS, ayant de plus un bas coût pour une intégration à grand volume. Les systèmes à modulation d'intensité et détection directe n'ont pas besoin d'un oscillateur local ou d'un traitement de signal numérique (DSP) compliqué, ils sont donc préférés aux systèmes cohérents pour les applications intra centre de données. Actuellement, la modulation de l'amplitude d'impulsion à 4 niveaux (PAM-4) a été acceptée pour la prochaine génération d'Ethernet 400G.

Dans cette thèse, deux modulateurs PAM-4 sur la plateforme photoniques sur silicium sont étudie pour la prochaine génération de systèmes de communication optique intra centre de données. Ils sont l'interféromètre Mach-Zehnder (MZI) assisté par deux modulateurs en anneaux (MRMs) et le modulateur interférométrique de Michelson (MIM) à double entraînement. Trois principes de fonctionnement pour la génération de signaux optiques PAM-4 sont étudiés, tous basés sur les architectures deux modulateurs proposés. Tout d'abord, en modulant les deux MRMs avec des signaux radio-fréquence (RF) différentiels à 4 niveaux, PAM-4 à bas bruit est attaint. La transmission PAM-4 à 92-Gb/s sur 1 km de fibre monomode standard (SSMF) et à 40-Gb/s sur 20 km de SSMF sans compensation de dispersion chromatique sont présentés avec succès. Deuxièmement, sur la base du chevauchement des résonances des deux anneaux et de la modulation d'un seul MRM, PAM-4 à grande amplitude de modulation optique et à rapport d'extinction élevé est réalisé. La réussie transmission PAM-4 à 80-Gb/s sur 2 km de SSMF est atteinte. Troisièmement, le fonctionnement à double entraînement avec des signaux RF binaires indépendants est utilisé pour génèrer des signaux optiques PAM-4 sans recours à un convertisseur numérique-analogique ou DSP, ce qui réduit la consommation d'énergie dans le lien de transmission optique. La transmission PAM-4 sur 2 km de SSMF à 50-Gb/s en utilisant le MZI assisté par deux MRMs et at à 56−Gb/s en utilisant le MIM à double entraînement est

présenté. Tous les taux d'erreurs sur les bits mesurés pour la transmission PAM-4 basés sur ces trois principes de fonctionnement sont inférieurs 3.8×10^{-3}.

Acknowledgments

First and foremost, I would like to thank my supervisor, Prof. David V. Plant, for his academic guidance and constant encouragement since I joined the Photonic Systems Group (PSG) in September 2013. To me, he is not only a supervisor, but also a respectable mentor and a supportive friend. Without him, I wouldn’t have such a wonderful and successful experience working towards a Ph.D. degree. I still remember when I was worried about my research and cried in December 2014, he encouraged me and told me that everyone was unique; when I was confused about the following work I could do in November 2015, he shared with me his views on the future of integrated optical devices; when my first two journal papers got rejected in January 2017, he discussed with me how to write a good paper; and when I was invited for a talk at CLEO, he was happy for me and even more excited than me. These moments are meaningful to me, and they have shaped my life. I would also like to express my appreciation to his generosity in sending me to the conferences and his support in every decision I made. I am privileged to be his student.

I would like to express my gratitude to my colleagues, who are talented and offered great help to my research. Many thanks to *Mr. David Patel* for his patient help in building up the experimental setups and fruitful discussions. He teaches me how to use the test beds, gives me a lot of instructive advice on designing modulators, writing papers and response letters. Many thanks to *Mr. Alireza Samani* for his helpful suggestions on ideas, meaningful assistance in experiments, warm-hearted encouragement and useful recommendations on my future career path. Many thanks to *Mr. Eslam El-Fiky*, who is enthusiastic and supportive to me. He not only helps me a lot on my research, but also gives me valuable advice in life. I would also like to thank *Dr. Qunbi Zhuge*, he lights up my view on optical transmission systems and helps me a lot on the general orientation of my research. In the past four and a half years, I have received countless help from the people in PSG, who are not mentioned here. The list is long and I am grateful to all of them.

I would like to express my deepest love and gratefulness to *Mrs. Hong Li*, my mother, for her unconditional love in my entire life. To me, she is a role-model, teaching me how to struggle in the hard times and how to keep calm in the good times. She is my motivation to be a better person every day. I would also like to thank my father, *Mr. Hong Liu*, for his continuous support and encouragement, which warms me when I feel depressed. Also, many thanks to my elder sister *Mrs. Xiaoming Liu*, for her accompany and help in life.

I would also thank *Lulu*, my cute cat. She makes my life more relaxed and helps me go through the hard days.

Last but not the least, I would like to express my deepest missing to my passed grandparents, *Mrs. Guoying Wang* and *Mr. Jinping Li*. They gave me everything they had and made me feel beloved. Their tender love and the good memories are my life-long treasure. I feel that they are shining stars in the sky, watching me and blessing me every day.

This thesis is dedicated to my mother, and in memory of my grandparents.

Sincerely,

Rui Li

March 2018

Associated Publications

This thesis represents my original research, and it has not been submitted for a degree or diploma at any other institution. The work presented within this thesis is entirely my own, except where references are made. Permissions on reprinting figures and tables from the cited references have been obtained from both the Optical Society of America (OSA) and Institute of Electrical and Electronics Engineers (IEEE). Based on their copyright policies, appropriate attributions are maintained and copyright lines appear prominently with every reprinted figure and table.

The content in this thesis is organized based on my 8 first-authored publications, including 5 published journal papers [1-5], 1 invited talk [6], 2 published conference proceeding [7, 8]. In addition, I also have 5 co-authored journal papers [9-13] and 6 co-authored conference proceedings [14-19] through the collaboration with my colleagues in the Photonic Systems Group at McGill University.

Journal Articles Directly Related to This Thesis

[1] **R. Li**, D. Patel, E. El-Fiky, A. Samani, Z. Xing, Y. Wang, and D. V. Plant, "Silicon photonic dual-drive MIM based 56 Gb/s DAC-less and DSP-free PAM-4 transmission," Opt. Express **26**(5), 5395-5407 (2018).

I conceived the idea, performed the simulation and analysis, conducted the experiments, and wrote the paper. The co-authors contributed in revising the manuscript.

[2] **R. Li**, D. Patel, A. Samani, E. El-Fiky, Z. Xing, L. Xu, and D. V. Plant, "Analysis and experimental study of a silicon photonic single MRM-assisted MZI PAM-4 modulator," IEEE Photonics J. **9**(6), 4900607 (2017).

I conceived the idea, performed the numerical analysis and the experiments, and wrote the paper. The co-authors contributed in discussing the idea, refining the analysis and revising the manuscript.

[3] **R. Li**, D. Patel, E. El-Fiky, A. Samani, Z. Xing, M. Morsy-Osman, and D. V. Plant, "High-

speed low-chirp PAM-4 transmission based on push-pull silicon photonic microring modulators," Opt. Express **25**(12), 13222-13229 (2017).

I conceived the idea, performed the simulation, conducted the experiments and wrote the paper. The co-authors contributed in discussing the idea, building up the experiment setup and revising the manuscript.

[4] **R. Li**, D. Patel, A. Samani, E. El-Fiky, Z. Xing, M. Sowailem, Q. Zhong and D. V. Plant, "An 80 Gb/s silicon photonic modulator based on the principle of overlapped resonances," IEEE Photonics J. **9**(3), 4900311 (2017).

I conceived the idea, performed the numerical analysis and simulation, conducted the experiments, and wrote the paper. The co-authors contributed in building up the experiment setup, discussing the results and revising the manuscript.

[5] **R. Li**, D. Patel, A. Samani, E. El-Fiky, Z. Xing, M. Morsy-Osman, and D. V. Plant, "Silicon Photonic ring-assisted MZI for 50 Gb/s DAC-less and DSP-free PAM-4 transmission," IEEE Photonics Technol. Lett. **29**(12), 1046-1049 (2017).

I conceived the idea, performed the simulation and the experiments, and wrote the paper. The co-authors contributed in discussing the idea, building up the experiment setup analyzing the results and revising the manuscript.

Conference Proceedings Directly Related to This Thesis

[6] **(Invited) R. Li**, D. Patel, E. El-Fiky, A. Samani, Z. Xing, L. Xu, and D. V. Plant, "A C-band push-pull silicon photonic modulator for 20 km SSMF transmission without CD compensation," in *Conference on Lasers and Electro-Optics* (Optical Society of America, 2017), paper SM2O.3.

I conceived the idea, conducted the experiments and wrote the paper. The co-authors contributed in building up the experiment setup, discussing the results and revising the manuscript.

[7] **R. Li**, D. Patel, E. El-Fiky, A. Samani, Z. Xing, Y. Wang and D. V. Plant, "56 Gb/s DAC-less and DSP-free PAM-4 using a silicon photonic dual-drive Michelson interferometric modulator," in *Optical Fiber Communication Conference* (Optical Society of America, 2018), paper W4D.1.

I conceived the idea, conducted the experiments and wrote the paper. The co-authors contributed *in revising the manuscript.*

[8] **R. Li**, A. Samani, E. El-Fiky, D. Patel, Q. Zhong, and D. V. Plant, "56-Gbps OOK transmission using silicon microring assisted Mach-Zehnder interferometer," in *Conference on Lasers and Electro-Optics* (Optical Society of America, 2016), paper STu4G.4.

I conceived the idea, conducted the experiments and wrote the paper. The co-authors contributed in discussing the idea, building up the experiment setup and revising the manuscript.

Journal Articles Not Directly Related to This Thesis

[9] L. Xu, Y. Wang, A. Kumar, D. Patel, E. El-Fiky, Z. Xing, **R. Li**, and D. V. Plant, "Polarization beam splitter based on MMI coupler with SWG birefringence engineering on SOI," IEEE Photonics Technol. Lett. **30**(4), 403-406 (2018).

[10] Y. Wang, L. Xu, A. Kumar, Y. D'Mello, D. Patel, Z. Xing, **R. Li**, M. G. Saber, E. El-Fiky, and D. V. Plant, "Compact single-etched sub-wavelength grating couplers for O-band application," Opt. Express **25**(24), 30582-30590 (2017).

[11] E. El-Fiky, M. Osman, M. Sowailem, A. Samani, D. Patel, **R. Li**, M. G. Saber, Y. Wang, N. Abadía, Y. D'Mello, and D. V. Plant, "200 Gb/s transmission using a dual-polarization O-band silicon photonic intensity modulator for Stokes vector direct detection applications," Opt. Express **25**(24), 30336-30348 (2017).

[12] A. Samani, D. Patel, M. Chagnon, E. El-Fiky, **R. Li**, M. Jacques, N. Abadía, V. Veerasubramanian, and D. V. Plant, "Experimental parametric study of 128 Gb/s PAM-4 transmission system using a multi-electrode silicon photonic Mach Zehnder modulator," Opt. Express **25**(12), 13252-13262 (2017).

[13] W. Wang, Q. Zhuge, M. Morsy-Osman, Y. Gao, X. Xu, M. Chagnon, M. Qiu, M. T. Hoang, F. Zhang, **R. Li**, and D. V. Plant, "Decision-aided sampling frequency offset compensation for reduced-guard-interval coherent optical OFDM systems," Opt. Express **22**(22), 27553-27564 (2014).

Conference Proceedings NOT Directly Related to This Thesis

[14] E. El-Fiky, Y. D'Mello, Y. Wang, M. G. Saber, A. Kumar, J. Skoric, A. Samani, L. Xu, **R.**

Li, D. Patel, and D. V. Plant, "Ultra-broadband and compact asymmetrical beam splitter enabled by angled sub-wavelength," in *Conference on Lasers and Electro-Optics* (Optical Society of America, 2018), paper STh4A.7.

[15] K. Zhang, Q. Zhuge, H. Xin, Z. Xing, **R. Li**, M. Xiang, S. Fan, L. Yi, W. Hu, and D. V. Plant, "Investigation on the dispersion tolerance in dual-drive MZM-based DAC-less optical PAM4 transmission," in *Optical Fiber Communication Conference* (Optical Society of America, 2018), paper Tu2C.2.

[16] Z. Xing, D. Patel, T. Hoang, M. Qiu, **R. Li**, E. El-Fiky, M. Xiang, and D. V. Plant, "100Gb/s 16-QAM transmission over 80 km SSMF using a silicon photonic modulator enabled VSB-IM/DD system," in *Optical Fiber Communication Conference* (Optical Society of America, 2018), paper M2C.7.

[17] L. Xu, Y. Wang, D. Patel, M. Osman, **R. Li**, M. Hui, M. Parvizi, N. Ben-Hamida, and D. V. Plant, "Ultra-broadband and ultra-compact optical 90° hybrid based on 2x4 MMI coupler with subwavelength gratings on silicon-on-insulator," in *Optical Fiber Communication Conference* (Optical Society of America, 2018), paper M3I.7.

[18] Y. Wang, L. Xu, A. Kumar, D. Patel, Z. Xing, **R. Li**, M. Saber, E. El-Fiky, Y. D'Mello, D. V. Plant, "Broadband sub-wavelength grating coupler for O-band application," in *Proceedings of IEEE. 14th International Conference on Group IV Photonics* (IEEE, 2017), paper ThP.9.

[19] L. Xu, Y. Wang, D. Patel, E. El-Fiky, Z. Xing, **R. Li**, M. G. Saber, M. Jacques, and D. V. Plant, "Polarization independent adiabatic 3-dB coupler for silicon-on-insulator," in *Conference on Lasers and Electro-Optics* (Optical Society of America, 2017), paper SF1I.5.

Table of Contents

List of Figures

List of Tables

List of Acronyms

ZB	Zettabytes
CMOS	Complimentary metal-oxide-semiconductor
MPW	Multi-project-wafer
SiP	Silicon photonic
IM/DD	Intensity-modulation/direct-detection
DSP	Digital signal processing
OOK	On-off keying
PAM-4	Four-level pulse amplitude modulation
SNR	Signal-to-noise ratio
SSMF	Standard single mode fiber
MRM	Microring modulator
MZI	Mach-Zehnder interferometer
MRR	Microring resonator
DAC	Digital-to-analog converter
MIM	Michelson interferometric modulator
TWMZM	Travelling-wave Mach-Zehnder modulator
BGM	Bragg grating modulator
EAM	Electro-absorption modulator
SISCAP	Silicon-insulator-silicon capacitor
WDM	Wavelength-division-multiplexing
EO	Electro-optic
SOI	Silicon-on-insulator

IL	Insertion loss
BPSK	Binary phase-shift keying
QPSK	Quadrature phase-shift keying
RF	Radio-frequency
DC	Direct-current
CD	Chromatic dispersion
OMA	Optical modulation amplitude
ER	Extinction ratio
FOM	Figure of merit
RAMZI	Ring-assisted MZI
BER	Bit error rate
HD	Hard-decision
FEC	Forward-error correction
BOX	Buried oxide
GC	Grating coupler
TE	Transverse electric
3D	Three-dimensional
FDTD	Finite-difference time-domain
FSR	Free spectral range
FWHM	Full-width at half maximum
Q-factor	Quality factor
EE	Electrical-electrical
PD	Photodetector
PP	Push-pull
SPP	Series push-pull

PRBS	Pseudo-random binary sequence
DCF	Dispersion compensation fiber
OSA	Optical spectrum analyzer
BPG	Bit pattern generator
EDFA	Erbium-doped fiber amplifier
B2B	Back-to-back
DCA	Digital communication analyzer
TIA	Trans-impedance amplifier
RTO	Real-time oscilloscope
PRIS	Pseudo random integer sequence
RRC	Root-raised cosine
SD	Soft decision
ECL	External cavity laser
TM	Transverse magnetic
PAM-8	Eight-level pulse amplitude modulation
16-QAM	16-state quadrature amplitude modulation

Chapter 1

Introduction

1.1 Overview

Supported by data centers with hundreds of servers, high-speed Internet services, such as cloud-based computing and storage, social networking and online multi-media, are revolutionizing our daily life. While benefiting from these bandwidth hungry applications, we are witnessing the rapid growth of data center traffic. According to the forecast by Cisco [1], the annual global data center IP traffic will increase from 4.7 zettabytes (ZB) in 2015 to 15.3 ZB by the end of 2020. The intra-data center traffic, such as moving data from a development environment to a production environment within a data center, or writing data to a storage array, occupies 77% of the data center traffic by the year of 2020. If taking the rack-local traffic into consideration, more than 90% of the traffic remains within the data center [1].

Short-reach fiber-optic communication technologies, which support a high transmission speed and a large bandwidth, is a promising solution to fulfill the demand of the ever-increasing intra-data center traffic. Moreover, optoelectronic and optical components can potentially solve the power dissipation and interconnects density problems in the future large-scale information processing machines [2].

High-speed low-cost modulators, which are the key components for the intra-data center optical communication links, have attracted immense research interest in recent years. There are two important aspects regarding modulators: the fabrication platform and the modulation format. Silicon photonics is a mature platform for developing data center interconnects. It is compatible to the complimentary metal-oxide-semiconductor (CMOS) fabrication processes. Moreover, compared to other photonic integration platforms, silicon photonics has a larger wafer size and a lower substrate cost for large volume integration [3, 4]. Currently, supported by the multi-project wafer (MPW) runs provided by foundries, such as IME A*STAR and IMEC, silicon photonics is on the way to be a mature and fabless industry [5]. Recent reports on a variety of silicon photonic (SiP) devices, such as modulators [6, 7], photodetectors [8, 9] and various passive devices [10-12], further demonstrate the suitability of silicon photonics for data center interconnects.

Regarding the modulation format, intensity modulation is favored over coherent modulation. Figure 1-1 compares a typical intensity-modulation/direct-detection (IM/DD) system [13] with a typical coherent transmission system [14]. As IM/DD systems do not require a local oscillator or complicated digital signal processing (DSP), they are more cost-saving and suitable than coherent transmission systems for intra-data center applications.

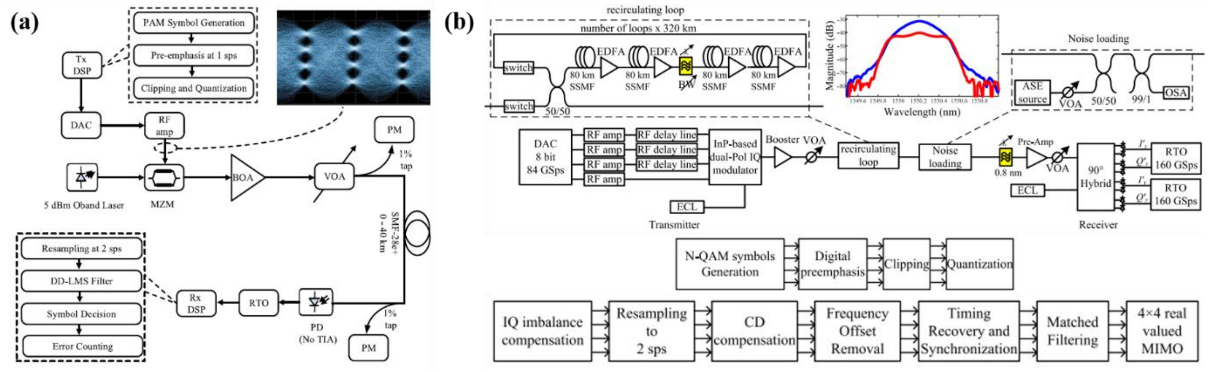

Fig. 1-1. (a) An 84 Gbaud IM/DD transmission system and the DSP applied [13] (©2017 IEEE) and (b) an 84 Gbaud coherent transmission system and the DSP applied [14] (©2017 IEEE).

For the applications in the 40G and 100G Ethernet, on-off keying (OOK) modulation has been widely applied [15]. But given the bandwidth requirement for the applications in the next generation 400G Ethernet, higher order modulation formats are preferred. Among them, four-level pulse amplitude modulation (PAM-4) is a good choice when considering both the spectral efficiency and the required signal-to-noise ratio (SNR). Currently, 8λ × 50G PAM-4 over 2 km of standard single fiber (SSMF) transmission (400GBASE-FR8) has been selected for the next generation 400G Ethernet [16].

The objective of this thesis is to investigate SiP PAM-4 modulators for the next generation intra-data center optical communication systems. In this thesis, PAM-4 generation using two modulator structures are demonstrated targeting intra-data center applications. First, a dual microring modulators (MRMs) assisted Mach-Zehnder interferometer (MZI) is studied. Three different operating principles for generating PAM-4 optical signals are investigated, which are the push-pull operation of dual parallel MRMs, the resonances overlap operation of an MRM with an microring resonator (MRR), and the dual-drive operation without implementing a digital-to-analog converter (DAC) or DSP. Second, DAC-less and DSP-free generation of PAM-4 signals using the dual-drive Michelson interferometric modulator (MIM) is presented and discussed.

1.2 Motivation

The urgent need of high-speed low-cost PAM-4 modulators for intra-data center applications, and the potential of the silicon photonics technology in building these devices, are the major motivations of research in this field.

Plenty of SiP modulators using different structures have been reported, such as travelling-wave Mach-Zehnder modulators (TWMZMs) [6, 7], MRMs [17, 18], lumped MIM [19], Bragg grating modulator (BGM) [20], GeSi electro-absorption modulators (EAMs) [21, 22], and silicon-insulator-silicon capacitor (SISCAP) modulator [23]. Figure 1-2 shows the schematics of each modulator structure. TWMZM is thermally stable and tolerant to fabrication variations, but it has a large footprint, with a length of typically several millimeters, as shown in Fig. 1-2(a). In [6, 7], TWMZM-based 112 Gb/s PAM-4 transmissions have been reported. On the other hand, MRM occupies small footprint as its radius is only tens of micrometers, as shown in Fig. 1-2(b). Moreover, its natural filtering ability favors it for wavelength-division-multiplexing (WDM) applications. But it is very sensitive to temperature changes and small variations in the fabrication process. 64 Gb/s PAM-4 transmission over 5 km of SSMF is demonstrated using a single MRM in [18]. The dominant source of power consumption in a TWMZM is the termination resistor, and that in an MRM is the heater for thermally controlling the resonant wavelength. Lumped MIM can avoid these additional sources of power consumption. As shown in Fig. 1-2(c), its modulation efficiency is doubled because of the loop mirrors at the end of the structure [19]. But the electro-optic (EO) bandwidth of the MIM is lower than those of a TWMZM and an MRM.

In addition, the MIM in [19] is designed to operate in a single-drive configuration, therefore only 40 Gb/s OOK modulation results are presented. BGM with a lumped design structure is recently reported, and it achieves 60 Gb/s PAM-4 [20]. However, as shown in Fig. 1-2 (d), the sidewall corrugations of the gratings are only tens of nanometers. This makes the operating wavelength of BGM very sensitive to fabrication variations. GeSi EAM exploits the sub-picosecond phenomenon Franz–Keldysh effect, and thus it enables high-speed modulation. As a waveguide modulator, it is only tens of micrometers in length [21, 22]. But since Ge has a strong absorption in O-band (around 1310 nm) and C-band (around 1550 nm) [24], GeSi EAM operation is limited to the edge of the C-band and L-band (around 1600 nm). In [22], 100 Gb/s OOK modulation is demonstrated based on a GeSi EAM. The SISCAP modulator is based on a vertical PN junction, which consists of a p-type poly-Si layer, a gate-oxide layer and a n-type silicon-on-insulator (SOI) layer, as shown in Fig. 1-2(f). It achieves a high modulation efficiency because the high charge density region is largely overlapped with the optical mode. But its optical insertion loss (IL) is also high due to the optical scattering in the poly-Si layer. Moreover, the fabrication process of the vertical PN junction is more complicated compared to that of the lateral PN junctions used in other modulator structures. The pros and cons of each SiP modulator structure are summarized in Table 1.

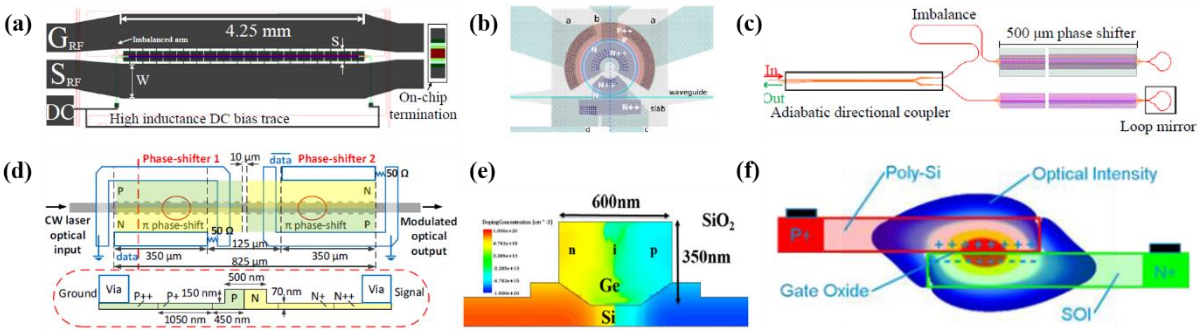

Fig. 1-2. Schematics of (a) TWMZM [6], (b) MRM [18], (c) MIM [19], (d) BGM [20], (e) GeSi EAM [21] (©2016 IEEE) and (f) SISCAP modulator [23] (©2014 IEEE).

In addition to these structures, SiP modulators based on a combination of an MZI and MRRs have also been reported to achieve wide operating wavelength range [25], thermal stability [26] and high linearity [27]. These structures are also used for OOK modulation [28, 29], binary

Table 1. Pros and cons of each SiP modulator structure.

Modulator structure	Pros	Cons
TWMZM	Thermal stable, high fabrication tolerance	Large footprint
MRM	Compact, natural filtering ability	Thermal unstable, fabrication sensitive
MIM	Low power consumption, 2× efficiency	Limited EO bandwidth
BGM	Lumped design	Operating λ sensitive to fabrication
GeSi EAM	Compact, high-speed	Operating λ in L-band
SISCAP modulator	Large modulation efficiency	High optical IL, hard fabrication process

phase-shift keying (BPSK) [29], quadrature phase-shift keying (QPSK) [30] and PAM-4 [31]. To the best of our knowledge, the best modulation performance using this structure for IM/DD is 25 Gb/s PAM-4, and for coherent modulation is 56 Gb/s QPSK.

In recent years, PAM-4 signal generation without implementing DAC or any DSP (e.g. pre-emphasis, pulse shaping, equalization, etc.) is proposed to further reduce the power consumption in the optical transmission links. This has been achieved with various SiP modulators, such as MZI-assisted ring modulator [31], TWMZMs [32-35], cascaded dual MRMs [36], segmented MRM [37], push-pull segmented SISCAP modulators [38] and dual parallel GeSi EAMs [39]. It should be noted that though the device in [35] is driven by 4-level radio-frequency (RF) signals, there is no DAC or DSP applied in the transmission link. The RF signals are obtained by combining two channels from a pulse pattern generator. In [40], 60 Gb/s PAM-4 optical signals are generated without the use of a DAC. But DSP including filtering, resampling and equalization is applied on the receiver side. Therefore, the result presented in [40] is not regarded as a DAC-less DSP-free PAM-4 signal generation.

In conclusion, high-speed low-cost PAM-4 modulators are key components in the next generation intra-data center optical transmission links, and silicon photonics offers a promising platform for developing these devices. Currently, various SiP modulators have been reported for short-reach IM/DD systems. Based on these two major motivations, this thesis is focused on the SiP PAM-4 modulators for short-reach optical transmission systems. To be specific, we use three operating principles on two SiP modulator structures to achieve PAM-4 signals generation and transmission over distances which are suitable for intra-data center applications.

1.3 Thesis organization

Following this chapter on introduction, the remainder of this thesis is organized as follows:

In **Chapter 2**, the fundamentals of SiP modulators are presented. First, the basics of designing SiP modulators, including the plasma dispersion effect, the designs of silicon waveguide, lateral PN junction and heater, are introduced. Then the SiP modulators, including MRMs, TWMZMs, and other modulator structures, are reviewed. The focus is on the device structure, modulation principle and the state of the art for IM/DD applications.

In **Chapter 3**, the push-pull operation of dual parallel MRMs is demonstrated. Following the presentation of the device design and the description of the fabrication method, the operating principle is explained using the system-level simulation and it is further proved by the chirp measurement. Afterwards, the device is characterized by both direct-current (DC) measurement to show the modulation efficiency, and by small-signal modulation to show the EO bandwidth. The experimental results of large-signal modulation based on this operating principle, including OOK modulation and PAM-4 transmission without any chromatic dispersion (CD) compensation, are also presented.

In **Chapter 4**, the resonances overlap operation of an MRM with an MRR is investigated. After the device design and fabrication being introduced, the operating principle is explained in two steps. First, by assisting a single MRM in an MZI, the optical modulation amplitude (OMA) and the static extinction ratio (ER) are both improved compared to those of a single MRM. Second, by overlapping the resonances of the MRM with an MRR assisted in another arm of the MZI, these two figure of merits (FOMs) are further enhanced. The measured DC transmission spectra are also presented to explain this operating principle experimentally. Afterwards, OOK modulation and PAM-4 transmission using a single MRM, a single MRM-assisted MZI, and a MZI assisted by the resonances overlap of an MRM with an MRR are all presented. Their large-signal modulation results are compared to further prove the advantages of the resonances overlap operating principle. Other resonances overlap operating principles are also introduced and analyzed in this chapter.

In **Chapter 5**, dual-drive operation for DAC-less and DSP-free PAM-4 signal generation is demonstrated. This operating principle is applied on two modulator strucutures: a ring-assisted MZI (RAMZI) modulator and an MIM. In Section 5.2, the dual-drive operation of a RAMZI modulator is presented: the device design and fabrication is shown, and the operating principle is then presented by system-level simulation; afterwards, the device characterization is reported with a focus on the bias conditions of the device and the choice of the driving RF signals; then the PAM-4 experimental results are presented. In Section 5.3, the dual-drive operation of an MIM is studied: the PN junction designs with asymmetric 4 doping concentrations and symmetric 6 doping concentrations are compared by simulation; then the design and fabrication of two MIMs using these two PN junction structures are presented; afterwards, they are experimentally compared in terms of the modulation efficiencies and the bandwidths; then the experimental results of PAM-4 transmission are presented for further comparison.

Finally, **Chapter 6** summarizes the major works presented in this thesis and proposes several potential research directions for future work.

1.4 Original contribution

In brief, the major original contributions of this thesis are the three operating principles of generating PAM-4 optical signals based on the two SiP modulators: the RAMZI modulator and the dual-drive MIM. They are summarized as follows:

SiP RAMZI modulator

- The low-chirp modulation of the dual MRMs assisted MZI modulator is explained by the system-level simulation, and characterized by the chirp parameters using 10 Gb/s OOK transmission over 20 km of SSMF [41]. The measured OOK modulation results are better than those of a single MRM [42], further proves the low-chirp property of this operating principle. Without any CD compensation, we demonstrate successful PAM-4 transmission over 1 km of SSMF at 92 Gb/s with a bit error rate (BER) below the hard-decision (HD) forward-error correction (FEC) threshold of 3.8×10^{-3} [41]. The bit rate we achieved is the highest published for the PAM-4 transmission based on the modulation of SiP MRMs up to date. Moreover, 56 Gb/s PAM-4 transmission over 10 km of SSMF and at 40 Gb/s over 20 km of SSMF are also presented, with measured BERs below the HD FEC threshold [41].

- We report on the analysis and experimental study of a SiP single MRM-assisted MZI to prove that its OMA and ER are both enhanced compared to those of a single MRM with the same design parameters [43]. 76 Gb/s PAM-4 is achieved based on this structure [43]. Moreover, by assisting the device with a passive MRR on the other MZI arm and overlapping the resonances of the MRM with that of the MRR, the OMA and ER are further improved [44, 45]. We also present the numerical analysis and simulation of the resonances overlapping operation principle [45]. Moreover, 2 km of SSMF transmissions using 56 Gb/s OOK modulation [44, 45] and 80 Gb/s PAM-4 [45] are demonstrated, with measured BERs below the HD FEC threshold.
- We investigate the generation of evenly spaced PAM-4 optical signals by system-level simulation of the SiP RAMZI modulator. The experimental design method, including the chosen of the bias conditions and the parameters of the driving RF signals on each MRM, is also presented using the measured DC transmission when applying voltages on both MRMs [46]. DAC-less and DSP-free PAM-4 transmission at 40 Gb/s over 5 km of SSMF and at 50 Gb/s over 2 km of SSMF is presented, with estimated BERs below the HD FEC threshold [46].

SiP dual-drive MIM

- We compare the PN junction designs with asymmetric 4 doping concentrations and symmetric 6 doping concentrations by the simulation of effective index changes, waveguide losses and junction resistances [47]. We also investigate the measured modulation efficiencies and the small-signal characterization to show the advantages of the optimized PN junction design [47].
- We demonstrate 56 Gb/s PAM-4 transmission over 2 km of SSMF by driving the device with two independent binary RF signals, which results in a DAC-less and DSP-free PAM-4 signal generation with reasonable even spacing [47, 48]. The two devices

with different PN junction designs are also experimentally compared, showing the dual-drive MIM with symmetric 6 doping concentrations have better PAM-4 transmission performance [47].

Chapter 2

Fundamentals of SiP Modulators

2.1 Overview

Since the pioneering works of Soref in the late 1980s and early 1990s [49-51], silicon photonics technology has developed rapidly. The early works are mainly focused on passive devices, such as silicon optical waveguides [52, 53], direction coupler [54], interferometer [55] and multiplexer/demultiplexer [56]. In 2004, Intel Cooperation demonstrated the first GHz silicon photonic modulator [57]. In 2013, the first deletion-mode carrier-plasma modulator fabricated in a standard 45 nm CMOS platform with no changes in the fabrication process was reported [58]. In recent years, SiP modulators have attracted immense research interest, and their performance metrics have been tremendously improved. They have also been widely implemented in commercial products, such as the 100G parallel single-mode fiber 4-lane optical transceiver by Intel [59], the 100G integrated opto-electronic transceiver by Luxtera [60], the 200G direct detect optical transceiver by Ranovus [61], and the 200G quad small form-factor pluggable transceiver by Mellanox [62].

In this chapter, the fundamentals of SiP modulators are reviewed, and it is organized as follows. In Section 2.2, the modulation basics are introduced. The plasma dispersion effect [50], which is the most commonly used principle for modulation in silicon, is described in Section 2.2.1. Then the design methods of silicon waveguide, lateral PN junction and heater are presented in Section 2.2.2, Section 2.2.3 and Section 2.2.4, respectively. Afterwards, Section 2.3 reviews the different SiP modulators, including MRMs in Section 2.3.1, TWMZMs in Section 2.3.2, and other modulator structures in Section 2.3.3. The review is focused on the device structure, modulation principle and the state of the art for IM/DD transmission systems. Finally, this chapter is concluded in Section 2.4.

2.2 SiP modulation basics

The plasma dispersion effect [50] is the basic of EO modulation in the PN doped silicon waveguide. As most of the SiP modulators utilize carrier-depletion in the reverse-biased PN junctions and they work in C-band [6, 7, 17-20, 28-37, 40-48], this section introduces the fundamentals of SiP modulation and design methods of PN doped silicon waveguides based on carrier-depletion modulation at around 1550 nm.

2.2.1 Plasma dispersion effect

When applying electrical currents to the PN doped silicon waveguides, the carrier densities are changed, and thus the refractive index of the waveguides is changed accordingly [50]. As the real and imaginary parts of the refractive index are coupled, which is described by the Kramers-Kronig relation [63], both the effective index and optical absorption of the silicon waveguides will be changed. This is termed the plasma dispersion effect, and it is applied for carrier-depletion SiP modulators driven by reverse biased RF signals [6, 7, 17-20, 28-37, 40-48], or carrier-injection SiP modulators driven by forward biased RF signals [25]. In [64], the effective index change Δn and the optical absorption coefficient change Δα (in cm^{-1}) in the silicon waveguide at a wavelength of 1550 nm are evaluated using the following equations:

$$\Delta \mathrm{n} = -8.8\times10^{-22}\,\Delta N - 8.5\times10^{-18}\,\Delta P^{0.8} \tag{2.1}$$

$$\Delta\alpha = 8.5\times10^{-18}\,\Delta N + 6.0\times10^{-18}\,\Delta P \tag{2.2}$$

where ΔN and ΔP are the carrier densities of electrons and holes in cm^{-3}, respectively.

These two equations are straightforward for calculation. If using the same concentrations for electrons and holes, e.g. $\Delta N = \Delta P = 5 \times 10^{17}\ \mathrm{cm}^{-3}$, the effective index change is $\Delta n = -1.6 \times 10^{-3}$ and the optical absorption coefficient change is $\Delta\alpha = 7.55\ \mathrm{cm}^{-1}$. The contribution of holes in Δn is approximately 75%, but it is only around 40% in Δα.

Based on more recent experimental data, the models at 1550 nm were updated in 2011 as follows [65]:

$$\Delta \mathrm{n} = -5.40\times10^{-22}\,\Delta N^{1.011} - 1.53\times10^{-18}\,\Delta P^{0.838} \tag{2.3}$$

$$\Delta\alpha = 8.88\times10^{-21}\Delta N^{1.167} + 5.84\times10^{-20}\Delta P^{1.109} \tag{2.4}$$

Similarly, if using ΔN = ΔP = 5 × 10^{17} cm^{-3} for calculation based on these two updated equations, the change in the effective index is Δn = -1.46 × 10^{-3}, in which approximately 71% is from the contribution of holes. The optical absorption coefficient change is Δα = 6.49 cm^{-1}, in which only around 38% comes from the contribution of holes. Figure 2-1 clearly compares the contributions of electrons and holes to Δn and Δα, based on Eqs. 2.1 – 2.4. Both the two models conclude that the concentration of holes contributes more to Δn and has less effect on Δα than those of electrons.

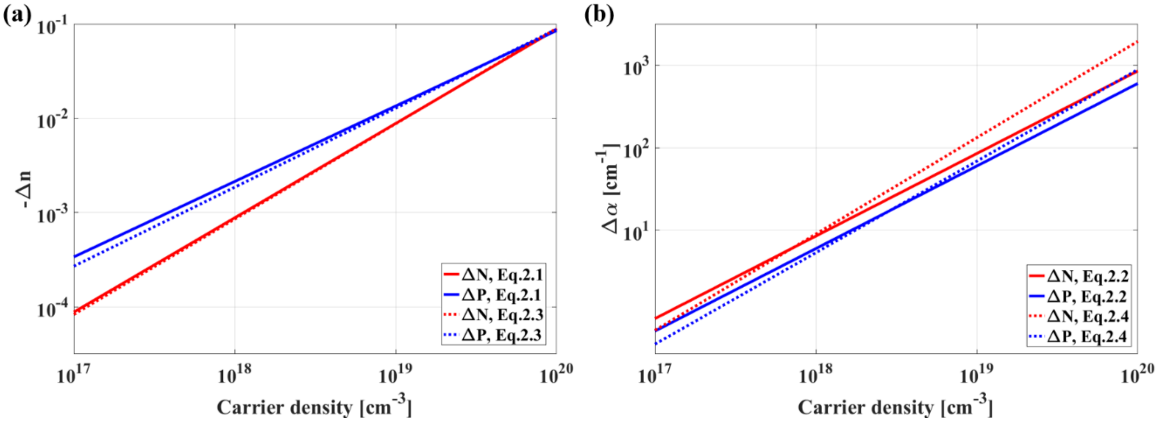

Fig. 2-1. (a) Effective index changes and (b) optical absorption coefficient changes with carrier densities in PN doped silicon waveguides.

Therefore, PN junction designs in a zigzag configuration [17] and with an offset [19] have been reported to make the best advantage of the hole concentrations. Currently, the doping concentrations typically used in the MPW runs at IME A*STAR, one of the global foundries, are ΔN = 3 × 10^{17} cm^{-3} and ΔP = 5 × 10^{17} cm^{-3} [66]. As the holes concentration is larger than the electrons concentration, SiP modulators with symmetric PN junctions are designed and fabricated at IME, and they can also achieve a high modulation efficiency [6, 7, 32, 33].

When the PN junction is reverse biased, i.e. positive and negative voltages are applied on the n-type layer (typically implanted with phosphorus) and p-type layer (typically implanted with boron), respectively, the free carriers will be depleted [67]. On the other hand, carriers are injected in the waveguide by forward biasing the PN junction, i.e. positive and negative voltages are applied on the p-type and n-type layers, respectively [67]. As shown in Fig. 2-1, these two mechanisms both change the effective indices in the PN doped silicon waveguides, and thus enable EO modulation. Compared to the SiP modulators working in the forward-biased carrier-injection mode [25, 68], those working in the reverse-biased carrier-depletion mode has larger EO bandwidths and they can work at higher modulation speeds [6, 7, 17-20, 28-37, 40-48, 68]. But the reverse-biased SiP modulators need larger driving peak-to-peak voltages than the forward-biased ones [68].

2.2.2 Silicon waveguide design

Figure 2-2 shows the cross-section of the IME silicon photonics MPW platform [69]. The 2-μm buried oxide (BOX) layer is on a silicon substrate, and the cladding layer is silicon dioxide. There are three etching heights for the top silicon layers, which are 60-nm shallow etch for the grating couplers (GCs), 130-nm shallow etch for the rib waveguide and 220-nm full etch for the channel waveguide. The typical waveguide structure used for designing PN doped phase shifters in the SiP modulators is a 220-nm rib waveguide on a 90-nm slab, as shown in Fig. 2-2.

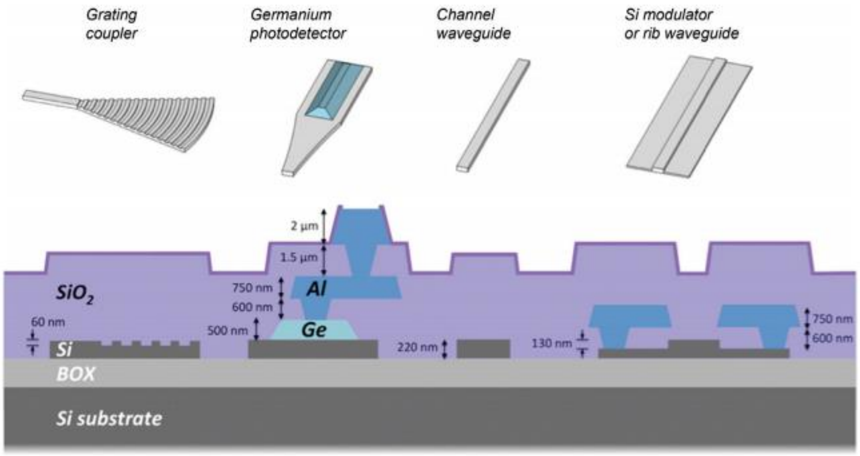

Fig. 2-2. Cross-section of the IME silicon photonics MPW platform. [69] (©2013 IEEE)

Figure 2-3 presents the silicon waveguide structure for simulation using Lumerical MODE Solutions [70] based on the fabrication process shown in Fig. 2-2. The properties of the materials used in the simulation model are from the optical constants of solids database [71], where the refractive indices of silicon and silicon dioxide near 1550 nm at room temperature are approximately 3.48 and 1.44, respectively. The width of the rib waveguide is 500 nm. It is a commonly used number determined from the trade-off between supporting only the fundamental transverse electric (TE) mode [72] and minimizing the optical propagation loss in telecom wavelengths [73]. The eigenmode solver is used for simulating the mode profiles, effective indices and group indices in different conditions, e.g. at different wavelengths or with different bent radius of the waveguides.

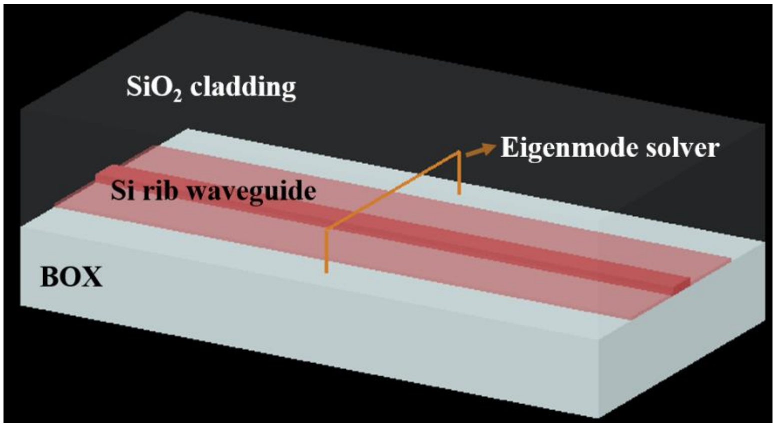

Fig. 2-3. Silicon waveguide structure for simulation using Lumerical MODE Solutions.

The simulated optical mode at 1550 nm in the straight waveguide is shown in Fig. 2-4(a), and it is mostly confined in the 500-nm × 220-nm waveguide. The optical modes in bent waveguides are also investigated, as shown in Figs. 2-4(b) – 2-4(f). When the bent radius R is 3 µm, the optical mode is in the slab waveguide and this is undesirable. With at least 5-µm bent radius, the

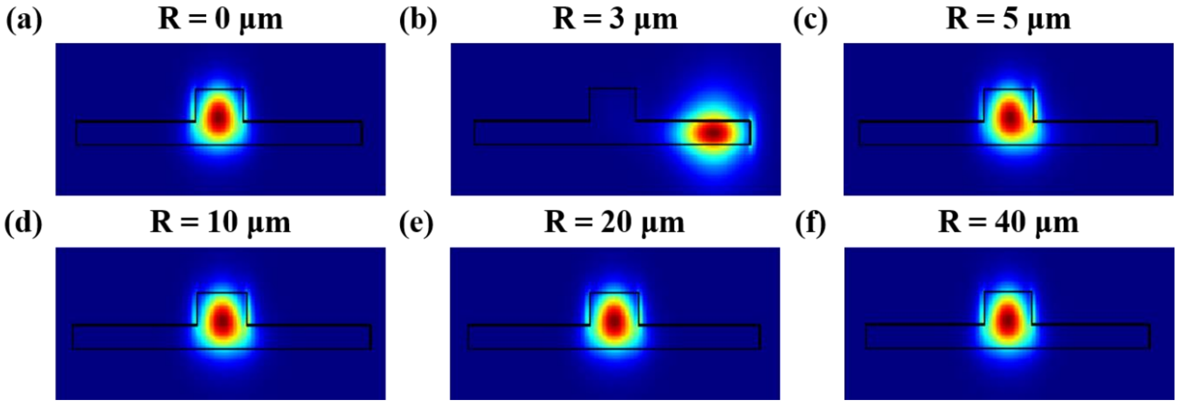

Fig. 2-4. Simulated optical modes at 1550 nm in the waveguides with a bent radius of (a) 0 µm, (b) 3 µm, (c) 5 µm, (d) 10 µm, (e) 20 µm and (f) 40 µm.

optical mode is confined in the rib waveguide, which is suitable for optical transmission.

To investigate the propagation losses in the bent waveguides, three-dimensional (3D) finite-difference time-domain (FDTD) simulation is used in Lumerical FDTD Solutions [74], as shown in Fig. 2-5. The propagation loss is calculated by the transmitted power of the fundamental mode over its input power.

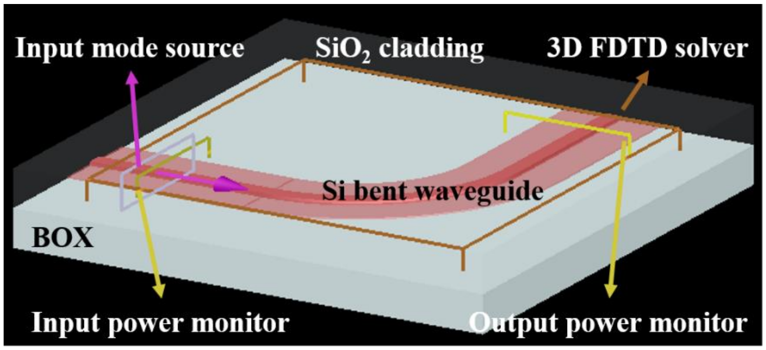

Fig. 2-5. Silicon bent waveguide structure for simulation using Lumerical FDTD Solutions.

Figure 2-6 shows the simulated results of a bent 500-nm × 220-nm rib waveguide on a 90-nm slab. To achieve a low-loss bend, the waveguide bent radius should be at least 5 μm. A typical value used in the device design and fabrication is 10 μm.

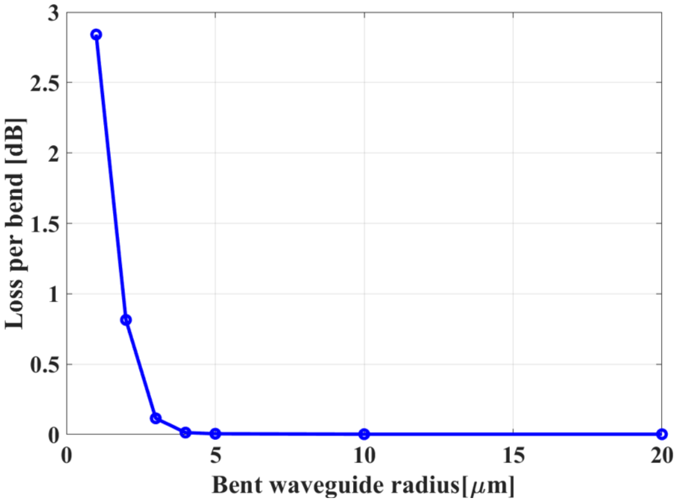

Fig. 2-6. Simulated propagation losses per bend with different bent radius.

Using the method in [73], the effective indices and group indices of the fundamental TE mode in the straight rib waveguide at different wavelengths from 1500 nm to 1600 nm are simulated in Lumerical MODE Solutions. As shown in Fig. 2-7(a), the effective index varies with the wavelength, so the silicon waveguide is dispersive. The group index n_g is a result of this dispersion, and it can be approximately calculated using the following equation based on its definition [75]:

$$\mathrm{n_g} = n_{eff} - \lambda \frac{dn_{eff}}{d\lambda} \tag{2.5}$$

where n_{eff} is the effective index at wavelength λ. The group indices shown in Fig. 2-7(b) are calculated using the simulated effective indices in Fig. 2-7(a) and Eq. 2.5. They can be used in the electrode design for SiP TWMZMs [6].

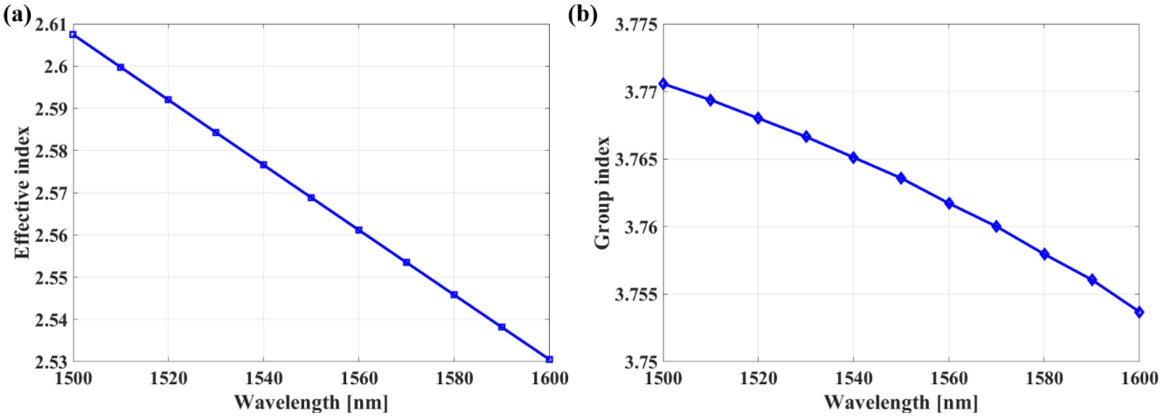

Fig. 2-7. Simulated effective indices and calculated group indices of the fundamental TE mode in the straight rib waveguide at different wavelengths.

2.2.3 Lateral PN junction design

In most of the SiP modulators reported, reverse-biased lateral PN junctions are used as phase shifters for modulation via the plasma dispersion effect [6, 7, 17-20, 28-37, 40-48]. Their geometries are designed to optimize the modulation efficiency, optical waveguide loss and the 3-dB cutoff frequency. As the doping concentrations and the implantation processes in the IME MPW run are kept confidential within the foundry, constant doping of the values in [66] are used as an example in this section. There are 6 doping concentrations, which are 5×10^{17} $\mathrm{cm^{-3}}$ for P, 3×10^{17} $\mathrm{cm^{-3}}$ for N, 2×10^{18} $\mathrm{cm^{-3}}$ for P+, 3×10^{18} $\mathrm{cm^{-3}}$ for N+, 1×10^{20} $\mathrm{cm^{-3}}$ for P++ and N++.

In fact, PN junctions with 4 doping concentrations [19] or 6 doping concentrations [6, 7, 32, 33] can both be fabricated in the MPW runs at IME. Figure 2-8 shows the schematic of a PN junction with 6 doping concentrations. The optical waveguide is a 500-nm × 220-nm rib on a 90-nm slab, as analyzed in Section 2.2.2. The geometries to be designed are the widths of each doping concentration, which are W_p, W_n, W_{p+}, W_{n+}, W_{p++}, W_{n++}, and the distance between the edge of the N doping area to the middle of the optical waveguide, which is $W_{n,\ offset}$. Because the doping concentrations of holes are larger than those of electrons, $W_{n,\ offset}$ is set to be zero and a symmetric PN junction is formed to make the best advantages of the contribution from the hole concentrations, as analyzed in Section 2.2.2. $W_n = W_p = 370$ nm and $W_{n+} = W_{p+} = 810$ nm are chosen based on those reported in [6, 33] as an example for the PN junction simulation. The other geometric parameters are $W_{n++} = W_{p++} = 6.42$ µm.

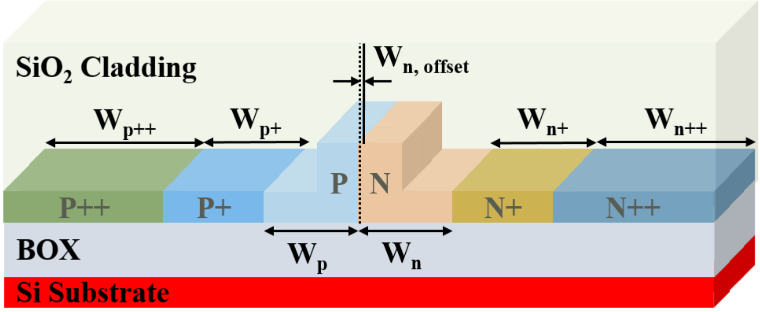

Fig. 2-8. Schematic of a PN junction with 6 doping concentrations.

Based on the simulation methods in [73], first the carrier distributions in the PN doped rib waveguide at various reverse bias voltages are simulated using Lumerical DEVICE [76]. Figure

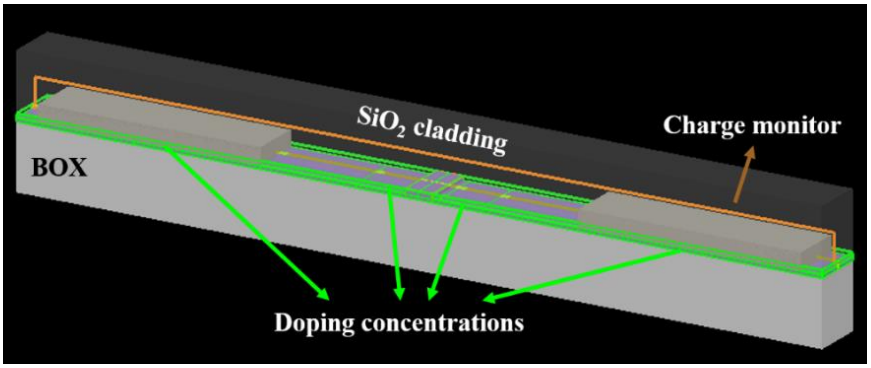

Fig. 2-9. Carrier distribution simulation in lateral PN junction using Lumerical DEVICE.

2-9 shows the simulation structure, where positive voltages are applied on the N++ doping area to make the PN junction reverse biased, and a charge monitor saves the carrier distributions. In the simulation, reverse bias voltages from 0 to 10 V with a step of 0.25 V are applied.

Afterwards, the carrier distributions are imported into Lumerical MODE Solutions for simulation on the effective indices and propagation losses using the eigenmode solvers. Figure 2-10 shows the simulated results at various reverse bias voltages. The increase of the effective indices and decrease of losses are because that carriers are more depleted when applying higher reverse bias voltages. The modulation efficiency is directly related to the effective index change ΔN_{eff}, and it is approximate 4.7×10^{-5} at -4 V bias. At the same bias voltage of -4 V, the simulated propagation loss is 11.78 dB/cm.

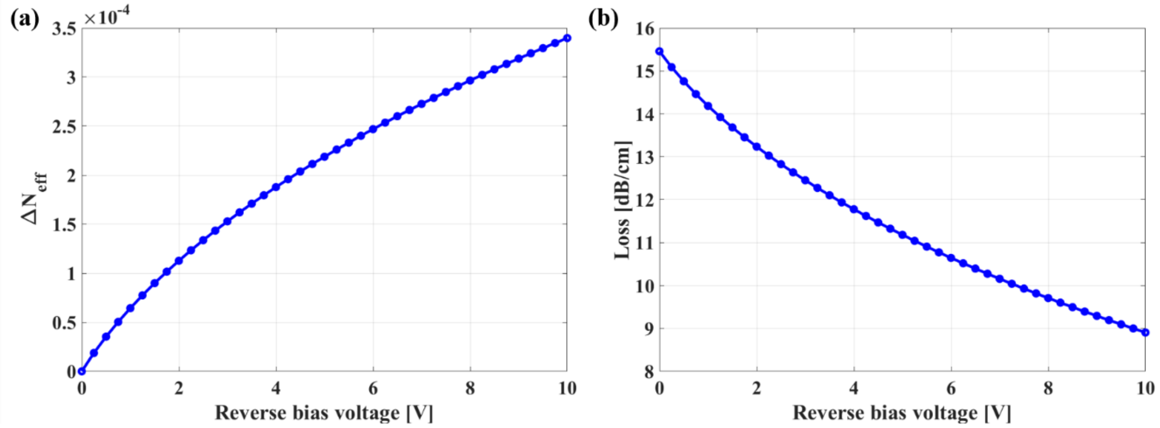

Fig. 2-10. Simulated (a) effective index changes and (b) optical waveguide losses in the lateral PN junction at various reverse bias voltages.

The junction capacitances are obtained by running two simulations at reverse bias voltages V and V + ΔV in Lumerical DEVICE, and then it is calculated using the following equation [73]:

$$C_{n,p} = \frac{Q_{n,p}(V+\Delta V) - Q_{n,p}(V)}{\Delta V} \tag{2.6}$$

where C_n and C_p are the capacitances due to the electrons (n) and holes (p), respectively, Q_n and Q_p are the charges obtained by integration of the carrier density using the charge monitor shown in Fig. 2-9. As shown in Fig. 2-11(a), the simulated junction capacitance decreases with the increasing reverse bias voltages due to the depleted electrical charges. It is 0.2 fF/μm at -4 V.

The junction resistances are also simulated based on the method in [73], which is splitting the simulation region into the n side and the p side, and then measuring the current of each side in response to the applied voltage. The simulated results are shown in Fig. 2-11(b). The junction resistances do not change much with the bias voltages, and it is approximately 0.62 Ω-cm under -4 V bias voltage.

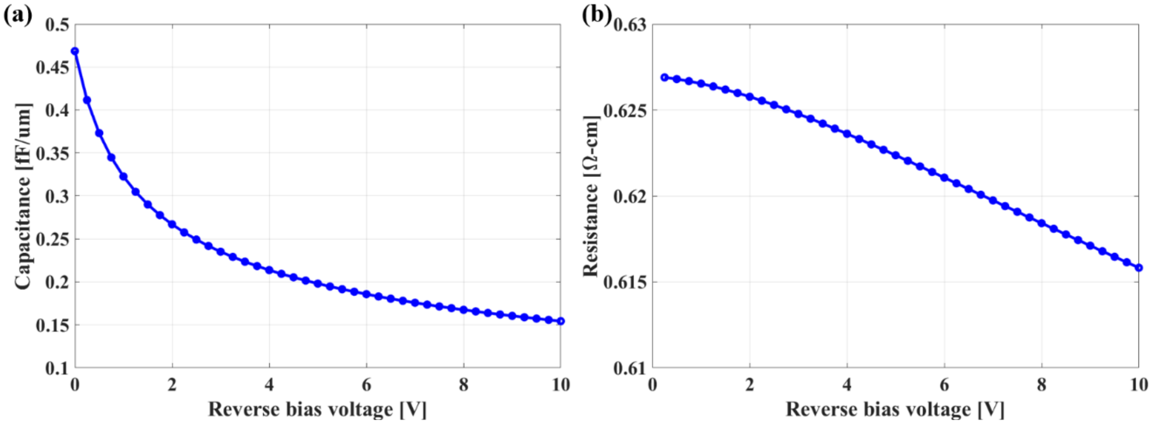

Fig. 2-11. Simulated PN junction (a) capacitances and (b) resistances of the lateral PN junction at various reverse bias voltages.

If only the PN junction capacitance C_j and resistance R_j are considered, the 3-dB cutoff frequency is calculated as [77]:

$$\mathrm{f}_c = \frac{1}{2\pi R_j C_j} \tag{2.7}$$

Figure 2-12 shows the 3-dB cutoff frequency at different bias voltages. It is 120 GHz at -4 V.

However, the 3-dB electrical bandwidth of a SiP modulator is always much smaller than the calculated cut-off frequency using Eq. 2.7. This is because in addition to the junction resistance and capacitance, there are also other elements in the circuit model of a SiP modulator, such as the capacitances induced by the metal pads and the resistance of the silicon substrate [17, 19].

It should be noted that the geometric parameters chosen in this section are used as an example to show how to simulate a PN junction. In the design process of a PN doped phase shifter, the geometry parameters are optimized to achieve the best modulation efficiency, propagation loss, junction capacitance and resistance, based on the doping concentrations and fabrication process of the foundry.

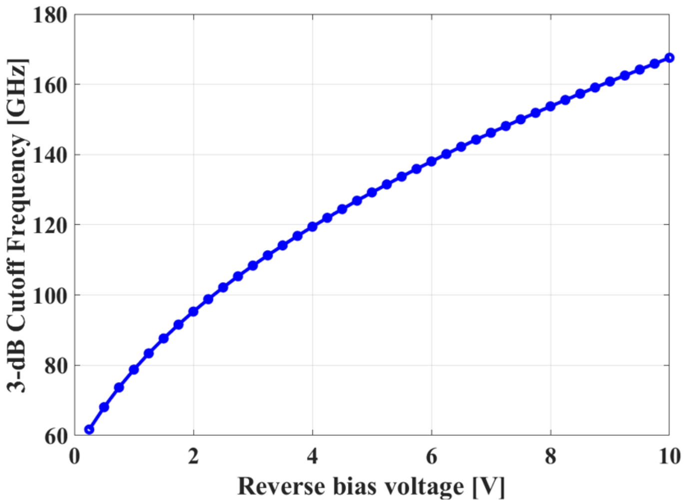

Fig. 2-12. Simulated 3-dB cutoff frequencies of the PN junction at various bias voltages.

2.2.4 Heater design

The heater for a SiP modulator is used for shifting the transmission spectrum, such as tuning the resonant wavelength of an MRM [78]. It is designed based on the thermo-optic effect, where the refractive index of silicon increases with the temperature. When applying a DC voltage on the heater, the change of temperature induces a refractive index change in the silicon waveguide [79]. The thermo-optic coefficient of silicon at room temperature 295 K is 1.87×10^{-4} K^{-1} [80].

Figure 2-13 shows the cross-section of a typical heater structure [18], where doping concentrations of N and N++ are applied. The heater is typically tens to hundreds of micrometers in length. Since the thermo-optic coefficient is in the magnitude of 10^{-4}, a small DC voltage on

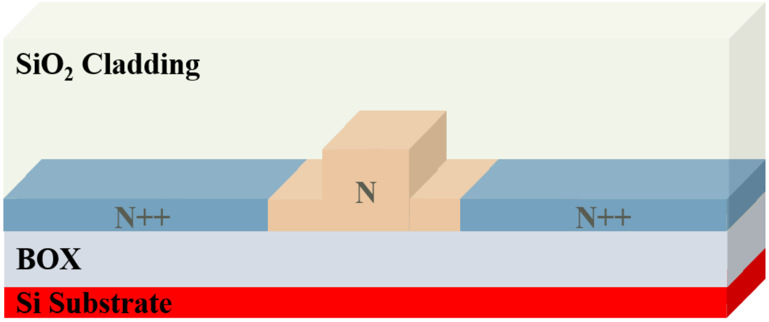

Fig. 2-13. Cross-section of a heater in SiP modulator design.

the heater will shift the transmission spectrum of SiP modulators. For example, the thermal tuning efficiency is 0.2 nm/mW in [78].

2.3 Review on SiP modulators

MRM and TWMZM are two SiP modulator structures that have attracted immense research interest and have been widely used in commercial products [61, 81]. There are also many other modulators, such as MIM [19], BGM [20], GeSi EAM [21, 22], SISCAP modulator [23] and those based on a combination of several different structures [25-39]. In this section, we review these SiP modulator structures, with a focus on the device structure, operating principle and the state of the art for IM/DD applications.

2.3.1 MRMs

The schematic structure of an all-pass single SiP MRM [18] is shown in Fig. 2-14(a). The modulation is via the dispersion plasma effect in the reverse-biased PN junction, and the thermal tuning is achieved by the thermo-optic effect, as introduced in Sections 2.2.3 and 2.2.4, respectively. In addition to the PN junction and heater, the radius, and the gap between the microring waveguide and the bus waveguide are also very important parameters that should be carefully designed. The model of an all-pass MRR [77] is shown in Fig. 2-14(b). The ring radius affects the round-trip phase change ϕ and the round-trip loss α. The gap influences the straight-through coupling coefficient σ and the cross-coupling coefficient κ, where $\sigma^2 + \kappa^2 = 1$.

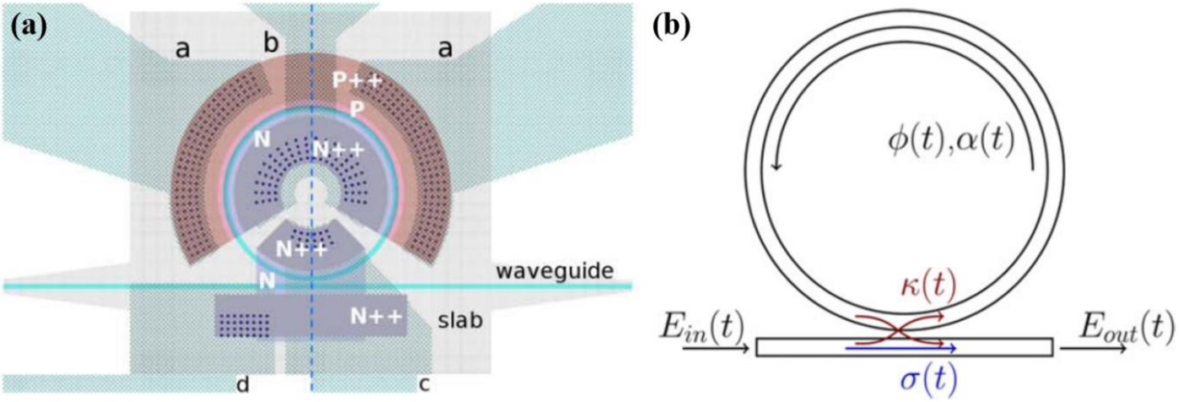

Fig. 2-14. (a) Schematic structure [18] and (b) model [77] (©2015 IEEE) of an all-pass MRR.

With an input electric field E_{in}, the output electric field of an all-pass single MRR is [82]:

$$E_{\text{out}} = E_{in} \frac{-\Lambda + \sigma e^{-j\phi}}{-\Lambda\sigma + e^{-j\phi}} \tag{2.8}$$

where Λ is the round-trip attenuation and $\Lambda^2 + \alpha^2 = 1$, which means Λ = 1 when there is no loss. The round-trip phase change is defined as [83]:

$$\phi = 4\pi^2 \mathrm{n}_{\text{eff}} \frac{R}{\lambda} \tag{2.9}$$

in which n_{eff} is the effective index of the MRR waveguide, R is the radius and λ is the wavelength. The output power of the MRR is [83]:

$$P_{out} = | E_{out} |^2 = \frac{\Lambda^2 + \sigma^2 - 2\Lambda\sigma\cos\phi}{1 + \Lambda^2\sigma^2 - 2\Lambda\sigma\cos\phi} | E_{in} |^2 \tag{2.10}$$

Figure 2-15 shows the transmission spectrum of an all-pass single MRR with a 40-µm radius. The round-trip attenuation Λ is 0.9785, which corresponds to a 10 dB/cm propagation loss. The straight-through coupling coefficient σ is set as 0.9760, and the effective index is 2.5673. The optical IL is defined as the maximum transmission. The resonant wavelength is where the output power is at minimum, and in this case ϕ = 2πm and m is an integer. The ER is the ratio between the IL and the transmission at resonance. The free spectral range (FSR) is the difference between

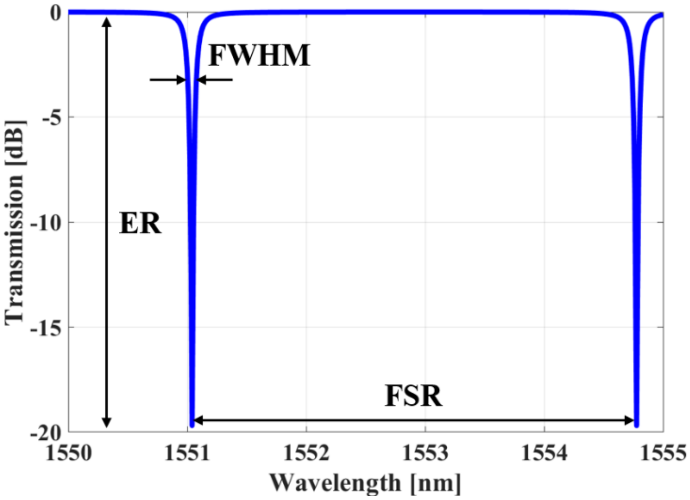

Fig. 2-15. Transmission spectrum of an all-pass MRR.

the two resonances, and the full-width at half maximum (FWHM) is defined as the optical bandwidth at -3 dB transmission with respect to the IL. The quality (Q) factor of an MRR is calculated as the resonant wavelength over the FWHM.

At resonance, the output power is [83]:

$$P_{\text{out}} = \frac{(\Lambda - \sigma)^2}{(1 - \Lambda\sigma)^2} |E_{in}|^2 \tag{2.11}$$

Based on this equation, there are three coupling conditions defined as follows. When the round-trip attenuation Λ is equal to the straight-through coupling coefficient σ, P_{out} becomes zero and it is called the critical-coupling condition [82]. When $\Lambda > \sigma$, the MRR is over-coupled and when $\Lambda < \sigma$, it is under-coupled.

Figure 2-16 shows the phase responses of an over-coupled MRM and an under-coupled MRR, both with R = 40 μm, Λ = 0.9785 and n_{eff} = 2.5673. The straight-through coupling coefficients for the simulation of the two MRRs are chosen to be 0.9760 and 0.9780, respectively. In the over-coupled condition, the phase shift across the resonance is 2π, but that in the under-coupled condition is much smaller, which is typically less than π [77].

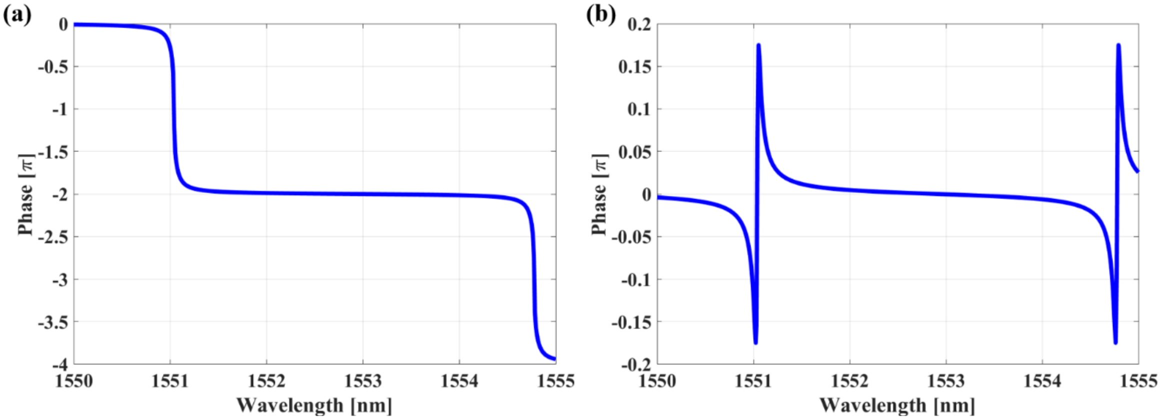

Fig. 2-16. Phase responses of (a) an over-coupled MRR and (b) an under-coupled MRR.

When applying DC reverse bias voltages on the PN junction of an MRM, n_{eff} changes so the transmission spectrum shifts. Figure 2-17 shows the measured transmission spectra of an over-coupled MRM [18] and an under-coupled MRM [84] under various reverse biases. Due to the carrier-depletion phenomenon, the propagation loss in the waveguide becomes smaller when applying higher reverse bias voltages. Therefore, the round-trip loss α is smaller, which means the IL of the MRM is smaller and the round-trip attenuation Λ is larger. With the straight-through coupling coefficient unchanged, the over-coupled MRM is further away from the critical-coupling condition, but the under-coupled MRM is closer to the critical-coupling condition. As a result, the ER of the over-coupled MRM becomes smaller with the applied reverse biases, but that of the under-coupled MRM is larger. As shown in Figs. 2-17(a) and 2-17(b), these phenomena are obvious.

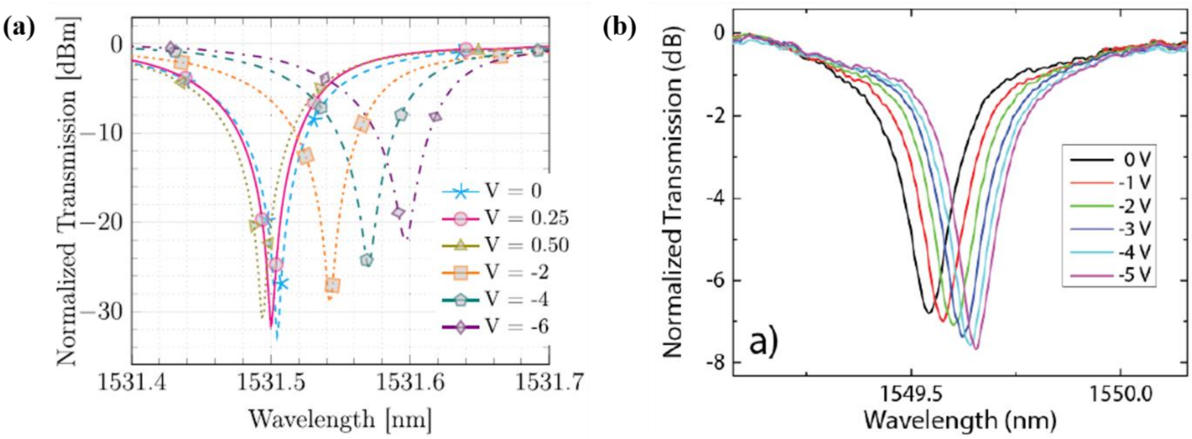

Fig. 2-17. Transmission spectra of (a) an over-coupled MRM [18] and (b) an under-coupled MRM [84] when applying various reverse bias voltages on their PN junctions.

The modulation efficiency of the MRMs is characterized using the resonance shift at a certain bias voltage. For example, as shown in Fig. 2-17(a), the resonant wavelength shift at -4 V is approximately 66 pm, so the modulation efficiency is 16.5 pm/V at -4 V. Similarly, the modulation efficiency of the measured transmission spectra in Fig. 2-17(b) is around 3 pm/V. The OMA is defined as OMA = $P_{V1} – P_{V0}$, where P_{V1} and P_{V0} are the transmitted powers of the MRM at a certain wavelength under the bias voltages V_1 and V_0, respectively.

Another important FOM of SiP modulator is the EO bandwidth. For MRM, it is determined by the optical bandwidth, which is the FWHM, and the electrical-electrical (EE) bandwidth. Figure 2-18 presents the small-signal characterization of a SiP MRM [17]. Since the small RF signals are mostly reflected, the EE S_{11} magnitudes are large. The electrical bandwidth increases with the applied reverse bias voltages because of the reduction of the junction capacitance. A circuit model of MRM is also shown in the Fig. 2-18(a). In addition to capacitance C_j and resistance R_j of the PN junction, there are also capacitance of the metal pads C_p, capacitance C_{sub} and resistance R_{sub} of the silicon substrate. Therefore, the electrical bandwidth is much smaller than the calculated 3-dB cutoff frequency of the PN junction, as analyzed in Section 2.2.3. As shown in Fig. 2-18(b), the EO bandwidth of the MRM also depends on the modulation wavelength. At a wavelength closer to the resonance, light is easier to be trapped and has a longer photon lifetime [17]. Therefore, at a larger detuning from the resonant wavelength, the EO bandwidth is higher and an optical peaking effect is also observed in the EO S_{21} response [85]. However, the OMA at large wavelength detuning from the resonance is smaller than that close to the resonance, as shown in Fig. 2-17. Therefore, a trade-off between OMA and EO bandwidth should be considered [86].

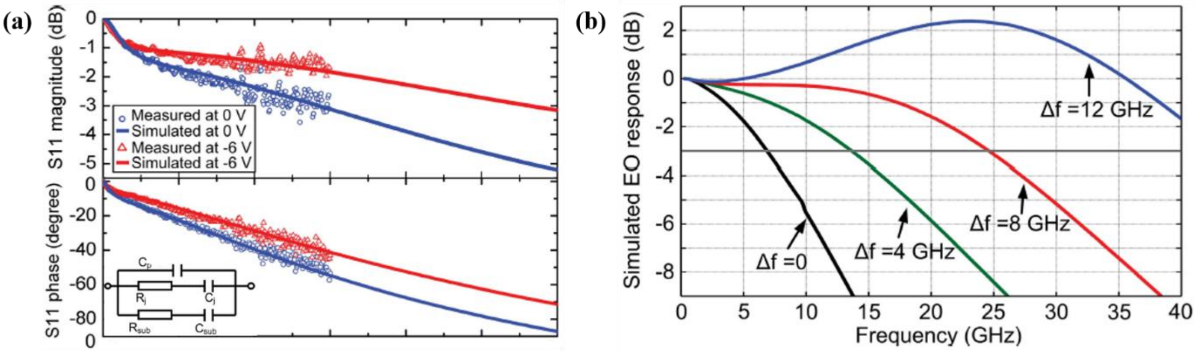

Fig. 2-18. (a) EE S_{11} and (b) EO S_{21} responses of a SiP MRM [17]. (©2012 IEEE)

Table 2 reviews the state of the art of C-band carrier-depletion SiP MRMs for IM/DD applications, which are OOK modulation of at least 40 Gb/s [17, 87-89], PAM-4 based on a single MRM [18, 90, 91] and multiple channels modulation for WDM applications [92]. The Q-factors, static ERs, modulation efficiencies, peak-to-peak voltages and bit rates are listed as they the important FOMs for the SiP modulators. The EO bandwidths and the BERs are not listed since most of the references in Table 5 do not report on these two FOMs.

In conclusion, there are three aspects of designing a SiP MRM. First, the geometry and doping of the PN junction are designed to achieve a large modulation efficiency and a high 3-dB cutoff frequency. These designs also influence the effective index and propagation loss in the MRM waveguide. Second, the geometric parameters of the ring resonator, such as the radius and the

Table 2. The state of the art of SiP MRMs for IM/DD applications.

Ref.	Q-factor	Static ER	Modulation efficiency	Modulation format	V_{pp}	Bit rate
[17]	~ 8,000	11 dB	16 pm/V	OOK	3 V	44 Gb/s
[87]	~ 4,000	35 dB	28 pm/V	OOK	2 V	40 Gb/s
[88]	~ 7,000	> 30 dB	/	OOK	1.4 V	40 Gb/s
[89]	~ 20,000	16 dB	10 pm/V	OOK	/	40 Gb/s
[90]	~14,000	~ 20 dB	13 pm/V	PAM-4	1 V	24 Gb/s
[91]	~13,500	~ 20 dB	10 pm/V	PAM-4	2 V	20 Gb/s
[18]	~18,000	35 dB	16 pm/V	PAM-4	3.5 V	80 Gb/s
[92]	~5,000	/	25 pm/V	8 channels WDM OOK	4.8 V	320 Gb/s

gap from the bus waveguide, are carefully chosen. They affect the coupling condition of the MRM, which further affects the phase response and the optical bandwidth. Third, the experimental designs, including selecting the bias wavelength for the trade-off between EO bandwidth and the OMA, and choosing the peak-to-peak voltage and bias voltage of the RF signals to achieve a low power consumption, are also very important. In addition, the heater for thermally tuning the resonant wavelength of the MRM also plays a significant role, especially in the WDM applications. It occupies most of the power consumption in the modulation of a SiP MRM [93]. Currently, resonance locking based on monitoring photodetectors (PDs) [94] or a feed-back digital circuit [95] has been reported.

2.3.2 TWMZMs

Based on the driving configuration, single SiP TWMZMs can be categorized into two types: single-drive where RF signals are applied to modulate only one of the MZI arms [96], and dual-drive where both the MZI arms are modulated [97]. Push-pull (PP) operation is a special case. It can be achieved either by a dual-drive scheme with differential RF signals [98], or by a single-drive scheme on a TWMZM where the PN junctions on each arm are designed in opposite direction and connected in series [99]. The latter one is called series push-pull (SPP) operation. Figure 2-19 shows the schematic layout and PN junction design of a SiP SPP TWMZM [6]. As shown in Fig. 2-19 (a), the optical waveguide is designed to be an imbalanced MZI. Therefore, destructive interference is achieved at a certain wavelength. The FSR is determined by the imbalance length ΔL and the group index n_g based on the following equation [100]:

$$FSR=\frac{\lambda^2}{n_g \Delta L} \tag{2.12}$$

The series design by connecting two PN junctions in a back-to-back configuration for achieving SPP operation, as shown in Fig. 2-19(b), increases the junction capacitance and as a result, the velocity of the microwave increases [6].

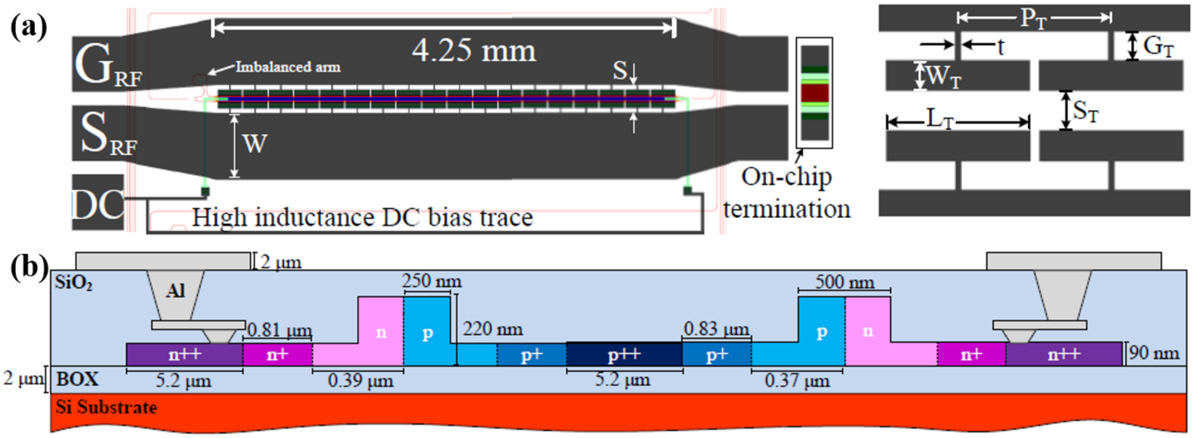

Fig. 2-19. (a) The schematic layout, the T-shaped electrodes extension, and (b) the PN junction design of a SiP SPP TWMZM [6].

Figure 2-20(a) shows the transmission spectra of the TWMZM [6]. Like SiP MRMs, the IL, static ER, FSR and FWHM are obtained from the transmission spectrum. When applying reverse bias voltages, its resonant wavelength is shifted due to the effective index change in the MZI waveguide. For TWMZMs, resonance shift is not an appropriate FOM to evaluate its modulation efficiency. Instead, $V_\pi L$, which is the required voltage to achieve a π phase shift for a given length L, is typically used. It is calculated as [101]:

$$V_\pi L=\frac{\pi V_{bias} L}{\Delta\varphi} \tag{2.13}$$

where V_{bias} is the applied bias voltage, and the phase shift Δφ at V_{bias} is [101]:

$$\Delta\varphi=\frac{2\pi\Delta\lambda}{FSR} \tag{2.14}$$

in which Δλ is the resonant wavelength shift at V_{bias}.

The $V_{\pi}L$ of the two diodes in the TWMZM [6] are calculated from the measured transmission spectra in Fig. 2-20(a), and are shown in Fig. 2-20(c). The V_{π} for diode 1 is 7 V, but that for diode 2 is larger than 10 V. This difference is mainly induced by the variations in the fabrication processes.

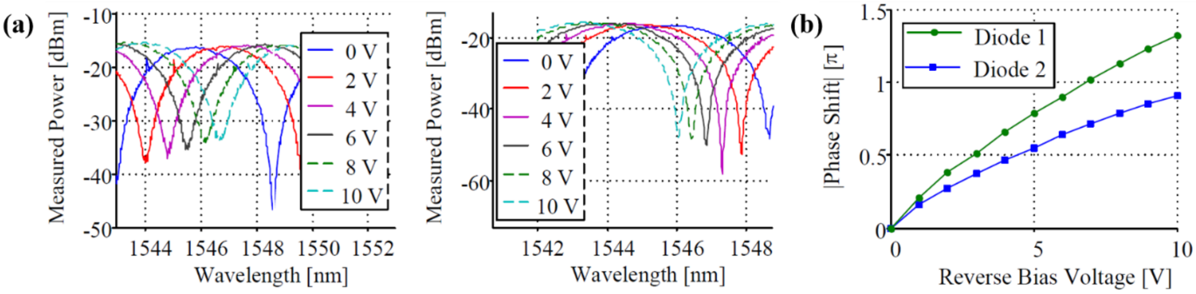

Fig. 2-20. (a) Measured transmission spectra and (b) calculated $V_{\pi}L$ of the two diodes in the TWMZM under various reverse bias voltages [6].

Figure 2-21 shows the small-signal EE and EO responses of the TWMZMs [6]. Different from that of the MRMs, the EE S_{11} magnitude is lower than -10 dB from DC to 50 GHz, since the electrical signals are mostly transmitted because of the travelling-wave electrodes. Therefore, the EE S_{21} magnitude is large, as shown in Fig. 2-21(b). The 6.4-dB point is beyond 50 GHz at -4 V bias voltage. The 3-dB EO bandwidth is 41 GHz at -4 V, as shown by the EO S21 magnitude in Fig. 2-20(c). When applying reverse bias voltages on the PN junction, the EE and EO

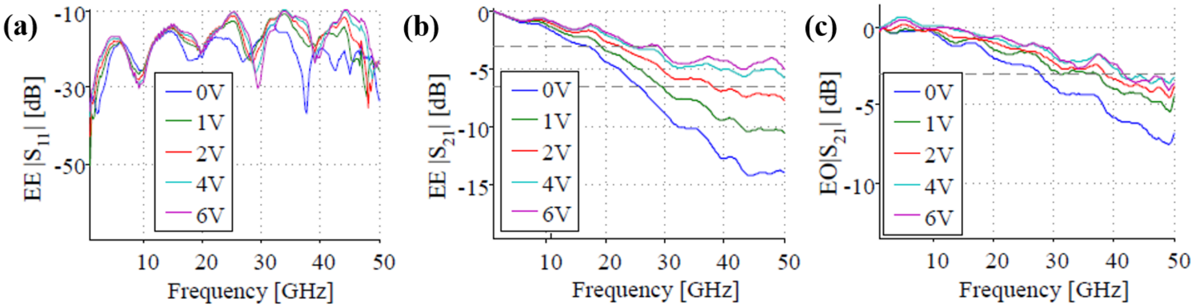

Fig. 2-21. (a) EE $|S_{11}|$, (b) EE $|S_{21}|$ and (c) EO $|S_{21}|$ of the TWMZM [6].

bandwidths both increase as the junction capacitance decreases. If there is no group velocity mismatch, the EE 6.4-dB bandwidth should be equal to the EO 3-dB bandwidth [66, 102]. In [6], this mismatch is 13% at -4 V bias, so the two bandwidths are different.

Table 3 reviews the state of the art of C-band carrier-depletion single SiP TWMZMs for IM/DD applications, including OOK modulation of over 40 Gb/s [66, 97, 103, 104, 105] and high order modulation formats such as PAM-4 [6, 7, 35] and PAM-8 [6]. It should be noted that the $V_\pi L_\pi$ and the EO bandwidths are those reported in the references, and they are at different bias voltages but not listed in this table.

Table 3. The state of the art of SiP TWMZMs for IM/DD applications.

Ref.	Length	$V_\pi L_\pi$	EO bandwidth	Modulation format	V_{pp}	Bit rate	BER
[6]	4.25 mm	3.2 V-cm	41 GHz	PAM-2	4.3 V	70 Gb/s	1.57×10^{-3}
				PAM-4	5.21 V	112 Gb/s	4.92×10^{-4}
				PAM-8	6.73 V	112 Gb/s	3.16×10^{-3}
[7]	4.2 mm	3.57 V-cm	35 GHz	PAM-2	2.2 V	64 Gb/s	$\sim 4 \times 10^{-4}$
				PAM-4		112 Gb/s	3.7×10^{-3}
[35]	2 mm	/	30.2 GHz	PAM-4	5 V	64 Gb/s	6.6×10^{-5}
[66]	3 mm	2.43 V-cm	30 GHz	OOK	1.6 V	40 Gb/s	/
[97]	/	/	55 GHz	OOK	5.32 V	70 Gb/s	/
[103]	3.5 mm	1.93 V-cm	27 GHz	OOK	1.6 V	40 Gb/s	$< 1 \times 10^{-12}$
[104]	0.95 mm	2.2 V-cm	26 GHz	OOK	7 V	40 Gb/s	/
[105]	3 mm	1.85 V-cm	37 GHz	OOK	3.5 V	50.5 Gb/s	/

2.3.3 Other modulator structures

Besides MRMs and TWMZMs, there are other modulator structures for IM/DD applications, such as MIM [19], BGM [20], GeSi EAM [21, 22], and SISCAP modulator [23]. As they are not directly related to this thesis, the details of device design or operating principle are not presented in this section. The performances of the SiP modulators based on single SiP modulator structures, excluding the single MRMs and the single TWMZMs, are concluded in Table 4.

As introduced in Section 1.2, SiP modulators based on a combination of an MZI and MRRs have also been reported to achieve wide operating wavelength range [25], thermal stability [26] and high linearity [27]. These structures are also used for OOK modulation [28, 29], BPSK [29], QPSK [30] and PAM-4 [31]. Their performances are listed in Table 5.

Table 4. Performances of SiP modulators based on a single structure (excluding single MRMs and single TWMZMs).

Ref.	Modulator structure	EO bandwidth	Modulation format	V_{pp}	Bit rate	BER
[19]	MIM	23.2 GHz (-4 V bias)	OOK	/	40 Gb/s	/
[20]	BGM	/	OOK	4.5 V	55 Gb/s	~ 2×10^{-4}
			PAM-4		60 Gb/s	~ 6×10^{-4}
[21]	GeSi EAM	> 50 GHz	OOK	1.5 V	56 Gb/s	/
[22]	GeSi EAM	/	OOK	/	100 Gb/s	/
[23]	SISCAP modulator	/	OOK	1 V	40 Gb/s	/

Table 5. Performances of the SiP modulators based on a combination of MZI and MRR.

Ref.	Modulator structure	Design Purpose	Modulation format	Bit Rate
[25]	10 MRMs on each arm of the balanced MZI	Wide operating λ range	OOK	10 Gb/s
[26]	1 MRM on one arm of the unbalanced MZI	Athermal modulation	OOK	2 Gb/s
[27]	1 MRM on each arm of the balanced MZI	High linearity	/	/
[28]	1 MRM on one arm of the balanced MZI	OOK modulation	OOK	10 Gb/s
[29]	1 MRM on each arm of the balanced MZI	Low-chirp OOK modulation	OOK	10 Gb/s
		BPSK modulation	BPSK	10 Gb/s
[30]	1 MRM on each arm of the balanced MZI	QPSK modulation	QPSK	56 Gb/s
[31]	MZI-assisted ring modulator	PAM-4	PAM-4	25 Gb/s

In addition, DAC-less and DSP-free PAM-4 signals generation based on MZI-assisted ring modulator [31], TWMZMs [32-35], cascaded dual MRMs [36], segmented MRM [37], push-pull segmented SISCAP modulators [38] and dual parallel GeSi EAMs [39] have been demonstrated. Table 6 summarizes their performances, including the peak-to-peak voltages (Vpp), the lengths of the pseudo-random binary sequence (PRBS), the bit rates, the transmission distances and the BERs. Moreover, 114 Gb/s DAC-less PAM-8 generation with DSP [106] has also been presented.

In conclusion, SiP modulators based on various structures for IM/DD short reach transmission systems have been reported, which further proves the capability of silicon photonics in intra-data center applications.

Table 6. Performances of DAC-less and DSP-free PAM-4 SiP modulators. [47]

Ref.	Modulator structure	V_{pp}	PRBS	Bit rate	Transmission	BER
[31]	MZI-assisted ring modulator	3 V, 3 V	31	25 Gb/s	0	/
[32]	Segmented TWMZM	4.8 V, 4.8 V	31	100 Gb/s	1 km	$< 3.8 \times 10^{-3}$
[33]	Dual parallel TWMZMs	2 V, 4 V	/	100 Gb/s	2 km	$< 4.4 \times 10^{-3}$
[34]	TWMZM	1.5 V, 3 V	/	50 Gb/s	0	2.2×10^{-6}
[35]	TWMZM	5 V	15	64 Gb/s	0	6.6×10^{-5}
[36]	Cascaded dual MRMs	1 V, 1 V	9	30 Gb/s	0	4×10^{-3}
[37]	Segmented MRM	4.4 V, 4.4 V	15	40 Gb/s	0	/
[38]	Push-pull segmented SISCAP modulators	2 V, 2 V	31	56 Gb/s	0	/
[39]	Dual parallel GeSi EAMs	1.1 V, 2.2 V	7	112 Gb/s	2 km	1.4×10^{-3}

2.4 Conclusion

In this chapter, the fundamentals of SiP modulators are reviewed. First, the plasma dispersion effect, which is the basic of SiP modulation, is introduced. Based on it, the design methods of passive silicon waveguide, lateral PN junction and heater are explained. Then the device structure, design method, operating principle and FOMs of two typically used SiP modulator structures, which are the MRMs and the TWMZMs, are elaborated. Then the other modulator structures are also reviewed in this chapter.

Chapter 3

Push-pull operation of dual parallel MRMs

3.1 Overview

As introduced in Section 2.3.1, MRMs are key component among SiP modulators. They are of immense research interest as they have compact size and intrinsic filtering ability for the applications in WDM schemes. Currently, SiP MRMs have already been applied in a commercial product [62]. However, in optical communication links where CD is not negligible, the frequency chirp of MRMs [107] limits their applications in transmission over long distances, e.g. 10 km or 20 km. There are two typical ways to compensate CD: dispersion compensation fibers (DCFs) and DSP. However, optical amplification is required in the transmission links where DCFs are used, as they introduce excess loss [108]. DSP-based CD compensation needs access to the modulated phase information on the receiver side [109], therefore it cannot be applied in the IM/DD systems. Recently, SiP MRMs for OOK modulation at 10 Gb/s with low chirp [29, 110] and negative chirp [111] have been reported.

In this chapter, high-speed low-chirp PAM-4 transmission based on the push-pull operation of dual parallel MRMs is demonstrated. This chapter is based on the author’s work in [41, 42], and it is organized as follows. The device structure design, PN junction design and fabrication method are described in Section 3.2. Then the push-pull operation principle is presented in Section 3.3, with simulation results shown in Section 3.3.1 and chirp measurement reported in Section 3.3.2 to prove the advantages of this principle. Afterwards, the device characterization is demonstrated in Section 3.4, including the measured DC transmission spectra in Section 3.4.1, as well as the small-signal EE and EO responses in 3.4.2. In Section 3.5, large-signal modulation without any method for CD compensation is presented. OOK modulation and comparison to the performance of a single MRM with the same design parameters are presented in Section 3.5.1. High-speed low-chirp PAM-4 transmission is shown in Section 3.5.2. Finally, this chapter is concluded in Section 3.6.

3.2 Device design and fabrication

For push-pull operation to achieve a low-chirp modulation, the dual MRMs are designed in parallel and assisted in a balanced MZI. Figure 3-1 shows the schematic structure of the device. The 500-nm × 220-nm silicon waveguide is on a 90-nm thick slab. The MRMs are designed to be identical. They have the same radius of 20 μm and the same gap of 200 nm from the MZI waveguide. The balanced MZI is 230 μm in length. On one of the MZI arms, a 125-μm heater is designed for phase tuning to compensate for any fabrication deviations and make the MZI perfectly balanced. Around 75% of the MRM is doped to form a lateral PN junction for carrier-depletion modulation, as elaborated in Section 2.2.1 and Section 2.2.3. The remaining 25% is designed as a heater for resonant wavelength tuning using the thermos-optic effect, as explained in Section 2.2.4. As shown in Fig. 3-1, light travels through the MZI, while differential RF signals are applied on the PN junctions of the two MRMs simultaneously. A DC voltage is applied on the heater of one MRM to tune its resonances closer to that of the other MRM.

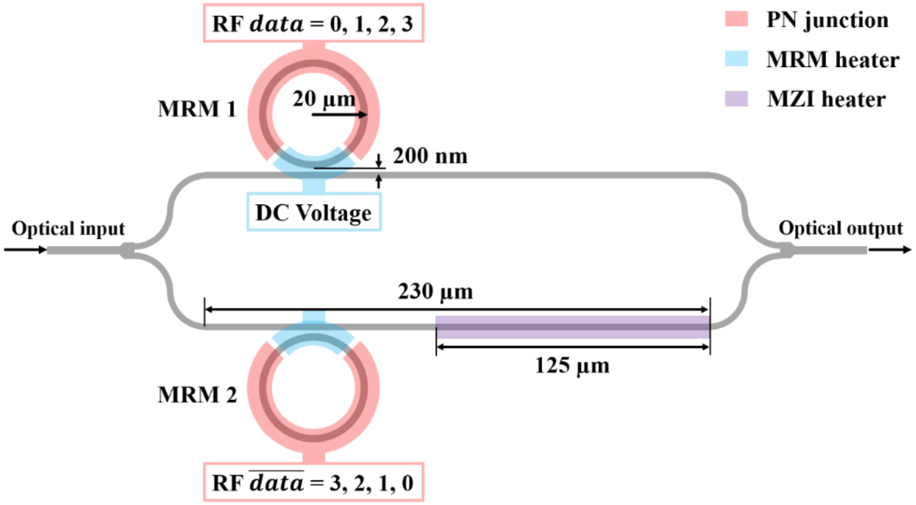

Fig. 3-1. Schematic layout of the dual parallel MRMs for push-pull operation [41].

As shown in Fig. 3-2(a), there are four doping concentrations applied in the lateral PN junction, which are 5 × 10^{17} cm^{-3} for P, 3 × 10^{17} cm^{-3} for N, 1 × 10^{20} cm^{-3} for P++ and N++ [66]. Therefore, the PN junction is designed to be symmetric for taking the best advantages of the holes, as analyzed in Section 2.2.3. The light PN doping in the rib waveguide is used for reducing the optical scattering loss, and the high P++/N++ doping in the slab waveguide is for ohmic contact with the metal pads. The heater design is shown in Fig. 3-2 (b). Similarly, and the high N++ doping is used for contact with metal pads. The light N doping is applied for thermo-optic tuning of the waveguide effective index.

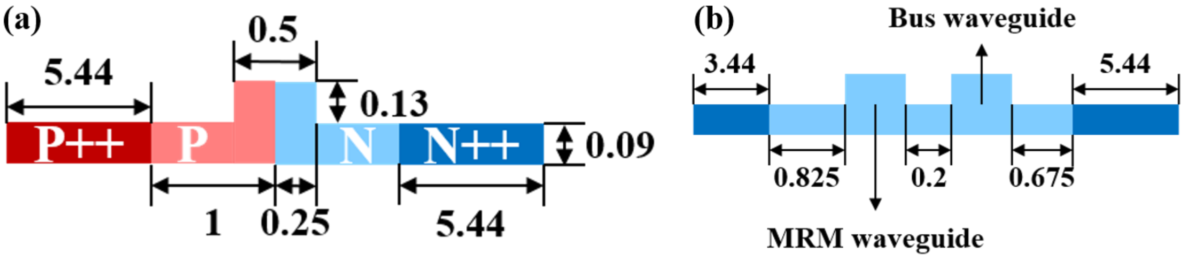

Fig. 3-2. (a) PN junction design and (c) heater design of the MRMs.

The device was fabricated at IME A*STAR using a fabrication process described in [112]. The substrate is an 8-inches 220-nm SOI wafer with a 2-µm BOX. The 90-nm slab, 130-nm slab, and 220-nm rib waveguides are formed using three anisotropic etch steps, as shown in Fig. 2-2 and introduced in Section 2.2.2. Boron and phosphorus are implanted in the silicon waveguides. Afterwards, a rapid thermal anneal of 1030°C for 5 seconds is followed to active the dopants. Finally, two levels of contact vias and aluminum pads are fabricated.

The micrograph of the fabricated device is shown in Fig. 3-3(a). The total footprint, dominated by the metal bond pads, is 0.61 mm × 0.61 mm. A DC voltage for tuning the resonances is applied using a GS probe on the G and DC pads, and the differential RF signals are applied using a GSGSG probe on the G, $\overline{RF}$, G, RF and G pads. The vertical GCs, which are used for optical input and output, are not shown in the micrograph. It should be noted that as the GC is designed only for TE polarization, the input light is kept as TE polarized in all the experiments in this thesis. For comparison, a single MRM with the same design parameters was also fabricated in the same fabrication run. Its microimage is demonstrated in Fig. 3-3 (b), in which the PN doping areas, aluminum layers and the contact vias are clearly shown.

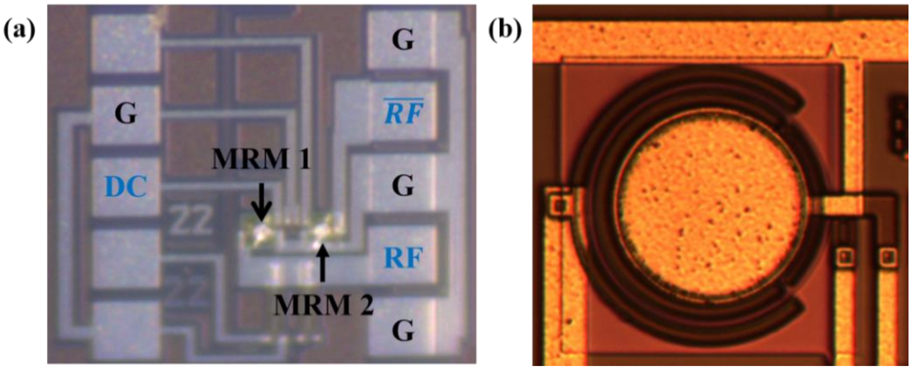

Fig. 3-3. Micrographs of (a) the dual parallel MRMs for push-pull operation, and (b) a single MRM with the same design parameters for comparison.

3.3 Operating principle

The push-pull operation is proposed for low-chirp modulation, so that the optical signals can transmit over a longer distance of SSMF without any CD compensation method. It is desirable for IM/DD systems where DSP for CD compensation cannot be applied, and for reducing the optical power consumption without implementing DCFs. In this section, the operating principle is explained by system-level simulation and then verified by chirp measurement using 10 Gb/s push-pull OOK modulation of the dual parallel MRMs.

3.3.1 Simulation

As shown in Fig. 3-1, to achieve the push-pull operation of the device, RF data levels 0, 1, 2, 3 and inverted RF data levels 3, 2, 1, 0 are applied on MRM 1 and MRM 2, respectively. To clearly demonstrate the operating principle, we simulate the power transmission and phase responses of both the two independent MRMs and the push-pull dual parallel MRMs in Lumerical Interconnect [113]. In the simulation, we intentionally set the resonant wavelengths of the two MRMs slightly different. Since there are always deviations between what is designed and what is really fabricated, the difference in resonant wavelengths is usually observed in the measurement, even though the two MRMs are designed to be identical. This can also be achieved by applying a DC voltage on the heater of one MRM in the experiment.

As shown in Fig. 3-4(a), when any of the four-level differential data is applied, the two MRMs have almost the same power transmission T at the marked operating wavelength λ. However, as shown in Fig. 3-4(b), their phases φ have the same magnitudes but opposite signs. In a word, $T_{MRM1,\,i} = T_{MRM2,\,i}$ and $\varphi_{MRM1,\,i} = -\varphi_{MRM2,\,i}$ (i = 1, 2, 3, 4) when applying differential RF signals on the two MRMs.

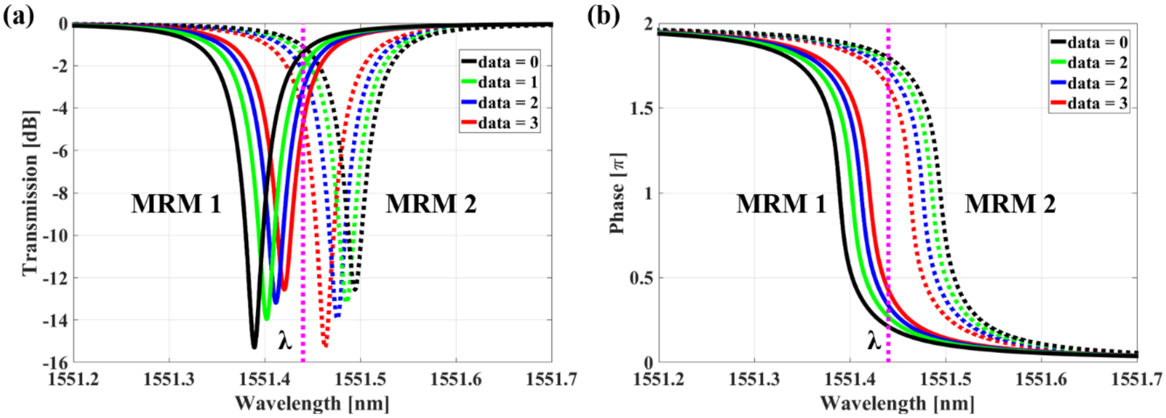

Fig. 3-4. Simulated (a) power transmission and (b) phase responses of the two MRMs.

The power transmission of the dual parallel MRMs in a balanced MZI is characterized by the following equation:

$$T_{\text{i}}=\frac{1}{4}\left|\sqrt{T_{MRM\,1,i}}\,e^{j\varphi_{MRM\,2,i}}\right.\left.+\sqrt{T_{MRM\,2,i}}\,e^{j\varphi_{MRM\,2,i}}\right|^{2}\ (\text{i}=1,2,3,4) \tag{3.1}$$

Since the two MRMs have the same magnitudes but opposite phases at the operating wavelength at any applied differential data level i, the device has larger power transmission than any of the MRMs, and the total phase response should be zero.

This is further proved by the following system-level simulation in Interconnect. As shown in Fig. 3-5(a), when the four levels of differential RF data applied on the two MRMs simultaneously, the device has four levels of power transmission at the operating wavelength λ, which are 0.033, 0.173, 0.327 and 0.477, respectively. The reasonable even spacings of these four levels are desirable for generating PAM-4 optical signals. The simulated phase responses when various differential RF data levels are applied on the dual MRMs are shown in Fig. 3-5(b). To quantitatively estimate the chirp performance of a modulator, the chirp parameter, or α parameter is defined using the following equation [114]:

$$\alpha = 2I\frac{\mathrm{d}\varphi/dt}{dI/dt} \tag{3.2}$$

in which the modulated optical intensity I and the phase φ are both functions of the time t. Since the applied voltage V also varies with time, Eq. 3.2 can be re written into:

$$\alpha = 2I\frac{\mathrm{d}\varphi/dV}{dI/dV} \tag{3.3}$$

As shown in Fig. 3-5(b), the phases at λ are all zero, no matter what RF data value that is applied. Thus, dφ/dV in Eq. 3.3 is zero and the simulated α-parameter is also zero. It proves that the device is capable of zero-chirp modulation. It should be noted that the phase is zero only at the operating wavelength λ. At a high modulation speed, e.g. 80 Gb/s, the single side band is 40 GHz. It corresponds to a wavelength range of approximately 0.32 nm, and the α-parameter in this range is not always zero. But compared to the phase response of a single over-coupled MRM, as shown in Fig. 3-4(b), the phase shown in Fig. 3-5(b) and the related dφ/dV are much smaller. Therefore, the push-pull operation of the dual MRMs decreases the chirps in the modulation, even though the α-parameter is not always zero at a high modulation speed.

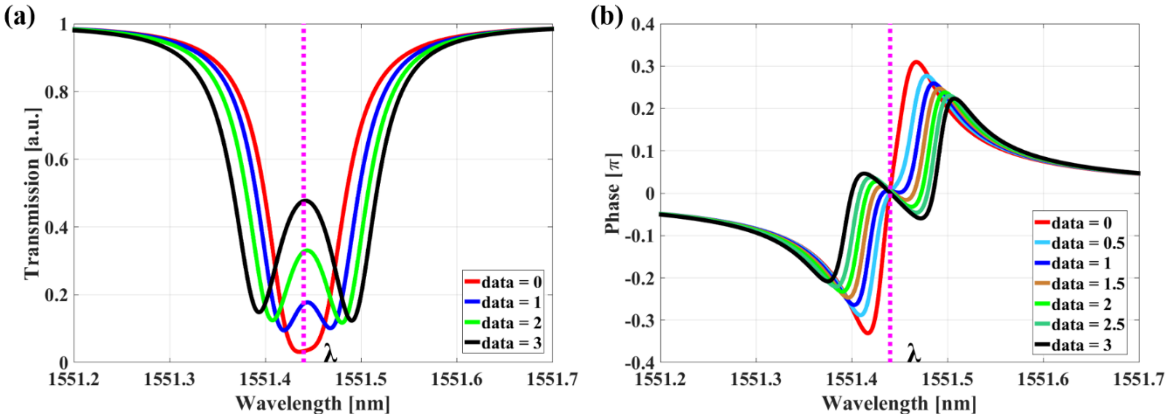

Fig. 3-5. Simulated (a) power transmission and (b) phase responses of the dual parallel MRMs in the push-pull operation. [41]

As shown in Fig. 3-5(a), the largest transmission is 0.477 in the simulation. It means the modulation loss, which is defined as the IL at the operating wavelength and the highest level after modulation, i.e., ‘11’ for PAM-4, is approximately 3.2 dB. It should be noted the RF data and the MRM model are used as an example to explain the push-pull operating principle. The modulation loss can be reduced by applying differential RF signals with larger peak-to-peak voltages, and tuning the resonant wavelengths of the two MRMs further separated. Theoretically, the modulation loss can be 0 dB if the resonances of the two MRMs at ‘11’ level are totally separated. Meanwhile, the phase response at the operating wavelength is always zero, which guarantees the zero-chirp modulation of the device in the push-pull operation.

3.3.2 Chirp measurement

The chirp performance of the device is characterized by measuring the constellation diagrams and the chirp parameters of the modulated optical signals by an APEX AP-2443B complex optical spectrum analyzer (OSA). As a clock input at 10 GHz is necessary for the measurement using the complex OSA, we use OOK modulation of the device in a push-pull configuration at 10 Gb/s. Figure 3-6 shows the experimental setup. Differential 16-bits PRBS were generated by an SHF 12103A bit pattern generator (BPG). Afterwards, the RF signals were amplified and synchronized using a RF delay line. The peak-to-peak voltages of the RF signals were measured in a 50 Ω system, and they were both 1.8 Vpp. Using 65 GHz bias tees, the DC bias voltages of −2 V were applied on the two MRMs together with the RF signals. A DC voltage of 1.08 V was applied on the MRM 1 heater to tune its resonance closer to that of the MRM 2. A 14-dBm laser

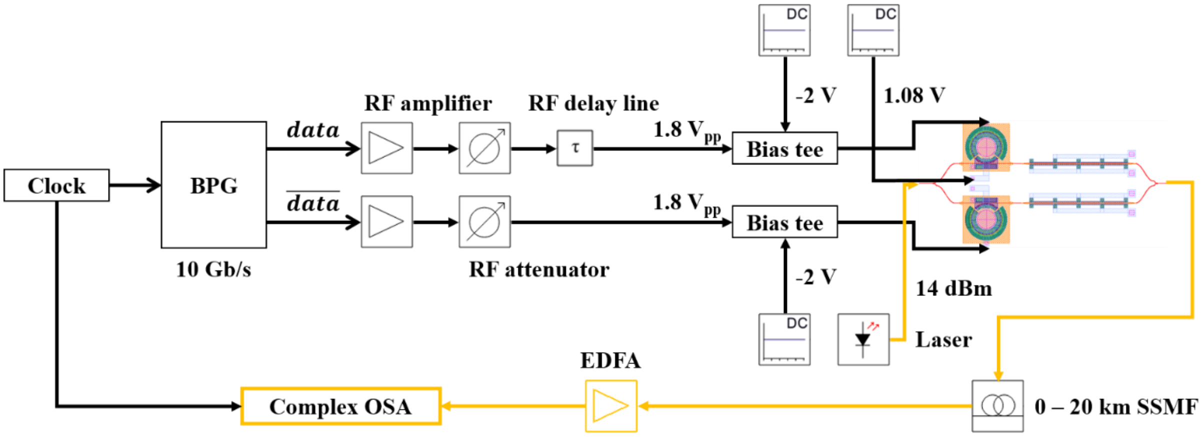

Fig. 3-6. Experimental setup for chirp characterization of the dual parallel MRMs in the push-pull operation. [41]

output was coupled in to the chip and modulated by the device. The modulated optical signals were transmitted over 0 – 20 km of SSMF. Next, they were amplified by an erbium-doped fiber amplifier (EDFA). Finally, the constellation diagrams and the chirp parameters were obtained by the complex OSA.

The parameter defined in Eqs. 3.2 and 3.3 is widely used for evaluating the chirp of a modulator [33, 97, 111, 115, 116], but it is constant only in small-signal regime [114]. In large-signal modulation for optical fiber communications, an effective way to characterize the chirp parameter is still waiting to be discovered. In [116], several definitions of α parameters are studied and compared, but no one can accurately evaluate the chirp of the modulators in large-signal modulation regime. However, the $\alpha_{50\%}$ parameter measured by the APEX AP-2443B complex OSA does not depend on the RF frequency, and thus it can be used to compare the chirp performances of different modulators [117].

The measured constellation diagrams and the $\alpha_{50\%}$ parameters of the dual parallel MRMs operated in a push-pull 10 Gb/s OOK modulation are shown in Fig. 3-7. The previously reported α-parameters of push-pull MZMs [33, 97, 115, 116] have magnitudes between 0.5 and 1.0. Compared to them, the measured chirp parameters of the push-pull dual parallel MRMs from back-to-back (B2B) to 20 km of SSMF transmission are all much smaller. This proves that the device in the push-pull operation is capable of low-chirp modulation. As analyzed in Section 3.3.1, at a higher modulation speed, the measured $\alpha_{50\%}$ parameters will be larger because the phases are not always zero in a wide wavelength range.

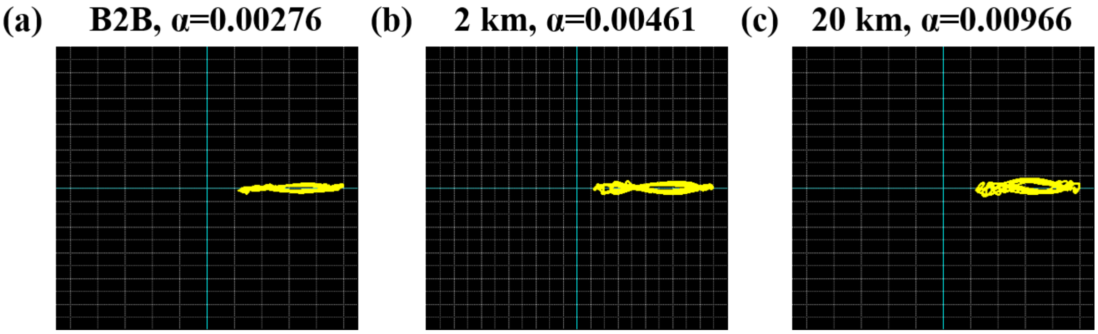

Fig. 3-7. Measured constellation diagrams and $\alpha_{50\%}$ parameters using push-pull 10 Gb/s OOK modulation of the dual parallel MRMs after (b) B2B, (c) 2 km and (d) 20 km of SSMF transmission. (x axis: real part and y axis: imaginary part of the electric field.) [41]

3.4 Device characterization

3.4.1 DC measurement

Figure 3-8 shows the measured DC characterization spectra of the device by applying 0 to 10 V reverse bias voltages on the RF pad of each MRM. The total on-chip IL at a bias voltage of 0 V is approximately 14.0 dB, including the 11.5-dB measured IL from the GC pair and the 1.3-dB estimated IL from the routing waveguide. The device has an IL of 1.2 dB, in which around 0.6 dB comes from the two Y-branches [118] in the MZI. The IL becomes smaller with the applied reverse bias voltages because there is less optical scattering when more carriers are depleted in the rib waveguide, as analyzed in Section 2.2.3.

Though the two MRMs are designed to be identical, their measured resonant wavelengths are different due to the fabrication variations. At -4 V bias, the modulation efficiencies of the two MRMs are both 6.25 pm/V. However, the measured modulation efficiency at -8 V bias becomes 4.375 pm/V, smaller than that at -4 V bias because of the diminishing phase shift effect [19]. When applying higher reverse bias voltages, the ERs become larger. As analyzed in Section 2.3.1, this phenomenon indicates that the MRM is under-coupled. However, this is not the case for the MRMs assisted in the MZI, and it will be analyzed in Section 4.3.1. The FWHM of the two MRMs are both 160 pm at various reverse bias voltages, corresponding to an optical bandwidth of 20 GHz. The Q-factors are measured to be ~ 9.7k for the two MRMs at -4 V bias.

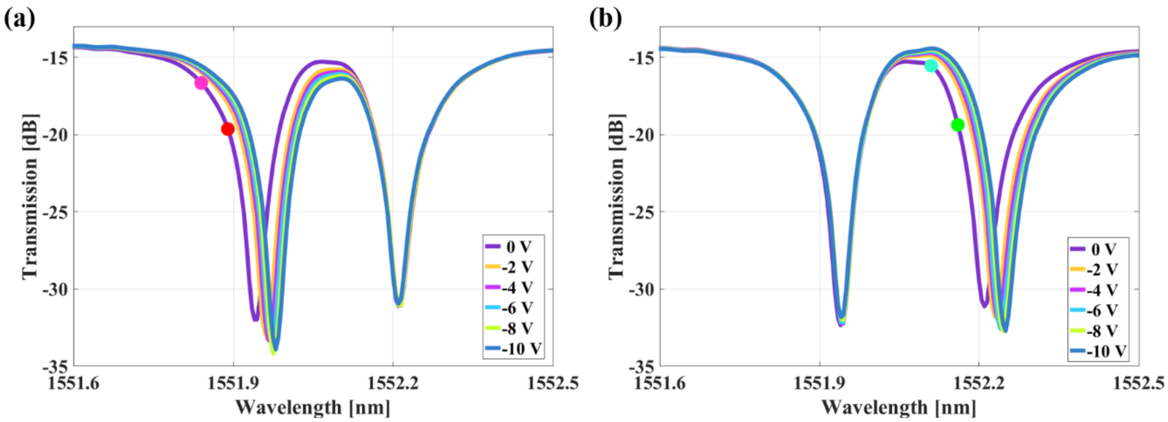

Fig. 3-8. Measured DC characterization spectra when applying 0 – 10 V reverse bias voltages on the RF pad of (a) MRM 1 and (b) MRM 2, respectively. [41]

3.4.2 Small-signal characterization

The measured EE S_{11} responses and EO S_{21} responses are shown in Fig. 3-9. The bias wavelengths are 50 pm and 100 pm away from the resonances of the two MRMs, as marked by the dots in Fig. 3-8. At different detuned wavelengths for each MRM, the EE S_{11} responses are the same, which proves that the detuned wavelength does not influence their electrical responses. However, the measured 3-dB EE bandwidths of the two MRMs are different. It is 29.9 GHz for MRM 1, which is 7.7 GHz smaller than that of MRM 2. This difference is also because of the variations in the fabrication process, such as the misalignment of the pn junction and the implantation concentrations. Therefore, the two MRMs have different junction capacitances and resistances, and this further results in the different measured 3-dB EE bandwidths. As shown in Fig. 3-9(b), the measured EO S_{21} responses are flat at the 50-pm detuning, but those at 100-pm detuned wavelengths away from the resonances have peaking at high frequencies. The reason for this optical peaking effect in the EO responses of the MRMs [85] is analyzed in Section 2.3.1. The measured 3-dB EO bandwidths of MRM 2 are 16.8 GHz and 23.3 GHz at 50 pm detuning and 100 pm detuning, respectively. They are larger than those of MRM 1, which are 15.1 GHz and 21.4 GHz at 50 pm detuning and 100 pm detuning, respectively. Since the two MRMs have the same FWHM, or equivalently, the same optical bandwidth, the difference in their measured 3-dB EO bandwidths is predominantly due to their different 3-dB EE bandwidths.

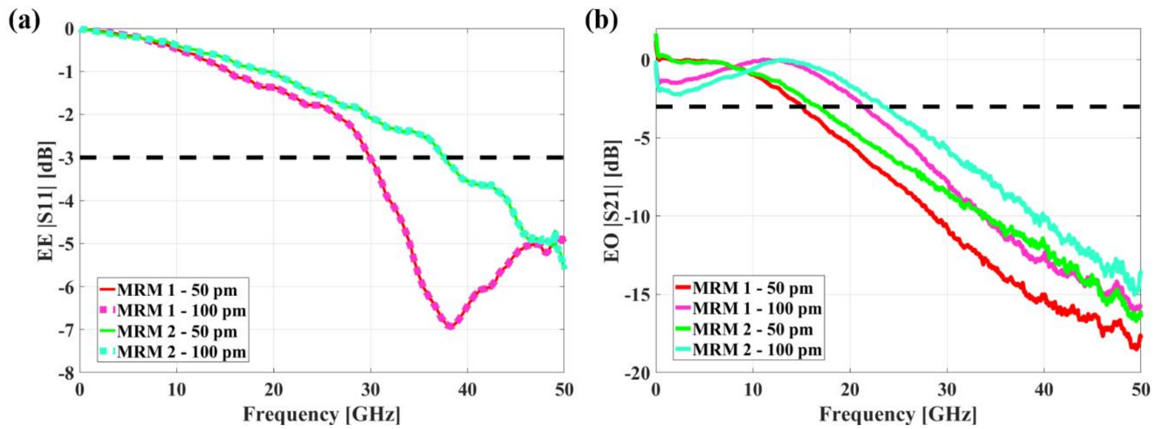

Fig. 3-9. Measured (a) EE S_{11} responses and (b) EO S_{21} responses by applying small RF signals on the two MRMs at 50 pm and 100 pm away from their resonances. [41]

A widely used formula for calculating the 3-dB EO bandwidth of the MRM is [77, 86, 119]:

$$f_{EO} = f_{opt} \bullet f_{EE} / \sqrt{f_{opt}^2 + f_{EE}^2} \tag{3.4}$$

in which f_{EO}, f_{opt} and f_{EE} are the EO bandwidth, optical bandwidth and EE bandwidth of the MRM. However, it is pointed out in [77, 86] that this formula is not accurate because it does not take the influence of wavelength detuning into consideration. For example, using $f_{opt,1}$ = 20 GHz and $f_{opt,2}$ = 20 GHz measured from the DC transmission spectra in Fig. 3-8, $f_{EE,1}$ = 29.9 GHz and $f_{EE,1}$ = 22.2 GHz obtained from the EE S_{11} responses, the calculated EO bandwidths should be $f_{EO,1}$ = 16.6 GHz and $f_{EO,2}$ = 14.8 GHz. These values are close to the measured ones at 50 pm detuned wavelengths, but those measured at 100 pm detuning are much larger since the optical peaking effect broadens the EO bandwidth [85]. In addition, the device proposed in this chapter is not a single MRM, but the dual MRMs parallelly assisted in a balanced MZI. Even though the small RF signals are only applied on one MRM, the DC transmission spectra and EO responses of the proposed device are also influenced by the MZI waveguide and the other MRM.

3.5 Large-signal modulation

The large-signal modulation, including the OOK modulation and PAM-4 transmission, is presented in this section. In the OOK modulation, both the performances of the device and of the single MRM with the same design parameters are shown for comparison. The advantages of the push-pull operation are verified by the measured results. In the PAM-4 transmission, high-speed low-chirp modulation is achieved without any CD compensation method.

3.5.1 OOK modulation

The measurement setup for OOK modulation is shown in Fig. 3-10. The device was tested by applying differential 2^{31}-1 PRBS on the two MRMs. The amplified RF signals have measured peak-to-peak voltage of 1.8 Vpp in a 50 Ω system. The -2 V bias voltages were applied on the two MRMs together with the RF signals by 65 GHz bias tees. The resonances of the two MRMs were aligned by applying 1.08 V on the heater of MRM 1. A 14-dBm laser input was coupled into the device. Afterwards, the modulated optical signals were transmitted over 0 – 20 km of

SSMF. The optical eye diagrams were obtained by a digital communication analyzer (DCA). The optical module in the DCA had a bandwidth of 65 GHz, but a filter for approximately 43 Gb/s was turned on. Then a 35 GHz PD with a trans-impedance amplifier (TIA) was used to convert the optical signals into electrical signals. The received power was kept at 0.7 dBm. Then the BERs were measured by an SHF BER tester.

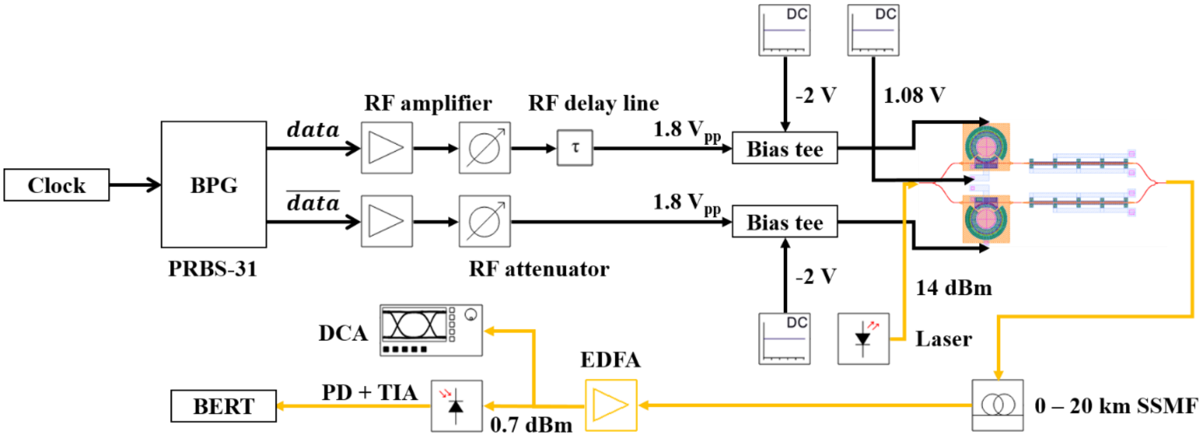

Fig. 3-10. Experimental setup for OOK modulation of the dual parallel MRMs in the push-pull operation.

The single MRM with the same design parameters was also tested by applying 2^{31}-1 PRBS with a 1.8 V_{pp} and -2 V bias, as shown in Fig. 3-11. All the parameters are chosen to be the same to those in Fig. 3-10 for a fair comparison.

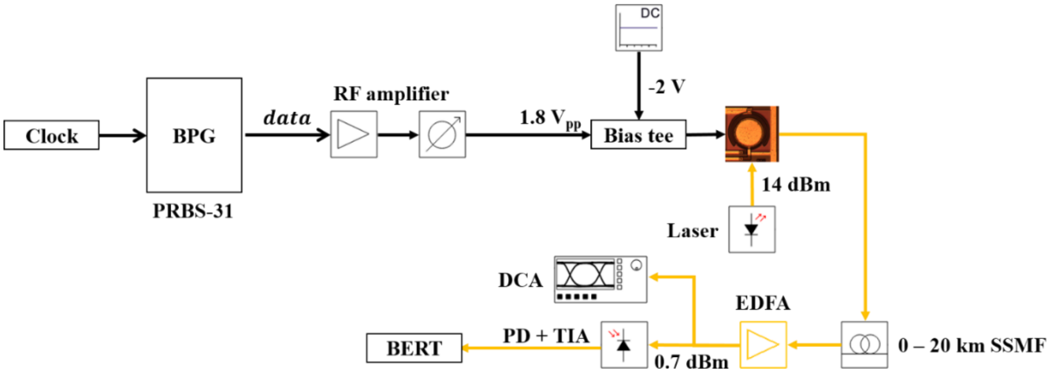

Fig. 3-11. Experimental setup for OOK modulation of the single MRM.

The measured 40 Gb/s optical eye diagrams of the single MRM and the dual parallel MRMs in the push-pull configuration are shown in Fig. 3-12. Compared to the eye diagrams of the single

MRM, more symmetric and clearer open eye diagrams are achieved by the push-pull device. In addition, the measured OMAs are 0.64 mW and 1.80 mW in Figs. 3-12(a) and 3-12(b), respectively. The improvement in the OMA is also an advantage of the push-pull operation, but at a sacrifice of driving the device with two channels of RF signals.

(a) Single MRM, B2B, 40 Gb/s **(b) Push-pull, B2B, 40 Gb/s**

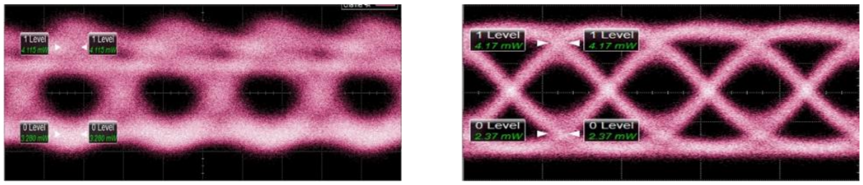

(c) Single MRM, 2 km, 40 Gb/s **(d) Push-pull, 2 km, 40 Gb/s**

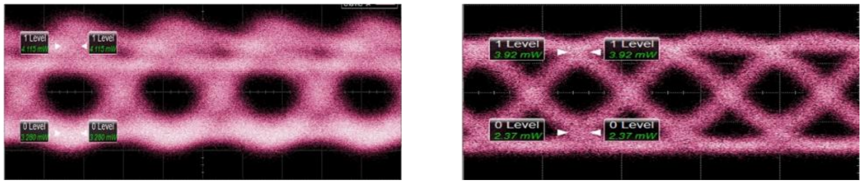

Fig. 3-12. Measured 40 Gb/s optical eye diagrams of the single MRM and the dual parallel MRMs in the push-pull configuration. [42]

Figures 3-13(a) and 3-13(b) show the measured BERs of the single MRM and the push-pull dual parallel MRMs, respectively. Both the HD FEC threshold of 3.8×10^{-3} [120] and KP4 FEC threshold of 2.2×10^{-4} [121] are listed for evaluation. In the B2B transmission, the dual parallel MRMs operated in a push-pull configuration have error free operation (0 errors in 3 Tbits transmission) up to 40 Gb/s, and it is 8 Gb/s better than that of the single MRM. The BER of the push-pull device is still below the HD FEC threshold at 60 Gb/s. As shown in Fig. 3-13(a), transmission up to 5 km of SSMF using the single MRM is successfully demonstrated. However, the BERs over 10 km and 20 km of SSMF transmission are hard to obtain. As shown in Fig. 3-13(b), the dual parallel MRMs driven by push-pull RF signals can transmit optical signals over 20 km of SSMF without using any CD compensation method. The 20 Gb/s optical eye diagram after transmission over 20 km of SSMF is inserted in Fig. 3-13(b). If considering the KP4 FEC threshold, which is a BER limit typically used in short-reach transmission systems and a standard in the next generation 400G Ethernet [16], the push-pull operation of the dual parallel MRMs can achieve 56 Gb/s in the B2B configuration, 50 Gb/s transmission up to 2 km, 30 Gb/s transmission of 10 km and 23 Gb/s transmission of 20 km.

There are two reasons for the better transmission performance using the dual parallel MRMs and the push-pull operation. One is the low-chirp modulation, as analyzed in Section 3.3, which enables the modulated optical signals to transmit for a longer distance. The other is the larger OMA, as shown by the optical eye diagrams in Figs. 3-12(b) and 3-12(d), which helps the device to achieve a better BER performance.

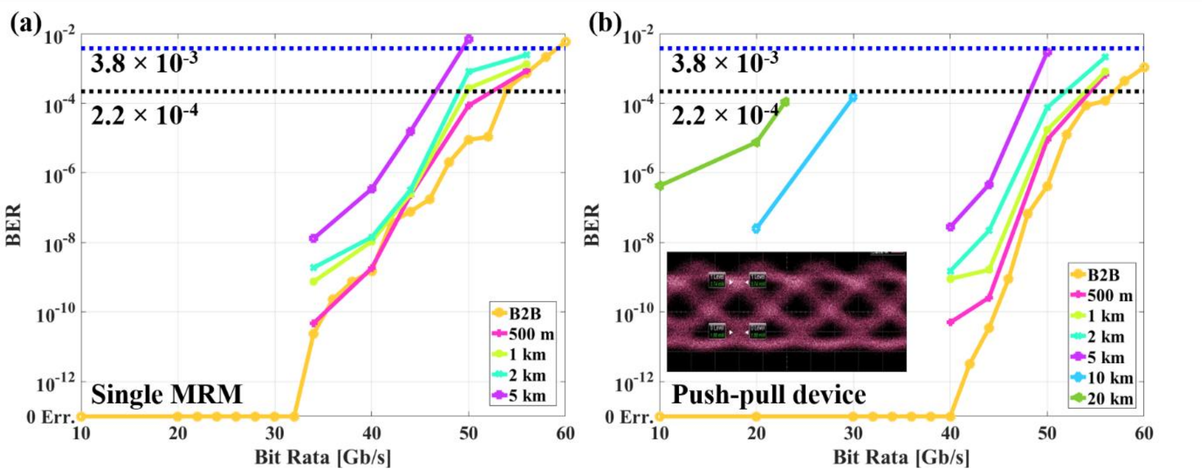

Fig. 3-13. Measured BERs of (a) the single MRM and (b) the push-pull dual-parallel (inserted: 20 Gb/s optical eye diagram after 20 km of SSMF transmission). [42]

3.5.2 PAM-4

The experimental setup of PAM-4 transmission by operating the dual parallel MRMs in the push-pull configuration is illustrated in Fig. 3-14. With the offline DSP, an 8-bit DAC generated the differential 4-level RF data at 70 GSamples/s. The peak-to-peak voltages of the RF data after amplification and synchronization were measured to be 1.6 Vpp in a 50 Ω system. The differential RF data and −3 V bias voltages were applied on the two MRMs using the 65 GHz bias tees. A 1.08 V DC voltage was used to tune the resonance wavelength of MRM 1 closer to that of MRM 2, and achieve the condition for push-pull operation, as illustrated by the simulated transmission spectra in Fig. 3-4(a). The laser input at 14 dBm was coupled into the device and the modulated PAM-4 optical signals were transmitted over 0 – 20 km of SSMF. Then we used an EDFA to amplify the signals, and a DCA with an optical filter turned to obtain the optical eye diagrams. To measure the BERs, first a 35 GHz PD with a TIA received the signals at a fixed average power of 0.7 dBm, and then a 62 GHz 8-bit real-time oscilloscope (RTO) working at 160 GSamples/s was used to capture the received data for offline DSP.

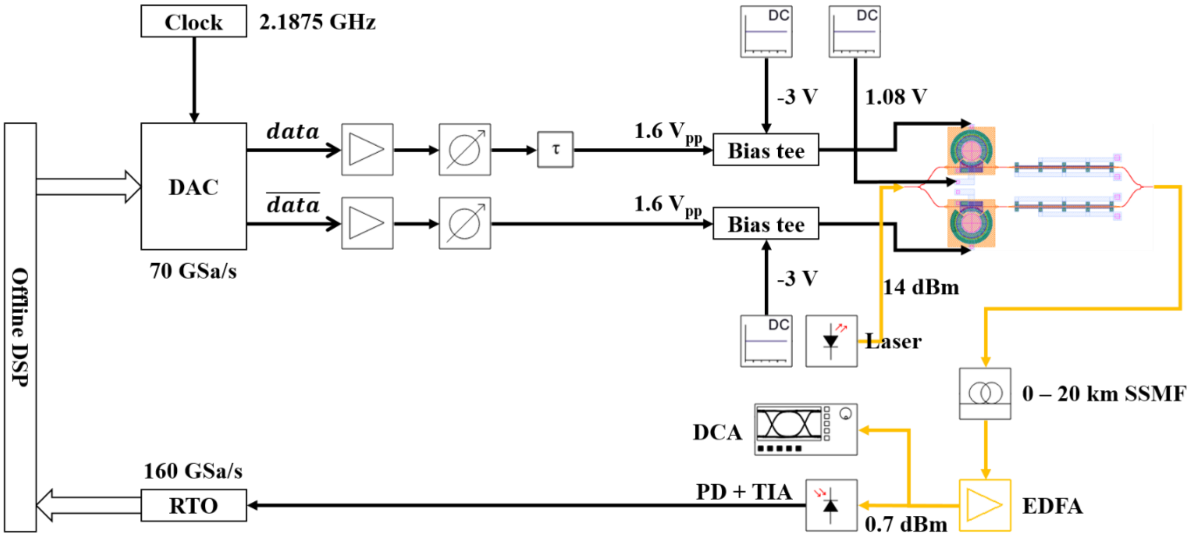

Fig. 3-14. Experimental setup of the PAM-4 transmission using the push-pull operation of the dual parallel MRMs. [41]

The sequential steps of the offline DSP are depicted in Fig. 3-15. On the transmitter side, first a pseudo random integer sequence (PRIS) was generated. The length of the PRIS depended on the selected baud rate. It was 33001 at 28 Gbaud and 65001 at 50 Gbaud. Then for pulse shaping, a root-raised cosine (RRC) filter with a roll-off factor α of 0.5 was applied. As the sampling rate of the DAC is 70 GSamples/s, the sequence was resampled by inserting (70/B – 1) zeros, where B is the baudrate in Gbaud. A pre-emphasis filter, which was obtained by a least-mean-squares algorithm using a training sequence [122], was applied afterwards. This filter was used to compensate only the limitations of the DAC and the RF components, not that of the modulator. Then the DAC generated the differential RF data based on the digital sequence. On the receiver side, first the data captured by the RTO were resampled to 2 samples/symbol. Then a RRC filter with α = 0.5 matched to the filter on the transmitter side was applied. To compensate for the remaining frequency response degradation, an equalizer, whose coefficients were also obtained from a training sequence, was used. Finally, by comparing the processed data to the transmitted PRIS after synchronization data, the BERs were obtained and the eye diagrams were plot.

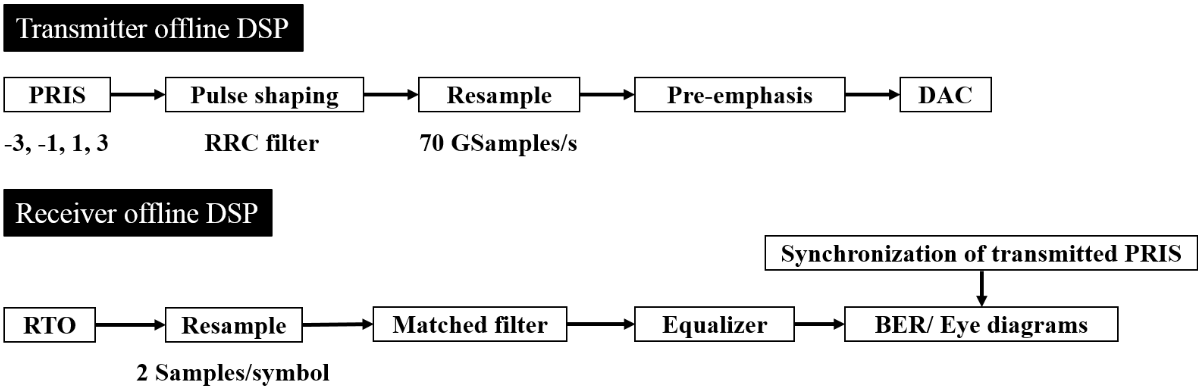

Fig. 3-15. Offline DSP for the PAM-4 transmission. [41]

The optical eye diagrams shown in Fig. 3-16 are after B2B transmission and then obtained by the DCA without applying the offline DSP on the receiver side. Since the clock input in the DCA should be integer times of the 2.8175 GHz clock frequency into the DAC, the optical eye diagrams are all at 21.875 Gbaud. They are the PAM-4 eye diagrams by driving the dual parallel MRMs with the differential RF signals, by driving MRM 1 with the RF signals and by driving MRM 2 with the inverted RF signals, respectively. In Figs. 3-16(b) and 3-16(c), the PAM-4 levels are not equally spaced because the nonlinearity of the MRMs is not compensated by the offline DSP. But as shown in Fig. 3-16(a), the push-pull operation results in clearer and more symmetric eye diagrams.

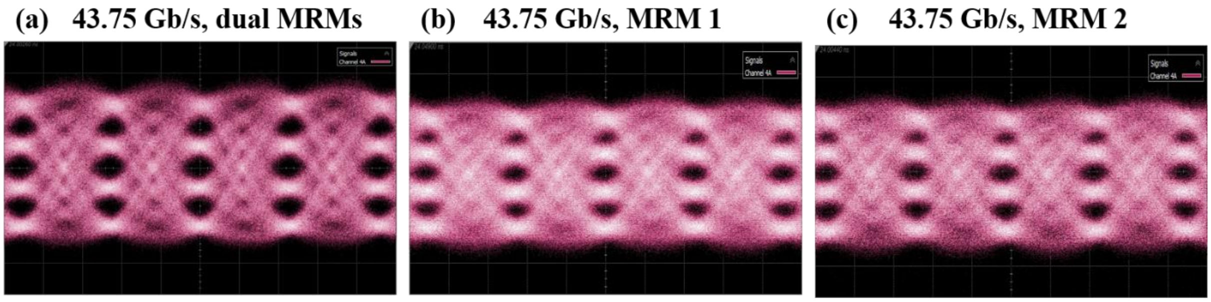
(a) 43.75 Gb/s, dual MRMs **(b) 43.75 Gb/s, MRM 1** **(c) 43.75 Gb/s, MRM 2**

Fig. 3-16. 43.75 Gb/s PAM-4 optical eye diagrams in B2B configuration obtained by (a) driving the dual parallel MRMs with the differential RF signals [41], (b) driving MRM 1 with the RF signals and (c) driving MRM 2 with the inverted RF signals.

The eye diagrams obtained using the offline DSP on the receiver side are shown in Fig. 3-17. At 80 Gb/s after transmission over 1 km and 2 km of SSMF, at 56 Gb/s after transmission over

10 km of SSMF, and at 34 Gb/s after transmission over 20 km of SSMF, the eye diagrams are all clearly open with the BERs below the HD FEC threshold. As shown in Fig. 3-17(a), the BER of 80 Gb/s 1 km transmission is below the KP4 FEC threshold. The 34 Gb/s eye diagram after 20 km of SSMF transmission has zero error detected using the transmission sequence. Similarly, the unequal eye openings are because nonlinearity of the modulator is not compensated in the offline DSP on both transmitter and receiver sides.

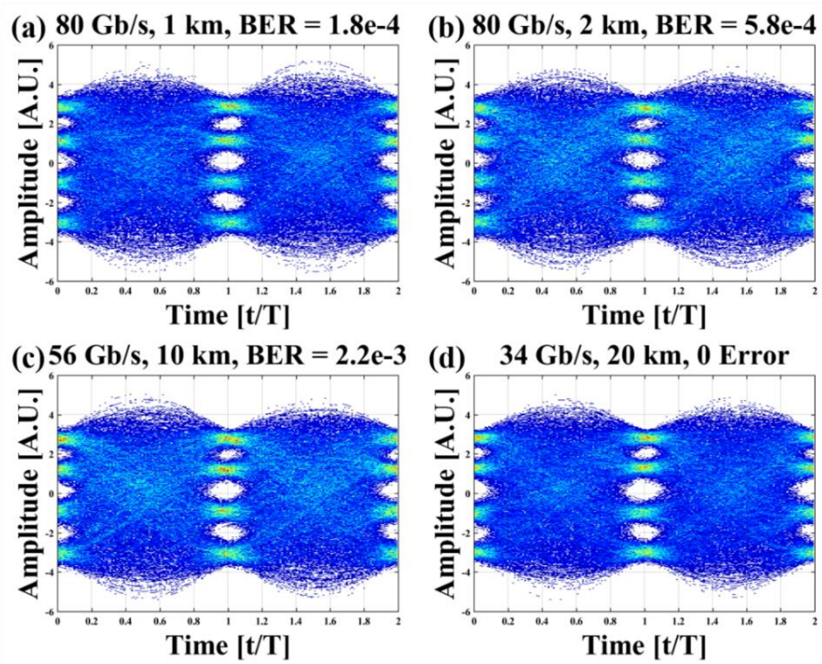

Fig. 3-17. PAM-4 optical eye diagrams obtained by offline DSP at (a) 80 Gb/s after 1 km of SSMF transmission, (b) 80 Gb/s after 2 km of SSMF transmission, (c) at 56 Gb/s after 10 km of SSMF transmission and (d) at 34 Gb/s after 20 km of SSMF transmission. [41]

Figure 3-18 shows the measured BER results of the push-pull PAM-4 transmission. In addition to the HD FEC threshold of 3.8×10^{-3} and the KP4 FEC threshold of 2.2×10^{-4}, the soft-decision (SD) FEC threshold of 2×10^{-2} is also listed for performance evaluation. The ‘0 Err.’ in the figure means that there is no error detected using the transmitted PRIS. Even after 1 km of SSMF transmission, the push-pull operation of the dual parallel MRMs can achieve no error at 70 Gb/s, and the BER at 92 Gb/s is below the HD FEC threshold. If considering the SD FEC threshold, the device works at 100 Gb/s. For 2 km of SSMF transmission, at the three different FEC thresholds it works at 76 Gb/s, 84 Gb/s and 96 Gb/s, respectively. Even though the push-pull operation has the advantage of low-chirp modulation, the quality of signals still degrades when transmitting for a longer fiber distance. For 5 km and 10 km of SSMF transmission, the bit rates for the BERs below the HD FEC threshold are 64 Gb/s and 56 Gb/s, respectively. In addition, PAM-4 transmission at 40 Gb/s over 20 km of SSMF with BER lower than 3.8×10^{-3} is also successfully demonstrated.

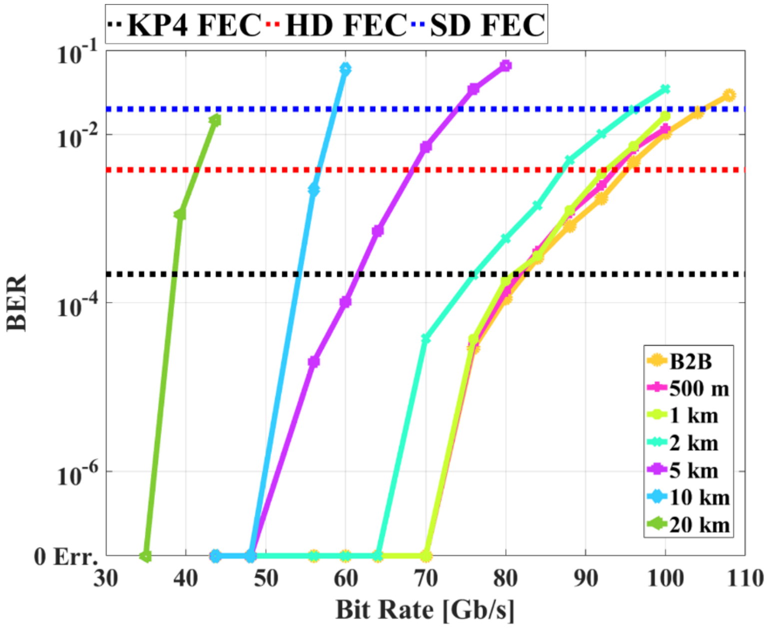

Fig. 3-18. The measured BERs of PAM-4 transmission using the push-pull dual parallel MRMs at various bit rates over 0 – 20 km of SSMF. [41]

3.6 Conclusion

In this chapter, we design and experimentally demonstrate the push-pull operation of dual parallel MRMs for high-speed low-chirp PAM-4 transmission. The operating principle is elaborated using a system level simulation. Then its main advantage, which is the low-chirp modulation, is verified by the measured constellation eye diagrams and chirp parameters using 10 Gb/s OOK transmission up to 20 km of SSMF [41]. The device has a modulation efficiency of 6.25 pm/V at -4 V bias. The measured 3-dB EO bandwidths dependents on the detuned wavelengths, and at 100 pm detuning they are 23.3 GHz and 21.4 GHz when applying small RF signals on the two MRMs, respectively [41].

In the B2B OOK modulation, the device has error free performance at 40 Gb/s, and the BER at 60 Gb/s is measured to be below the HD FEC threshold [42]. Without any method for CD compensation, the modulated 23 Gb/s OOK optical signals are transmitted successfully over SSMF up to 20 km with BERs below the HD FEC threshold of 3.8×10^{-3} [42]. Compared to the single MRM with the same PN junction design and geometric parameters, the dual parallel MRMs in the push-pull configuration has better OOK modulation and transmission performance.

In the PAM-4 transmission, successful 92 Gb/s over 1 km of SSMF and 40 Gb/s over 20 km of SSMF are demonstrated, with measured BERs below the HD FEC threshold of 3.8×10^{-3} [41]. If considering the SD FEC threshold, 100 Gb/s PAM-4 transmission over 1 km of SSMF is achieved. Compared to the previously published SiP MRM-based PAM-4 results [18, 90, 91], the work presented in this chapter shows the highest bit rate. It proves that the push-pull operation of the dual parallel MRMs is a good candidate for the next generation intra-data center optical transmission links.

Chapter 4

Resonances overlap operation of an MRM with an MRR

4.1 Overview

As introduced in Section 1.2 and compared in Table 1, the two widely used SiP modulator structures, TWMZMs and MRMs, have both pros and cons. TWMZM has the advantages of high fabrication tolerance and thermal stability, but it is typically a few millimeters in length and thus it occupies a large area of footprint. MRM is compact and its natural filtering ability is desirable for the applications in WDM systems, but it has the disadvantages of thermal instability and fabrication sensitivity. Therefore, SiP modulators based on the combination of MZIs and MRRs are reported for different purposes [25-31], as summarized in Table 5. However, 50 G class PAM-4 transmission over short reach distances, which are suitable for the next generation intra-data center applications, have not been reported based on these modulator structures.

In this chapter, we analyze and experimentally demonstrate an operating principle of resonances overlap for PAM-4 transmission based on a SiP modulator structure of assisting an MRM and an MRR in a balanced MZI. This chapter is based on the author's work in [43-45], and the operation is elaborated in two steps. First, the advantages of assisting a single MRM in a balanced MZI are analyzed, by comparing it to a single MRM with the same design parameters. Second, the device is designed by assisting the balanced MZI with an MRM on one arm and an MRR on the other arm, and the analysis on the performance enhancement using the resonances overlap operation is further presented.

This chapter is organized as follows. In Section 4.2, the device structure design and fabrication are demonstrated. Then the operating principle is explained in Section 4.3, with the single MRM-assisted MZI introduced in Section 4.3.1, and the resonances overlap of an MRM with an MRR elaborated in Section 4.3.2. In these two sections, the measured DC transmission spectra and the related analysis are also shown to further explain the advantages of this operating principle. In Section 4.4, the large-signal modulation, including the OOK modulation in Section 4.4.1 and the PAM-4 results in Section 4.4.2, are presented. In Section 4.5, other resonances overlap operating principles are also analyzed. Finally, this chapter is concluded in Section 4.6.

4.2 Device design and fabrication

The schematic layouts of the devices demonstrating the resonances overlap operation are illustrated in Fig. 4-1. The MRMs in these three structures all have the same geometry parameters, PN junction design and heater design to those shown in Figs. 3-1 and 3-2 of Section 3.2. The single MRM in Fig. 4-1(a) is designed for a purpose of comparison with other devices, the structure in Fig. 4-2(b) is designed for analyzing the performance improvement by assisting a single MRM in a balanced MZI, and the device in Fig. 4-1(c) is to achieve resonances overlap operation of an MRM with a passive MRR for further enhancing its performance. The RF signals

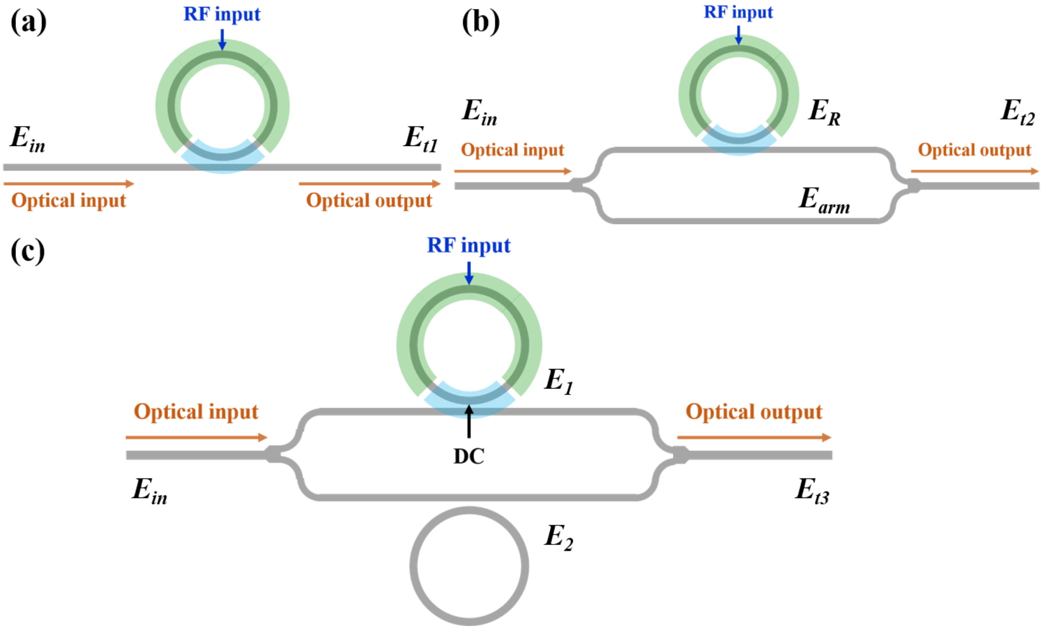

Fig. 4-1. Schematic layouts of (a) a single MRM, (b) a single MRM-assisted MZI, and (c) a balanced MZI assisted by an MRM and an MRR to achieve resonances overlap.

are all applied on the PN junction of the MRM in these three structures. An extra DC voltage is applied on the MRM heater of the device shown in Fig. 4-1(c) to align the resonances.

Figures 4-2(a) and 4-2(b) show the design layouts of the single MRM and the dual MRMs-assisted MZI. Obviously, the operation of Fig. 4-1(a) is achieved by applying RF signals on the single MRM shown in Fig. 4-2(a). Figures 4-1(b) and 4-1(c) are realized by operating the design in Fig. 4-2(b) in two different ways. By applying a DC voltage on MRM 2, its resonance shifts to a longer wavelength, and thus the resonances of the two MRMs are clearly separated. In this case, if applying RF signals on MRM 1 and only focusing on the wavelength range around its resonance, the device works as the structure shown in Fig. 4-1(b). In this case, MRM 2 are not modulated and it works as a passive MRR. Since these two MRMs are designed to be identical, their resonant wavelengths should be the same. However, there are always deviations between what are fabricated from what are designed. For example, ring radius, gap and the PN doping concentrations may variate in the fabrication process. As a result, the effective index of the waveguide, the straight-through coupling coefficient and the round-trip attenuation coefficient are different from the designed values, then the transmission spectrum of the device changes accordingly. In the measurement, the transmission spectrum of the device in Fig. 4-2(b) always has two resonant wavelengths in one FSR, which are the resonances of the two MRMs respectively. Therefore, a DC voltage is applied on one of the MRMs to overlap their resonances till the measured transmission spectrum of the whole device has the largest static ER. Then, RF signals are applied on MRM 1 to achieve the operation of Fig. 4-1(c). Similarly, MRM 2 also works as a passive MRR without being modulated. The heaters on the MZI arms are used for

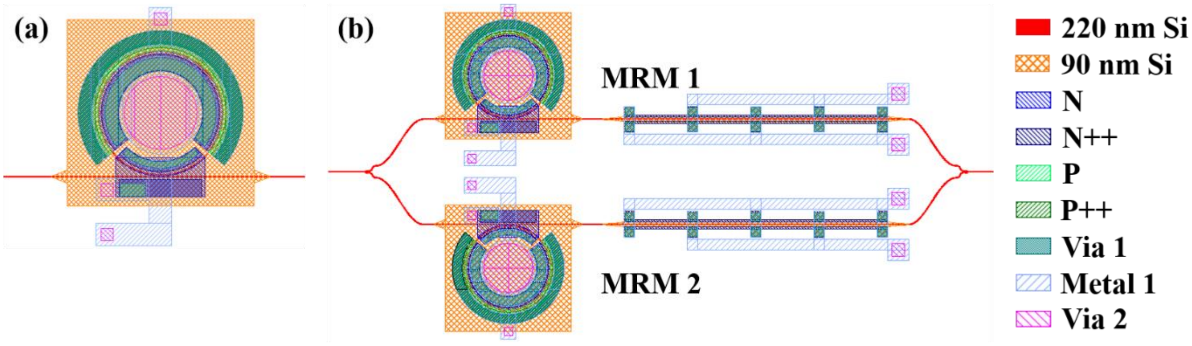

Fig. 4-2. Design layouts of (a) the single MRM and (b) the dual MRMs-assisted MZI.

compensating any imbalance induced by the fabrication variations. The operating methods will be further elaborated in Section 4.3.

These two devices were fabricated at IME A*STAR based on the same process described in Section 3.2. The micrographs are those shown in Fig. 3-3.

4.3 Operating principle

The purpose of overlapping the resonances of the MRM with that of a passive MRR is to achieve larger ERs and OMAs, which are desirable for PAM-4 transmission with better performances. In this section, the operating principle is analyzed in two steps. First, compared to that of a single MRM, the performance of the single MRM-assisted MZI is largely improved. Second, by assisting the MZI with an MRM on one arm and an MRR on the other arm, the ERs and OMAs are further enhanced. The advantages of this operating principle are also proved by the measured transmission spectra and the related analysis on the ERs and OMAs.

4.3.1 Single MRM-assisted MZI

The transfer function of an all-pass MRR is introduced by Eqs. 2.8 and 2.9 in Section 2.3.1. Here, they are presented again for convenience. As shown in Fig. 4-1(a), with an input electric field E_{in}, the output electric field E_{t1} of the single MRM is [82]:

$$E_{t1} = E_{in} \frac{-\Lambda + \sigma e^{-j\phi}}{-\Lambda\sigma + e^{-j\phi}} \tag{4.1}$$

where Λ is the round-trip attenuation, σ is the straight-through coupling coefficient, and ϕ is the round-trip phase change defined as [83]:

$$\phi = 4\pi^2 \mathrm{n}_{eff} \frac{R}{\lambda} \tag{4.2}$$

in which n_{eff} is the effective index of the MRM waveguide, R is the radius and λ is the wavelength.

For the structure shown in Fig. 4-1(b), the output electric field E_{t2} is:

$$E_{t2} = \frac{1}{\sqrt{2}}\Lambda_m E_R + \frac{1}{\sqrt{2}}\Lambda_m E_{arm} e^{-j\varphi} = \frac{1}{2}\Lambda_m E_{in}\left(\frac{-\Lambda + te^{-j\theta}}{-\Lambda t^* + e^{-j\theta}} + e^{-j\varphi}\right) \tag{4.3}$$

where Λ_m is the propagation attenuation of the MZI arm, E_R and E_{arm} are the electric fields on the two MZI arms as shown in Fig. 4-1(b), and φ is the phase difference between the two MZI arms induced by the fabrication variations.

In the simulation, we use R = 20 μm as designed. Based on the designed geometry parameters and PN junction design, the round-trip attenuation Λ and the straight-through coupling coefficient σ are simulated using Lumerical FDTD Solutions [74], and the effective index n_{eff} is simulated using Lumerical MODE Solutions [70]. They are and they are Λ = 0.9847, σ = 0.8661, and n_{eff} = 2.5673. The electric field propagation attenuation of the MZI waveguide Λ_m is calculated based on a typically used propagation loss value of 2.4 dB/cm in the silicon waveguide. Since the length of the MZI arm is 230 μm, Λ_m = 0.9937. We assume there is no fabrication variation, so the phase difference φ in the simulation is set as φ = 0.

Figures 4-3(a) and 4-3(b) show the simulated power transmission and phase response of the single MRM, respectively. Because Λ = 0.9847 and σ = 0.8661, the MRM far away from the critical coupling condition (Λ = σ) [82]. Therefore, its static ER of the single MRM is very small, which is less than 2 dB, as shown in Fig. 4-3(a). The simulated 2π phase change across its resonance shown in Fig. 4-3(b) also confirms that the single MRM is in the over-coupled condition (Λ > σ). If using this MRM for PAM-4, the ER between the '11' level and the '00' level cannot be larger than the static ER, which is only approximately 1.9 dB. The ERs between the adjacent levels (e.g. '10' and '01' levels) are even smaller than this. This makes the

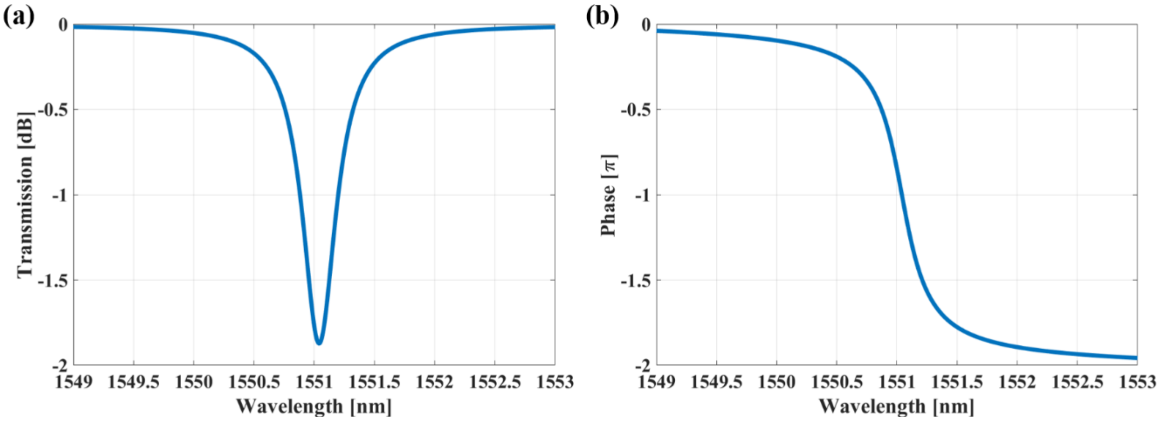

Fig. 4-3. Simulated (a) power transmission and (b) phase response of the single MRM. [43]

(©2017 IEEE)

modulated four power levels hard to be detected, especially in the presence of noise. As a result, this single MRM achieves poor PAM-4 performance.

Based on $\Lambda_m = 0.9937$, $\varphi = 0$, and the other simulation parameters same to those of the single MRM, the simulated power transmission and phase response of the single MRM-assisted MZI are shown in Figs. 4-4(a) and 4-4(b), respectively. The static ER of the device is approximately 20 dB, which is more than 18 dB larger than that of the single MRM. This is because of the small imbalance between the two MZI arms, and the phase change across the resonance of the MRM. At the output coupler of the interferometer, the response of the MRM and the electric field on the other arm have constructive (0 phase difference between the two arms), destructive (π phase difference) and constructive (2π phase change) interferences across the resonant wavelength. It is the destructive interference at the resonance that leads to a large static ER. This is good for PAM-4 because the adjacent levels will have sufficient spacings for detection, even though there are noise in the transmission links. In addition, if the MRM has a smaller static ER, which means it has a larger electric field amplitude with a phase of π at the resonance, the single MRM-assisted MZI will have a larger static ER because of the more destructive interference at the resonant wavelength. As shown in Fig. 4-4(b), the simulated phase response is approximately 0.6π across the resonance. It is much smaller than that of the single MRM and leads to a smaller chirp.

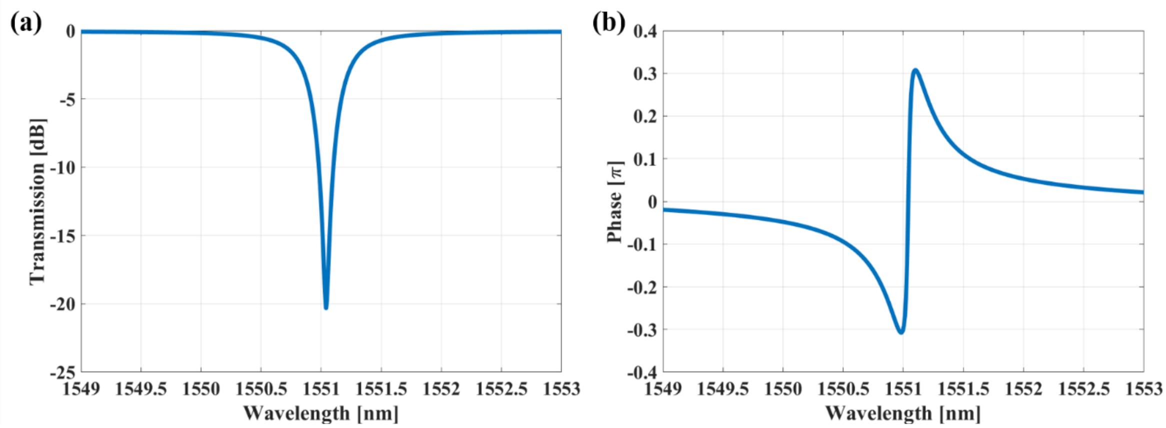

Fig. 4-4. Simulated (a) power transmission and (b) phase response of the single MRM-assisted MZI. [43] (©2017 IEEE)

Figures 4-5(a) and 4-5(b) present the measured transmission spectra of the two devices under 0 to 8 V reverse bias voltages. It should be noted that Fig. 4-5(b) is measured using the device shown in Fig. 4-2(b) by applying a DC voltage on MRM 2 to shift its resonant wavelength far away from that of the MRM 1. In this case, the bias voltages are applied on the PN junction of MRM 1, while the other arm works as a waveguide. The two devices have total on-chip ILs of 10.6 dB and 12.5 dB, respectively. The measured IL of the GC pair is 9 dB. This is different to the value reported in Section 3.4.1 because there are fabrication variations from chip to chip. In addition, the angles of the fiber array for coupling light in and out are not exactly the same in different experiments. The routing waveguides also have ILs, which are 0.8 dB for the single MRM and 1.3 dB for the single MRM-assisted MZI. Therefore, the two devices have the ILs of 0.8 dB and 2.2 dB, respectively. The two Y-branches [118] and the MZI arms both contribute to the larger IL of the single MRM-assisted MZI.

The measured static ER of the single MRM at 0 V bias is approximately 1.5 dB, as shown in Fig. 4-5(a). It is smaller than the simulated value, mainly due to the fabrication deviations. When applying larger reverse bias voltages, its static ERs become smaller, which is a signature of an over-coupled MRM [77]. As shown in Fig. 4-5(b), the static ER of the single MRM-assisted MZI is measured to be approximately 20 dB at 0 V bias, and it increases with the applied reverse bias voltages. This is consistent with our analysis on the simulation results: if the MRM has a smaller static ER, the single MRM-assisted MZI will have a larger static ER because of the more destructive interference at the resonant wavelength. Because of the identical PN junctions in these two devices, the modulation efficiencies are both measured to be 6.25 pm/V at -8 V bias.

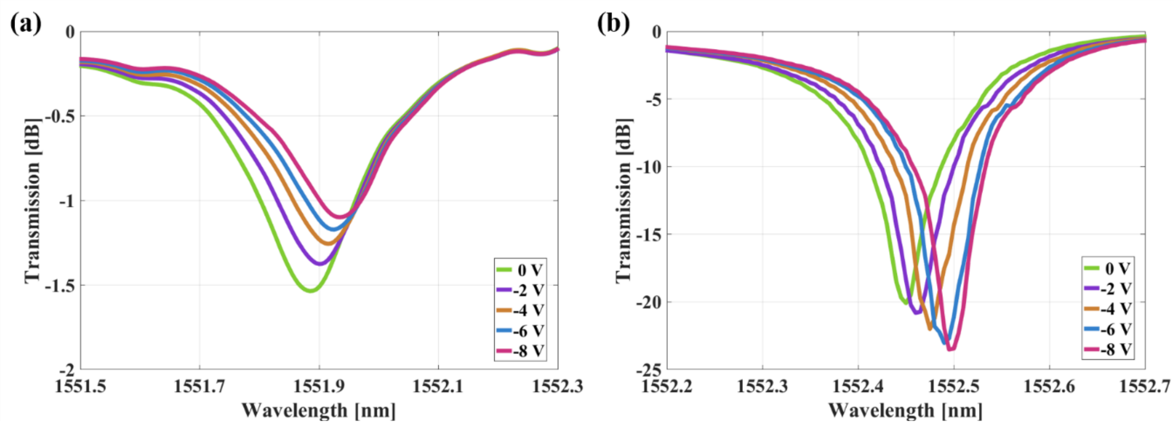

Fig. 4-5. Measured DC transmission spectra of (a) the single MRM and (b) the single MRM-assisted MZI. [43] (©2017 IEEE)

In conclusion, by assisting a single MRM on one arm of a balanced MZI, the static ER of the device is much larger than that of the single MRM, which is desirable for PAM-4 with adjacent levels clearly distinguished.

4.3.2 Resonances overlap of an MRM with an MRR

When an electric field E_{in} is input into the structure shown in Fig. 4-1(c), the transmitted electric fields on the two MZI arms after the microrings are [82]:

$$E_1 = \frac{E_{in}}{\sqrt{2}} \frac{-\Lambda_1 + \sigma_1 e^{-j\phi_1}}{-\Lambda_1\sigma_1 + e^{-j\phi_1}} \tag{4.4}$$

$$E_2 = \frac{E_{in}}{\sqrt{2}} \frac{-\Lambda_2 + \sigma_2 e^{-j\phi_2}}{-\Lambda_2\sigma_2 + e^{-j\phi_2}} \tag{4.5}$$

where Λ_1, Λ_2 are the round-trip attenuations of the two microrings, σ_1, σ_2 are their straight-through coupling coefficients, and ϕ_1, ϕ_2 are the round-trip phase changes which are expressed using the following equations [83]:

$$\phi_1 = 4\pi^2 \mathrm{n}_{\mathrm{eff1}} \frac{R_1}{\lambda} \tag{4.6}$$

$$\phi_2 = 4\pi^2 \mathrm{n}_{\mathrm{eff2}} \frac{R_2}{\lambda} \tag{4.7}$$

in which n_{eff1}, n_{eff2} are the effective indices of the two microring waveguides, R_1, R_2 are the ring radii, and λ is the wavelength.

The output electric field of the device is:

$$E_{t3} = \frac{1}{\sqrt{2}} \Lambda_m (E_1 + E_2) \tag{4.8}$$

where Λ_m is defined as the electric field propagation loss of the MZI waveguide.

The analysis methodology in this section is different from that in Section 4.3.1. This is because the structure in Fig. 4-1(c) is much more complicated than those shown in Figs. 4-1(a) and 4-1(b). Due to variations in the fabrication process, the device may have more parameters different from the designed values. To be specific, in this case, Λ_1, Λ_2, σ_1, σ_2, n_{eff1}, n_{eff2} and even R_1, R_2 may all be different from what are designed. Therefore, we first obtain the measured transmission spectrum of the device, and then based on Eqs. 4.6, 4.7 and 4.8, the parameters are extracted by curve fitting. Afterwards, the DC transmission spectra are simulated using these parameters. Finally, the measured DC characterization is used for analysis in detail. The device also works as a single MRM-assisted MZI by applying a DC voltage on MRM 2 to clearly separate the two resonances. The same analysis methodology is also implemented on this structure to compare the performances of the device when the resonances are overlapped and separated.

Figure 4-6(a) shows the experimental setup for measuring the passive transmission spectra of the device in different conditions. DC 1 and DC 2 are the voltages applied on the heaters of the MRM and the MRR, respectively. The measured transmission spectra after normalization to the ILs of the GC pair and routing waveguide are shown in Fig. 4-6(b). The passive curve is obtained without applying any DC voltage on any heater. Two resonances are observed since there are fabrication variations. The red curve is the transmission spectrum when applying a 2-V voltage on the MRM heater. In this case, the resonance of the MRM shifts to a longer wavelength and it overlaps with that of the MRR. For comparison, a 1.13-V voltage is applied on the heater of the MRR to make the two resonances clearly separated, as shown by the green curve.

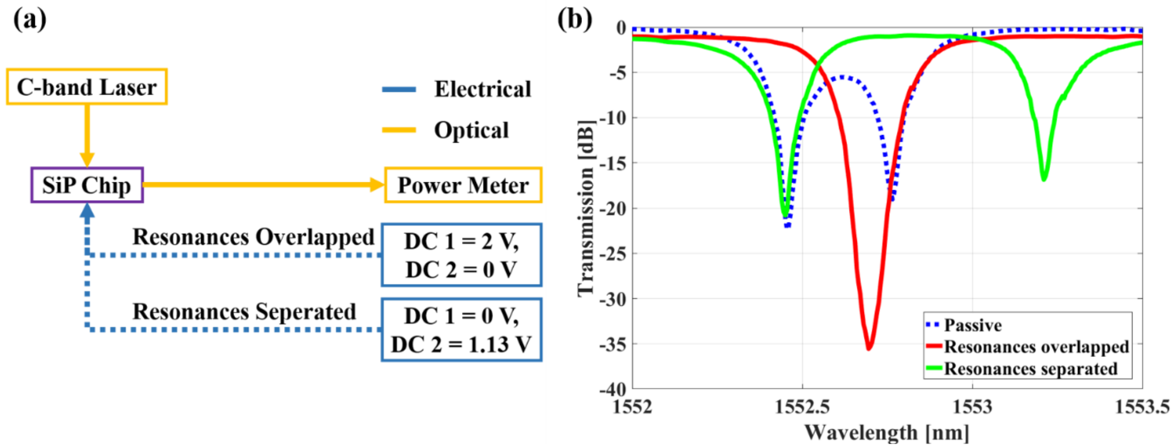

Fig. 4-6. (a) Experimental setup and (b) measured transmission spectra of the device in different conditions. [45] (©2017 IEEE)

Table 7 lists the FOMs of the device in the resonances separated and overlapped conditions. When the resonances are overlapped, the FWHM is 105 pm wider and the static ER is 15 dB larger than those when the resonances are separated.

Table 7. FOMs of the device. [45] (©2017 IEEE)

	Q-factor	FWHM (pm)	ER (dB)
Resonances separated	7,220	215	19.5
Resonances overlapped	4,850	320	34.5

The parameters of the device are obtained in two steps. First, based on the designs, the radii R_1 and R_2 are set to be 20 μm, the round-trip attenuation coefficients Λ_1 and Λ_2 are calculated to be 0.99, corresponding to a 7 dB/cm MRR waveguide loss. Λ_m is set based on a 2.4 dB/cm propagation loss of the 230-μm MZI waveguide, and it is 0.9937. Second, the remaining parameters of the resonances overlapped and separated conditions are extracted by curve fitting of the red curve and green curve in Fig. 4-6(b), respectively, and they are listed in Table 8. As shown in Fig. 4-2(b), the N doped heaters are designed on the coupling region between the microrings and the MZI arms. As a result, when applying a DC voltage on the heaters, both the effective indices and the straight-through coupling coefficients will be changed.

Table 8. Extracted parameters of the device in resonances separated and overlapped conditions by curve fitting.

	n_{eff1}	n_{eff2}	σ_1	σ_2
Resonances separated	2.520198	2.521469	0.88	0.945
Resonances overlapped	2.520456	2.520769	0.904	0.94

Using the fitted parameters and a modulation efficiency of $dn_{eff}/dV = 1.5 \times 10^{-5}$ /V, the simulated DC characterization spectra of the device in the two conditions are shown in Fig. 4-7. In the simulation, various reverse bias voltages from 0 to 8 V are applied on the PN junction of the MRM, while the MRR works as a passive resonator. When the resonances are overlapped, the OMA and the ER at the operating wavelength λ_2 under -4 V bias are 81 μW and 13.2 dB, respectively. For the resonances separated condition, we choose the bias wavelength of λ_1 because the power transmission is similar to that at λ_2 in the resonances overlapped condition, and the OMA and ER at -4 V are 75 μW and 9.4 dB, respectively. The simulated results show that the OMA and the ER are both improved by overlapping the resonances of the two microrings.

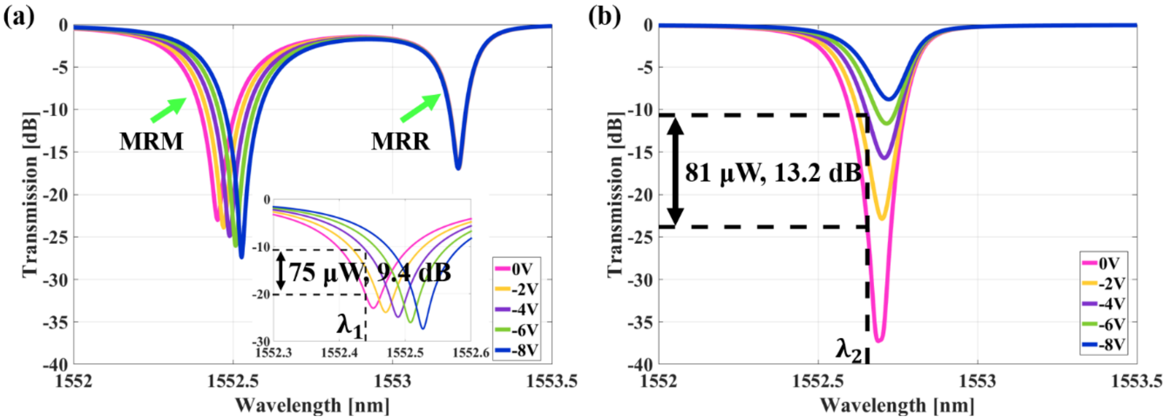

Fig. 4-7. Simulated DC transmission spectra when the resonances are (a) separated (inset: zoomed figure) and (b) overlapped. [45] (©2017 IEEE)

Figure 4-8 shows the normalized DC transmission spectra in the resonances separated and overlapped conditions. They are consistent with the simulated results. At -4 V bias, the OMA and ER at λ_1 are 54 μW and 8.1 dB when the resonances are separated. Under the same reverse bias voltage and at λ_2, they are increased to 77 μW and 12.9 dB when the resonances are overlapped. Table 9 summarizes the OMAs and ERs of the device in these two conditions, further proving that these two FOMs are largely improved by overlapping the resonances.

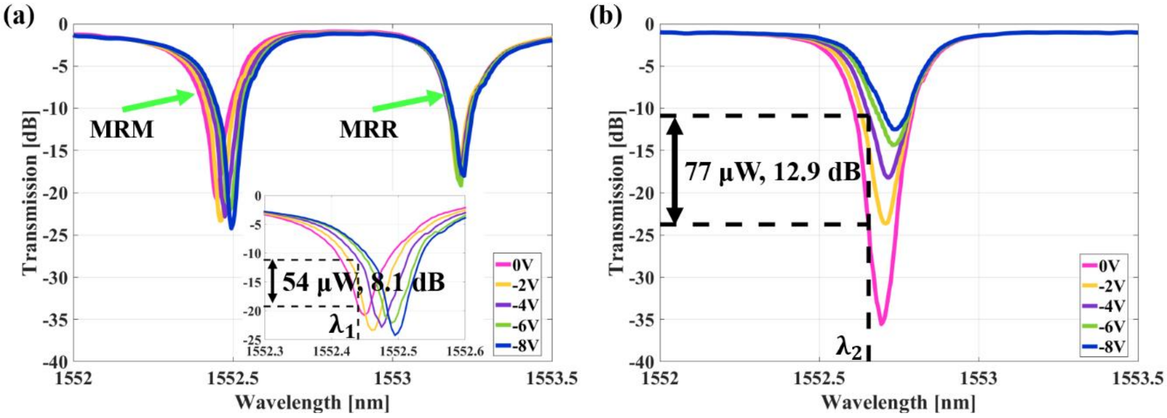

Fig. 4-8. Measured DC transmission spectra when the resonances are (a) separated (inset: zoomed figure) and (b) overlapped. [45] (©2017 IEEE)

Table 9. OMAs and ERs of the device. [45] (©2017 IEEE)

		-2 V	-4 V	-6 V	-8 V
OMA (μW)	Resonances separated	16	54	103	125
	Resonances overlapped	29	77	128	199
ER (dB)	Resonances separated	3.7	8.1	9.8	10.6
	Resonances overlapped	8.9	12.9	15.0	16.8

The main reason for the enhancement in the ERs is the larger static ER of the transmission spectrum in resonances overlapped condition, which means at 0 V bias, the power transmission at a wavelength close to the resonance is much smaller than that when the resonances are separated. For example, the marked power transmission at 0 V shown in Figs. 4-7(a) and 4-7(b) are approximately -20 dB and -24 dB, respectively. This is the predominant source of the simulated around 4-dB improvement in the ER. In the measurement, the power transmission under -4 V bias at λ_1 in the resonances separated condition is smaller than that at λ_2 in the resonances overlapped condition. In the simulation, these two values are almost identical. Since ER = $10\log_{10}(P_{-4V}/P_{0V})$ and ER = $P_{-4V} - P_{0V}$, the enhancements in the measured ER and OMA are both larger than the simulated values.

It should be noted there are two reasons may result in instability of the resonances overlap condition. First, the resonant wavelength of the microrings are sensitive to temperature changes. To solve this problem, a temperature controlling feedback loop, including a thermal sensor and a temperature controller, was applied in the experiment setup. Second, the heater may have degradation when it is biased for a long time or at a high voltage, and it also leads to a result that the two resonances are not perfectly overlapped. In our experiment, a DC voltage of 2 V was applied for approximately 6 hours, and in this case the resonances overlap condition was stable.

4.4 Large-signal modulation

4.4.1 OOK modulation

In this section, first we investigate and compare the OOK modulation performances of the single MRM and the single MRM-assisted MZI. The experimental setup of modulating the single

MRM is shown in Fig. 4-9(a). The RF signals applied on the MRM were 2^{31}-2 PRBS generated by an SHF BPG. They were amplified to have a peak-to-peak voltage of 1.8 V_{pp}, which was measured in a 50 Ω system. Using a bias tee of 65 GHz, a reverse bias voltage of 2.4 V and the RF signals were applied on the PN junction of the MRM. The optical input was 14 dBm from a C-band tunable laser. After modulation by the single MRM, the signals were amplified by an EDFA to 1 dBm. Then an PD with a TIA received the optical signals and converted them into electrical signals. Finally, a DCA was used to obtain the eye diagrams. The electrical module of the DCA had a bandwidth of 80 GHz, and no filter was applied in the experiment. For fair comparison, the parameters for modulating the single MRM-assisted MZI were kept the same to those for modulating the single MRM. The experimental setup is shown in Fig. 4-9(b). It should be noted that a DC voltage of 1.13 V was applied on the MRR to shift its resonant wavelength far away from that of the MRM. In this case, when focusing on the wavelengths around the resonance of the MRM, the device in Fig. 4-2(b) works as a single MRM-assisted MZI shown in Fig. 4-1(b), as explained in Section 4.2.

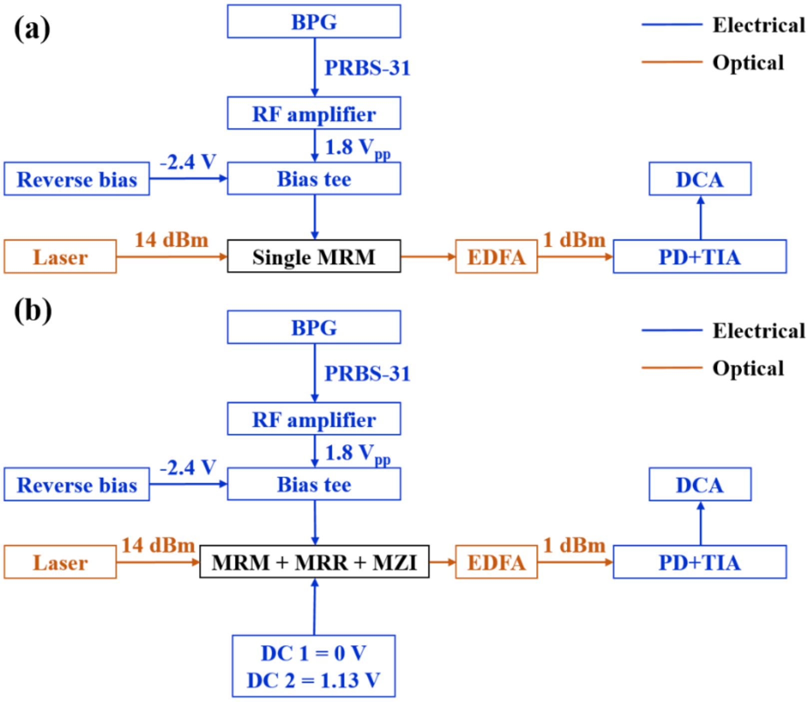

Fig. 4-9. Experimental setup for OOK modulation using (a) the single MRM and (b) the single MRM-assisted MZI. [43] (©2017 IEEE)

Figure 4-10 shows the received 40 Gb/s eye diagrams modulated. The modulation amplitude of the single MRM is 118 mV, and it is 221 mV using the single MRM-assisted MZI. As analyzed by the DC transmission spectra measurement in Section 4.3.1, the modulation efficiency of the two devices are identical. Therefore, the main reason of the improvement in the OOK modulation performance is the larger static ER by assisting the single MRM in a MZI.

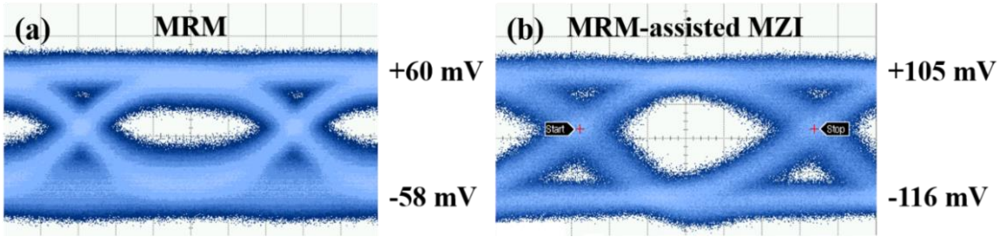

Fig. 4-10. Measured 40 Gb/s OOK eye diagrams modulated by (a) the single MRM and (b) the single MRM-assisted MZI. [43] (©2017 IEEE)

Then we further investigate the OOK modulation using the resonances overlap operation of the MRM and the MRR. As shown in Fig. 4-11, the driving RF signals, optical input and received power in the experimental setup were kept the same to those of the OOK modulation using the single MRM and the single MRM-assisted MZI shown in Fig. 4-10. However, there are three differences. First, a DC voltage of 2 V was applied on the heater of the MRM to achieve resonances overlap with that of the MRR, as shown in Figs. 4-1(c) and 4-6(a). Second, the modulated optical signals were transmitted over 0 to 2 km of SSMF. Third, a BERT was applied to measure the BERs for quantitatively evaluate the performance of the operating principle.

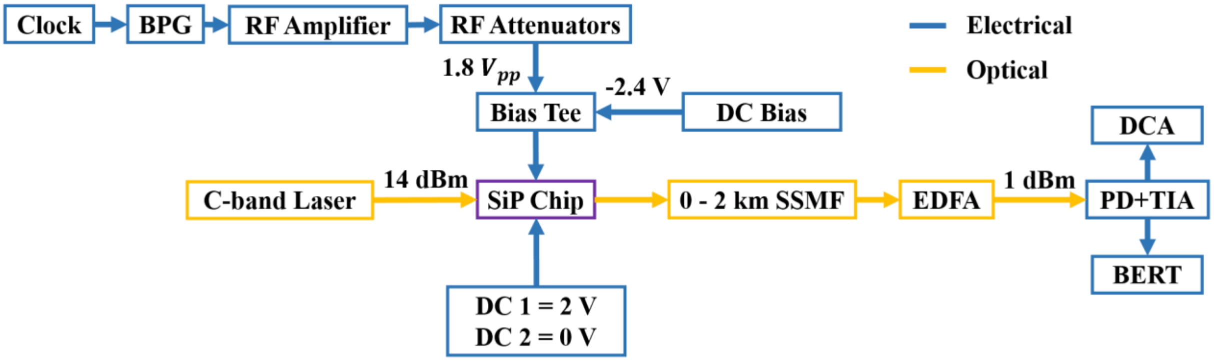

Fig. 4-11. Experimental setup for OOK modulation using the resonances overlap operation of the MRM with the MRR. [45] (©2017 IEEE)

The measured BER in the B2B transmission is demonstrated in Fig. 4-12(a), in which both the HD FEC threshold of 3.8 × 10^{-3} [120] and the KP4 FEC threshold of 2.2 × 10^{-4} [121] are shown for performance evaluation. It achieves error free modulation at 38 Gb/s, and the BER at 56 Gb/s is still below the HD FEC threshold. It means that the device using the resonances overlap operation can achieve error free (the post-FEC BER below 10^{-15} [120]) OOK modulation at a gross bit rate of 56 Gb/s, or equivalently, at a net bit rate of 50 Gb/s. The measured eye diagrams at 40 Gb/s and 50 Gb/s are shown in Figs. 4-12(b) and 4-12(c), respectively. They are both clearly open, and their measured Q-factors are 7.23 and 5.23.

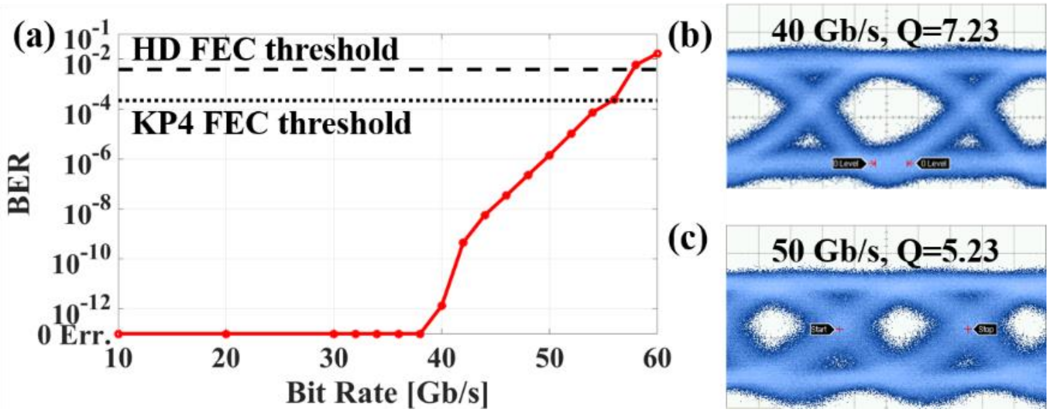

Fig. 4-12. Measured (a) BERs, eye diagrams at (b) 40 Gb/s and (c) 50 Gb/s of the B2B OOK modulation using the resonances overlap operation. [45] (©2017 IEEE)

We further investigate the OOK transmission performances over 0 to 2 km of SSMF, and the measured results are shown in Fig. 4-13. The device using the resonances overlap operation can transmit 56 Gb/s OOK signals over 2 km of SSMF with a measured BER below the HD FEC threshold, as shown in Fig. 4-13(a). The 40 Gb/s and 50 Gb/s eye diagrams after 2 km of SSMF transmission are still clearly open, with measured Q-factors of 6.97 and 4.97, respectively.

4.4.2 PAM-4

The PAM-4 transmission is based on DSP with modifications from that is shown in Fig. 3-15 and described in Section 3.5.2. The experimental setup is illustrated in Fig. 4-14, and the device shown in Fig. 4-2(b) works as a single MRM-assisted MZI and an MRM with resonances overlapped with an MRR by applying different DC voltages on the MRR heater and MRM

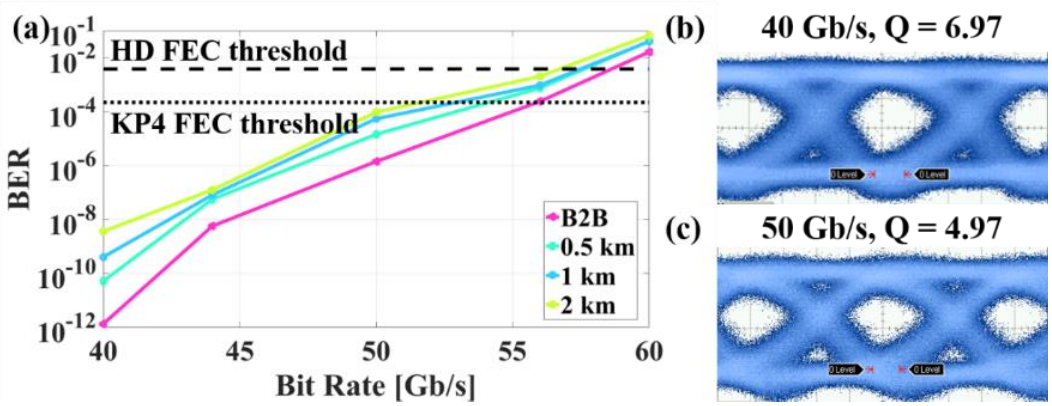

Fig. 4-13. Measured OOK (a) BERs, eye diagrams at (b) 40 Gb/s and (c) 50 Gb/s after 2 km of SSMF transmission using the resonances overlap operation. [45] (©2017 IEEE)

heater, respectively. It should be noted that PAM-4 experiment using the single MRM in Fig. 4-1(b) was also conducted but it is not successful. This is because the measured static ER of the MRM is only approximately 1.5 dB, which limits the modulation amplitude and results in a SNR not enough for PAM-4.

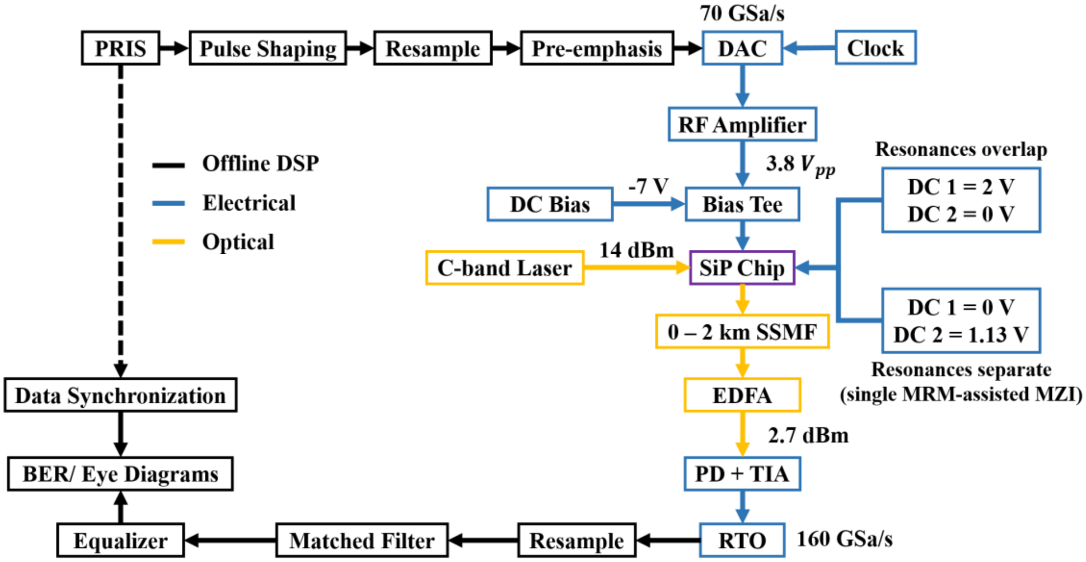

Fig. 4-14. Experimental setup of PAM-4 transmission using the device as a single MRM-assisted MZI and an MRM with resonances overlapped with an MRR. [45] (©2017 IEEE)

As shown in Fig. 4-14, the offline DSP generated a four-level PRIS, then used an RRC filter on it for pulse shaping, resampled it to 70 GSamples/s and applied a pre-emphasis filter on it.

Similarly, the length of the PRIS depended on the baud rate and the numbers were kept the same to those listed in Section 3.5.2. Based on the processed digital sequence, the DAC generated the RF signals. The peak-to-peak voltage was measured to be 3.8 V_{pp} in a 50 Ω system, and the bias voltage was -7 V. As shown in Fig. 4-6(a), a DC voltage of 2 V was applied on the MRM heater to achieve resonances overlap, and a 1.13-V voltage was applied on the MRR heater to make the device work as a single MRM-assisted MZI. The 14-dBm input laser light was modulated and afterwards the optical signals were transmitted over SSMF ranging from 0 to 2 km. An EDFA was applied to amplify the signals to 2.7 dBm. This value was larger than that in the OOK transmission setup as PAM-4 requires a larger SNR. The optical signals were received and converted to electrical signals by a PD with a TIA, then were captured by a RTO working at 160 GSamples/s. On the receiver side, the offline DSP resampled the data to 2 samples/symbol, applied a matched RRC filter and then an equalizer. After comparing the processed data to the synchronized PRIS on the transmitter side, the BERs were obtained and the eye diagrams were plotted.

The measured B2B PAM-4 BERs of the device in the resonances separated and overlapped conditions are shown in Fig. 4-15(a). When the device works as a single MRM-assisted MZI, its BER is below the HD FEC threshold at 76 Gb/s. While using the resonances overlap operation, it can achieve 56 Gb/s error free modulation using the transmitted data block, which means the

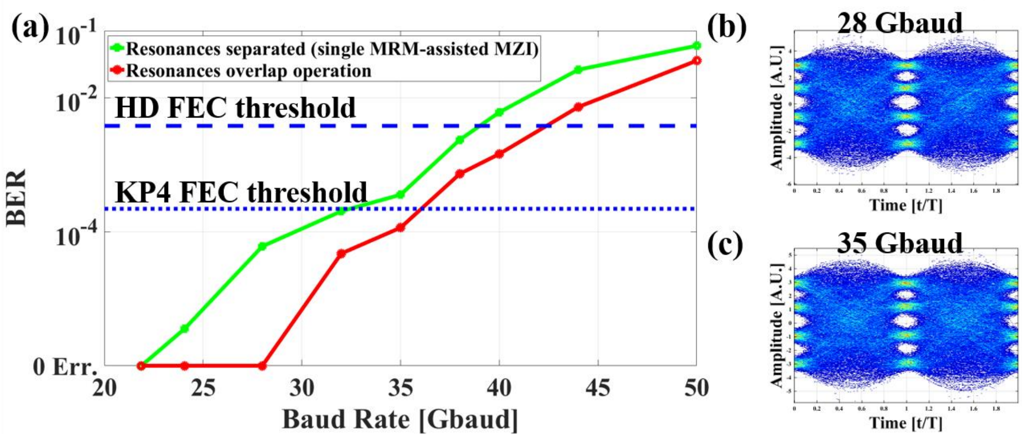

Fig. 4-15. Measured B2B PAM-4 (a) BERs when the resonances are separated and overlapped, eye diagrams at (b) 56 Gb/s and (c) 70 Gb/s after 2 km of SSMF transmission using the resonances overlap operation. [43, 45] (©2017 IEEE)

measured BER is lower than 1 × 10^{-6}. This value is approximately 12 Gb/s larger than that of the single MRM-assisted MZI. 80 Gb/s B2B transmission with the measured BER below the HD FEC threshold. Figures 4-15(b) and 4-15(c) show the eye diagrams at 56 Gb/s and 70 Gb/s when the resonances are overlapped, with the four levels clearly distinguished.

Using the resonances overlap operation, the modulated optical signals are further transmitted over 0 to 2 km of SSMF. The measured BERs are presented in Fig. 4-16(a), showing that the measured BER at 80 Gb/s even after 2 km of SSMF transmission is still below the HD FEC threshold. In Figs. 4-16(b) and 4-16(c), the clearly open eye diagrams at 56 Gb/s and 70 Gb/s after transmission over 2 km of SSMF are demonstrated, respectively.

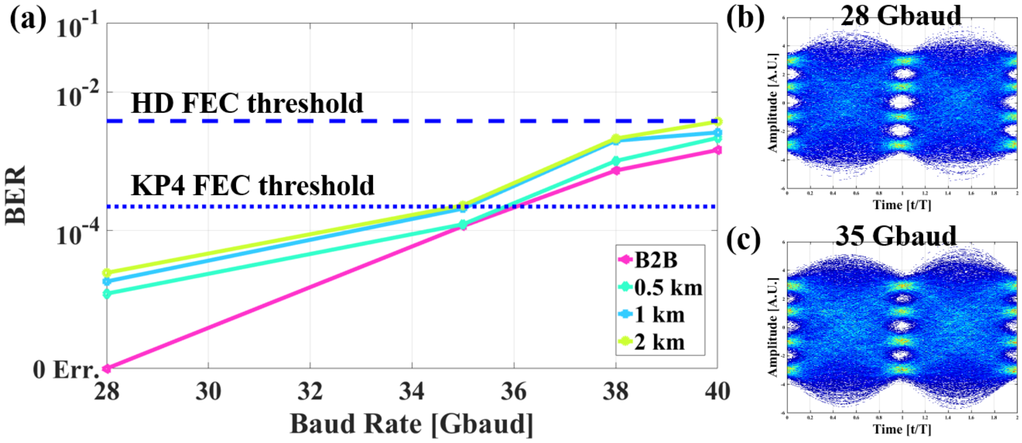

Fig. 4-16. Measured PAM-4 (a) BERs, eye diagrams at (b) 56 Gb/s and (c) 70 Gb/s after transmission over 2 km of SSMF using the resonances overlap operation. [45] (©2017 IEEE)

It should be noted that as the operating wavelength is in the C-band, CD is a problem for a longer transmission distance. This operating principle can be used in O-band applications, where the group velocity dispersion is zero at around 1310 nm [123]. In this case, transmission over longer distances of SSMF are expected.

4.5 Other resonances overlap operation

As shown in Fig. 4-2(b), there are also two heaters in the device design, one on each of the MZI arms. After fabrication, only one of the heaters is connected to the metal pads. Therefore, in addition to applying a DC voltage on the MRM heater to overlap the resonances, applying a DC voltage on the MZI heater can also achieve resonances overlap. Figure 4-17 shows the measured DC transmission spectra when applying 3.05 V on the MZI heater and applying reverse bias voltages on the PN junction of the MRM. At 0 V bias. In this case, the device has only one resonance, but this is not due to the resonant wavelength shift of the MRM. It is the phase change on the MZI arm in which the MRM is assisted that results in the overlapped resonances. The device in this configuration has a 360-pm FWHM, a static ER of 31.7 dB and a Q-factor of 4,300. The measured OMAs and ERs at different bias voltages at λ_2, the same bias wavelength to that shown in Figs. 4-7(b) and 4-8(b), are summarized in Table 10. Compared to the measured values when the resonances are separated, the OMAs of the device in this configuration are even smaller though the ERs are slightly enhanced. Therefore, the large signal modulation is not achieved using this resonance overlap operation. Overall, when the resonances are overlapped by applying a DC voltage on the MRM heater, which is elaborated in Section 4.3.2, the measured OMAs and ERs are the largest among all the three configurations.

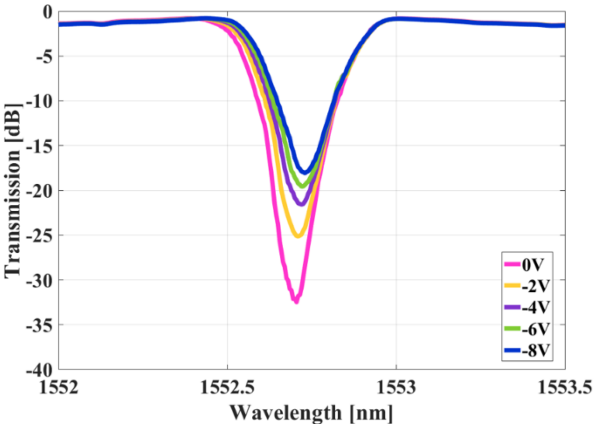

Fig. 4-17. Measured DC transmission spectra when applying a 3.05-V DC voltage on the MZI heater and various reverse bias voltages on the PN junction of the MRM.

Table 10. OMAs and ERs of the device when applying a 3.05-V DC voltage on the MZI heater to achieve resonances overlap.

	-2 V	-4 V	-6 V	-8 V
OMA (μW)	11	34	56	82
ER (dB)	7.0	11.3	13.4	14.9

In the operations introduced in the previous sections, the MRM being modulated has a shorter resonant wavelength than the one being used as a passive MRR. As shown in Fig. 4-2(b), both microrings are designed to have PN junctions. Therefore, the microring with a longer resonant wavelength can also be modulated to work as an MRM, and the other microring can be used as a passive MRR. Figure 4-18 shows the measured DC transmission spectra when applying reverse bias voltages on the PN junction of the other microring, who has a longer resonant wavelength. In Fig. 4-18(a), a 1.13-V DC voltage is applied on the MRM heater so the resonances are separated. In Fig. 4-18(b), a 2-V DC voltage is applied on the MRR heater and the resonances are overlapped. In Fig. 4-18(c), a 3.05-V DC voltage is applied on the MZI heater to achieve resonances overlap. Unlike those in Fig. 4-8(b) and Fig. 4-17, the measured DC transmission spectra in Figs. 4-18(b) and 4-18(c) have separated resonances when applying higher reverse bias voltages. Compared to the operation shown in Fig. 4-8(b), the operations shown in Figs. 4-17 and 4-18 do not have better measured OMAs and ERs. Therefore, they are not chosen for large signal modulation.

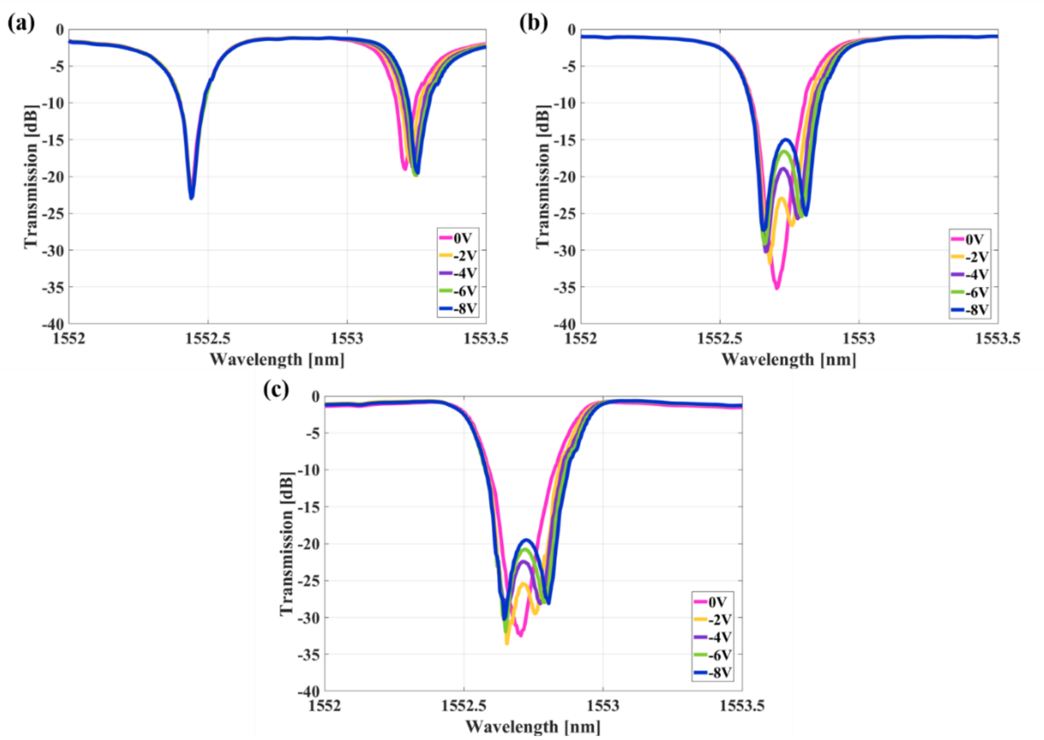

Fig. 4-18. Measured DC transmission spectra by applying bias voltages on the other microring and DC voltages on (a) The MRM heater, (b) the MRR heater and (c) the MZI heater. [44]

4.6 Conclusion

In this chapter, the operating principle of overlapping the resonances of an MRM with an MRR for PAM-4 transmission with better OMAs and ERs is introduced and elaborated. First, both simulation and measurement prove that by assisting an MRM in one arm of a balanced MZI, the static ER is largely enhanced by more than 18 dB [43]. Compared to the OOK modulation by the single MRM, clearer eye diagrams with larger modulating amplitudes are also observed using the single MRM-assisted MZI [43]. When assisting a passive MRR on the other MZI arm and applying a DC voltage on the MRM heater to achieve resonances overlap, even better OMAs and ERs are obtained from the simulated and measured DC transmission spectra. In this configuration, the device achieves 56 Gb/s OOK transmission and 80 Gb/s PAM-4 transmission over 2 km of SSMF [45].

Chapter 5

DAC-less and DSP-free dual-drive operation

5.1 Overview

As introduced in Chapter 1, PAM-4 short-reach transmission systems are cost-saving candidates for the next generation intra-data center applications, and they have been demonstrated based on SiP TWMZMs [6, 7] and MRMs [18, 60]. To further reduce the power consumption, PAM-4 signals generation without the use of DAC or DSP (e.g. pre-emphasis, pulse shaping, equalization, etc.) in the whole transmission link is favored. It has been achieved using MZI-assisted ring modulator [31], TWMZMs [32-35], cascaded dual MRMs [36], segmented MRM [37], push-pull segmented SISCAP modulators [38] and dual parallel GeSi EAMs [39]. Their performances are summarized in Table 6 in Section 2.3.3.

In this chapter, DAC-less and DSP-free dual-drive operation for PAM-4 signals generation and short-reach transmission is realized using two SiP modulator structures, a RAMZI modulator and an MIM. The content in this chapter is based on the author’s work in [46-48]. In the RAMZI structure, the dual parallel MRMs are both in the over-coupled condition. Moreover, they are biased at different wavelengths, driven by RF signals with different peak-to-peak voltages and bias voltages for PAM-4 signals generation with reasonable even spacings. As a result, there are large phase differences between the modulated ‘0’ and ‘1’ states of each MRM. In this case, the dual-drive operation using the RAMZI modulator is analyzed based on both the response of each MRM and the transmission of the whole device. In the dual-drive MIM, the two parallel phase shifters are designed to be identical and they do not have much phase difference. Therefore, only the power transmission of the whole device is investigated for PAM-4 signals generation with reasonable even spacings. In addition, MIMs with two different PN junction designs, one has four asymmetric doping concentrations and the other has six symmetric doping concentrations, are compared by simulation and measurement.

This chapter is organized as follows. In Section 5.2, the dual-drive operation of a RAMZI modulator is demonstrated. The device design and fabrication are presented in Section 5.2.1. Afterwards, the operating principle of PAM-4 signals generation is elaborated using system-level simulation and numerical analysis in Section 5.2.2. The device characterization, including the measured modulation efficiencies, the transmission of the whole device and the small-signal S parameters, is presented in Section 5.2.3. Then the PAM-4 experiment and results are shown in Section 5.2.4. In Section 5.3, the dual-drive operation of an MIM is demonstrated. The design, simulation and comparison of two different PN junctions are shown in Section 5.3.1. Following are the device designs and fabrication methods in Section 5.3.2. The measured DC transmission spectra for analyzing PAM-4 signals generation are shown in Section 5.3.3, and the small-signal S parameters of the devices are reported in Section 5.3.4. Then the PAM-4 transmission results are presented in Section 5.3.5. Finally, this chapter is concluded in Section 5.4.

5.2 Dual-drive operation of a RAMZI modulator

In this section, we present the DAC-less and DSP-free PAM-4 signals generation and short-reach transmission based on a dual-drive RAMZI modulator. The operating principle is analyzed using system-level simulation, as well as the numerical analysis of each MRM and the whole device. PAM-4 optical signals with reasonable even spacings are generated from 15 Gbaud to 25 Gbaud. 40 Gb/s 5 km and 50 Gb/s 2 km PAM-4 short-reach transmissions are demonstrated with the estimated BERs below the HD FEC threshold.

5.2.1 Device design and fabrication

As shown in Fig. 5-1(a), the RAMZI modulator has the same geometric parameters and identical PN junction design to those demonstrated in Figs. 3-1 and 3-2, except the radii of the two MRMs are 40 μm. In this design, the straight-through coupling coefficient is simulated to be 0.7443 using Lumerical FDTD Solutions [74], the round-trip attenuation is simulated to be 0.9847 using

Lumerical MODE Solutions [70] and Lumerical Device [76]. The simulated modulation efficiencies are 11.3 pm/V at -4.6 V bias and 9.9 pm/V at -7 V bias. The device was fabricated at IME A*STAR using the same process described in Section 3.2, and the micrograph of the fabricated device is shown in Fig. 5-2(b). In the dual-drive operation, a DC voltage is applied on the heater of MRM 1 for aligning the resonances, and two independent binary RF signals are applied on the two MRMs simultaneously.

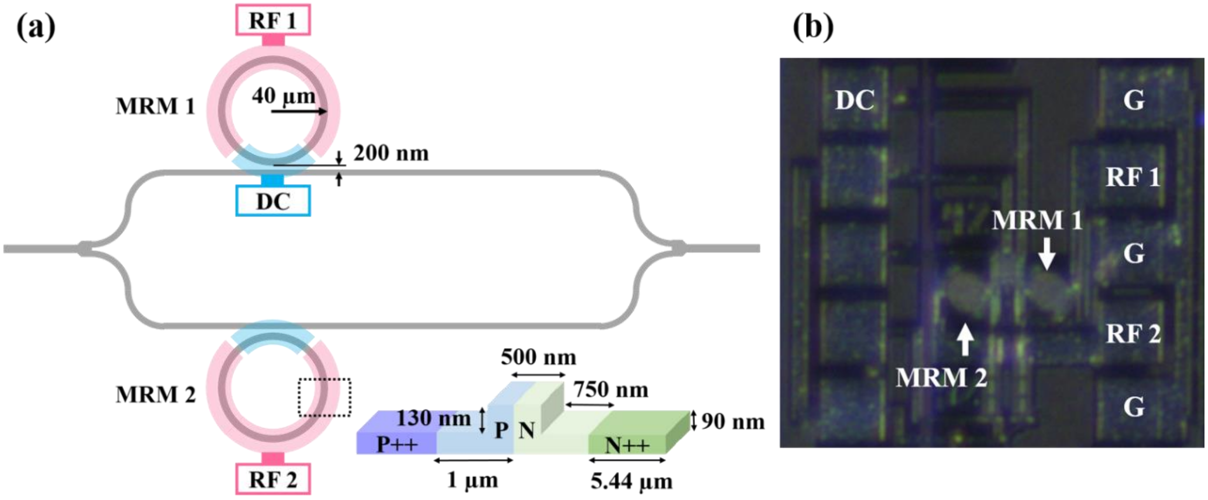

Fig. 5-1. (a) Schematic structures of the RAMZI modulator and the PN junction, (b) micrograph of the fabricated device. [46] (©2017 IEEE)

5.2.2 Operating principle

When applying DC voltages on the PN junctions of the two MRMs simultaneously, i.e. V_1 on MRM 1 and V_2 on MRM 2, the transfer function T (V_1, V_2) of the RAMZI is:

$$T(V_1,V_2)=\frac{1}{4}\left|\sqrt{T_1(V_1)}e^{j\phi_1(V_1)}+\sqrt{T_2(V_2)}e^{j\phi_2(V_2)}\right|^2 \tag{5.1}$$

in which T_1, T_2 are the power transmission of the two MRMs, and ϕ_1, ϕ_2 are their phase responses. These four parameters are all dependent on the applied DC voltages. The factor ¼ is because of the two 3-dB Y-branches [118] in the device.

To generate PAM-4 optical signals with even spacings, the response of each MRM should be considered, as shown in Eq. 5.1. Since these two MRMs are both designed to be in the over-coupled condition, their phases have 2π change across the resonant wavelengths. In this case, there are large phase differences between the ‘0’ and ‘1’ states of the modulated binary optical signals by each MRM. In addition, the phase difference between the two MRMs is also large. Therefore, the bias wavelengths and the parameters of the driving RF signals on each MRM should be carefully chosen.

For further explanation on the operating principle, we simulate the power transmission and phase responses of the two individual MRMs in Lumerical Interconnect [113] using the setup shown in Fig. 5-2(a). Their effective indices (n_{eff1} = 2.5190, n_{eff2} = 2.5191) and the straight-through coupling coefficients (σ_1 = 0.7443, σ_2 = 0.8943) are intentionally set to be slightly different to model the deviations in the fabrication process. The round-trip attenuation is set as the simulated value of 0.9847 for the two MRMs. The applied DC voltages are $V_{1,1}$ = -1.85 V, $V_{1,2}$ = -2.5 V on RF pad of MRM 1 and $V_{2,1}$ = 0 V, $V_{2,2}$ = -0.65 V on RF pad of MRM 2. These four voltages correspond to driving RF signals with V_{pp1} = 0.65 V, V_{bias1} = -2.175 V on MRM 1 and V_{pp2} = 0.65 V, V_{bias2} = -0.325 V on MRM 2. The system-level simulation setup of the RAMZI is shown in Fig. 5-2(b), in which all the simulation parameters are set to be the same as those in Fig. 5-2(a).

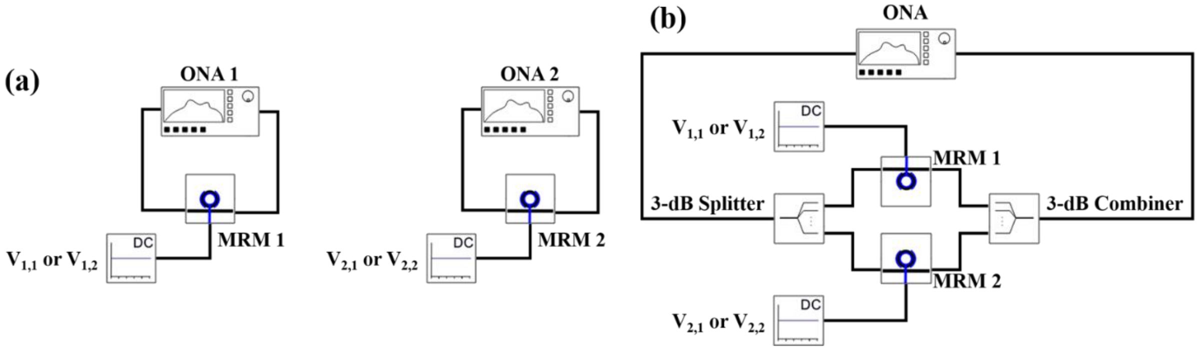

Fig. 5-2. Simulation setups of (a) two individual MRMs and (b) RMAZI modulator. [46] (©2017 IEEE)

The simulated power transmission and phase responses of the two MRMs at different applied voltages are shown in Fig. 5-3. The bias wavelength λ is chosen to generate four power levels by combining the simulated responses using Eq. 5.1. At λ, $T_1(V_{1,1})$ = 0.8227, $T_1(V_{1,2})$ = 0.8830, $T_2(V_{2,1})$ = 0.7746, $T_2(V_{2,2})$ = 0.8993, and the phases are $\phi_1(V_{1,1}) = -0.9826\pi$, $\phi_1(V_{1,2}) = -0.7952\pi$, $\phi_2(V_{2,1}) = -0.4725\pi$, $\phi_2(V_{2,2}) = -0.3410\pi$. Consistent with the analysis, there are large phase differences between each state. Based on these simulated values, the calculated four levels of power transmissions are T ($V_{1,1}$, $V_{2,1}$) = 0.3867, T ($V_{1,2}$, $V_{2,1}$) = 0.6330, T ($V_{1,1}$, $V_{2,2}$) = 0.2454, and T ($V_{1,2}$, $V_{2,2}$) = 0.5095. The spacings between adjacent levels are 0.1413, 0.1228 and 0.1235, respectively, which are reasonable for PAM-4 signals generation. It should be noted that the phase differences between the four output power levels are large, which results in a large modulation chirp using this operating principle.

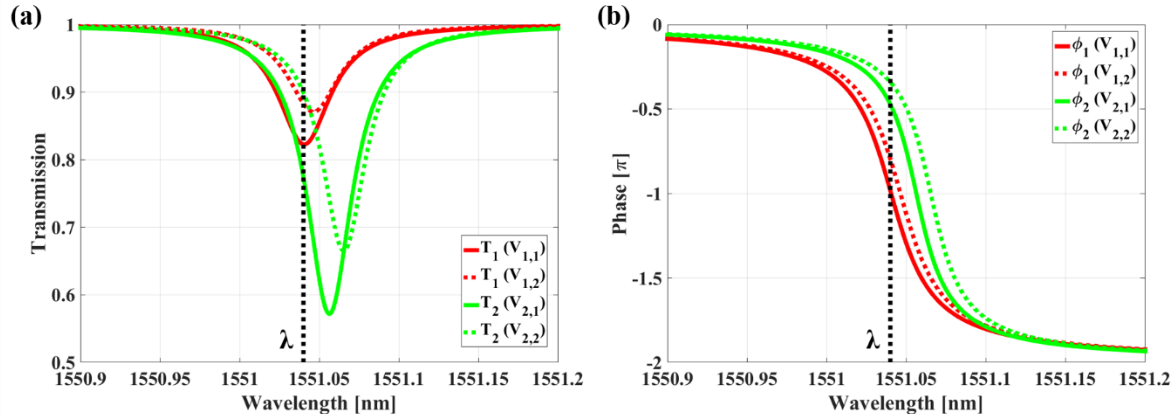

Fig. 5-3. Simulated (a) power transmission and (b) phase responses of the two individual MRMs when applying different voltages on their RF pads respectively. [46] (©2017 IEEE)

Based on the setup in Fig. 5-2(b), the power transmission of the RAMZI is also simulated and the results are shown in Fig. 5-4. The four power levels '00', '01', '10' and '11' at the marked

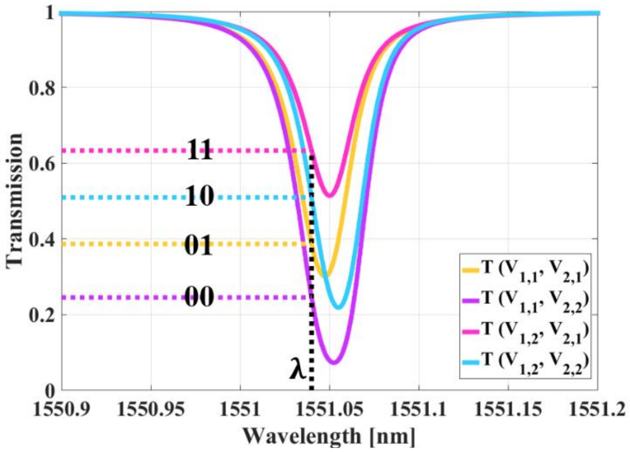

Fig. 5-4. Simulated power transmission of the RAMZI when applying voltages on the RF pads of the two MRMs simultaneously. [46] (©2017 IEEE)

wavelength λ are the same to the calculated values, further proving that the dual-drive operating principle can achieve PAM-4 signals generation with reasonable even spacings.

5.2.3 Device characterization

Figure 5-5 shows the measured DC transmission spectra by applying reverse bias voltages from 0 to 10 V on the RF pads of the two MRMs respectively. The total on-chip IL is approximately 14.0 dB, and there are two resonant wavelengths apart by 315 pm in the passive transmission spectrum. The measured modulation efficiencies of the two MRMs under -4 V bias voltage are 7.5 pm/V and 8.75 pm/V, respectively. The differences in the measured resonant wavelengths and modulation efficiencies are due to the variations in the fabrication process.

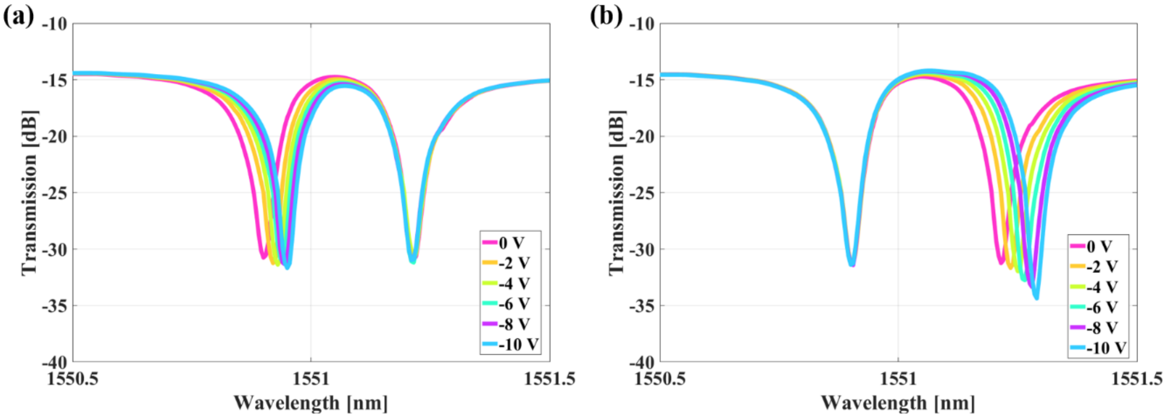

Fig. 5-5. Measured DC transmission spectra by applying reverse bias voltages on the RF pad of (a) MRM 1 and (b) MRM 2.

In Fig. 5-6, the resonance shifts and modulation efficiencies of the two MRMs are shown. They are extracted from the measured DC transmission spectra with a 0.25-V step for the applied bias voltages. For MRM 1, the measured modulation efficiency is 8.2 pm/V at -7 V bias, and it is 9.6 pm/V at -4.6 V bias for MRM 2. They are both smaller than the simulated values, which is mainly due to the fabrication deviations.

For PAM-4 signals generation, a DC voltage of 1.95 V is applied on the heater of MRM 1 to align the two resonances. By applying reverse bias voltages on the RF pads of the two MRMs simultaneously, the normalized power transmission of the RAMZI at the operating wavelength λ is plotted in Fig. 5-7(a). The marked points are the four levels of power transmission which

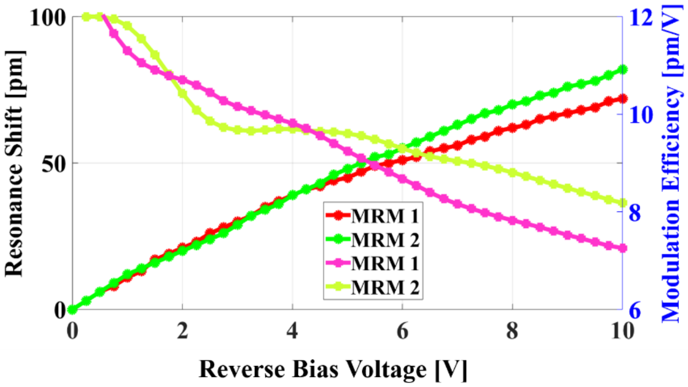

Fig. 5-6. Measured resonance shifts and modulation efficiencies by applying reverse bias voltages on the RF pad of the two MRMs respectively. [46] (©2017 IEEE)

have reasonable even spacings, and they are located at the voltages required for the PAM-4 generation. Figure 5-7(b) shows the normalized transmission spectra of the RAMZI at these four combinations of bias voltages. The measured four levels are 0.443, 0.381, 0.325 and 0.273, corresponding to modulation losses of 3.5 dB, 4.2 dB, 4.9 dB and 5.6 dB. Based on the four voltages, which are $V_{1,1}$ = -4.9 V, $V_{1,2}$ = -9.1 V, $V_{2,1}$ = -3.0 V, $V_{2,2}$ = -6.2 V, the driving RF signals are chosen to have V_{pp1} = 4.2 V, V_{bias1} = -7 V, V_{pp2} = 3.2 V, and V_{bias2} = -4.6 V.

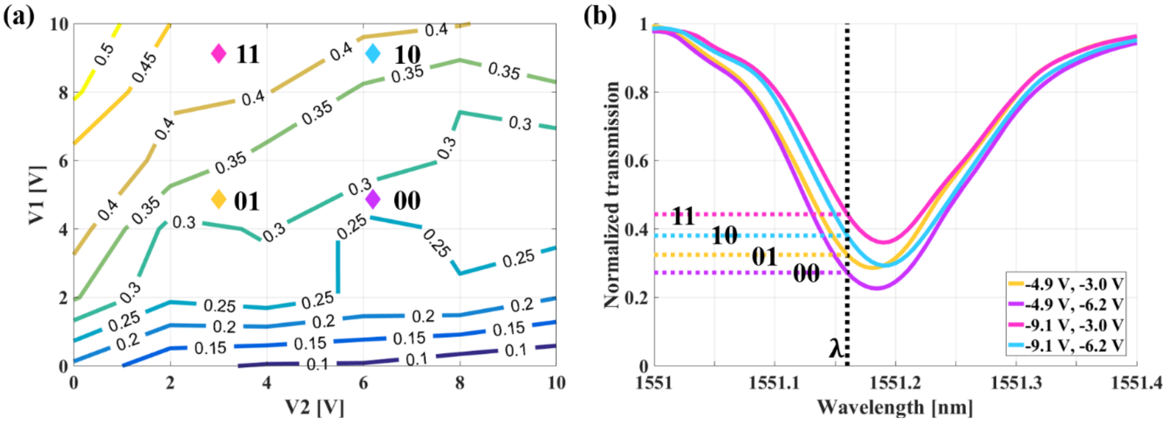

Fig. 5-7. Normalized (a) power transmission at λ and (b) DC transmission spectra of the RAMZI with reverse bias voltages applied on the RF pads of the two MRMs simultaneously. [46] (©2017 IEEE)

The EO S_{21} magnitudes are measured by biasing the RAMZI at the operating wavelength λ and applying small RF signals with the required bias voltages on the RF pads of the two MRMs respectively. As shown in Fig. 5-8, the 3-dB EO bandwidth of MRM 1 at -7 V bias is 13.5 GHz, and that of MRM 2 at -4.6 V bias is 19.3 GHz. As introduced in Section 2.3.1, a larger wavelength detuning from the resonance results in a larger EO bandwidth. In the measurement, an optical peaking effect is also observed when biasing at even larger detuning. These phenomena have been analyzed thoroughly in [85] and [86], so the measured figures are not shown in this thesis.

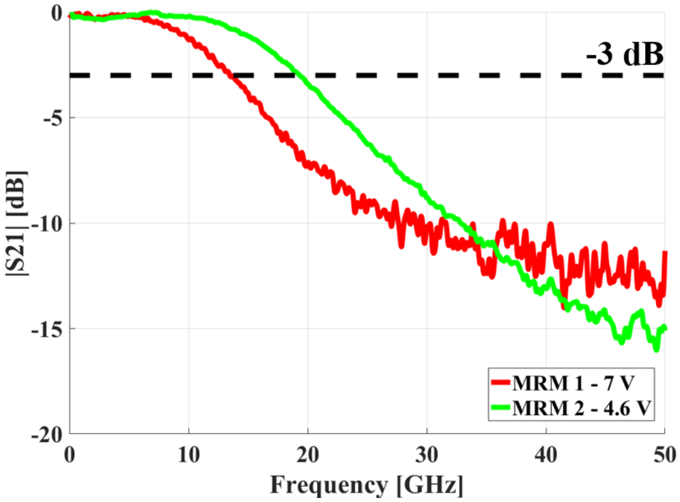

Fig. 5-8. Measured EO $|S_{21}|$ responses of MRM 1 at -7 V bias and MRM 2 at -4.6 V. [46] (©2017 IEEE)

5.2.4 PAM-4

Based on the experiment setup shown in Fig. 5-9, PAM-4 optical signals generation is achieved by applying two independent binary RF driving signals on the two MRMs in the RAMZI simultaneously. The 2^{31}-1 PRBS were generated by two channels of a BPG, and the time delay was adjusted using the control software of the BPG to correct any path mismatch between these two independent signals. Then they were amplified to have peak-to-peak voltages of 4.26 V_{pp} and 3.19 V_{pp}, respectively, which were measured in a 50 Ω system. They are slightly different from those chosen based on the measured power transmission of the RAMZI modulator, because there are RF attenuation in the cables and connectors. The bias voltages of V_{bias1} = -7 V and V_{bias2} = -4.6 V, which were also chosen based on the measurement and analysis in Section 5.2.3, were applied together with the RF signals on the two MRMs using 65-GHz bias tees. Also, a DC voltage of 1.95 V was applied on the heater of MRM 1 to align the two resonances for PAM-4 signals generation at the operating wavelength λ of 1551.16 nm. The 14-dBm laser input was coupled in the RAMZI and modulated, then the PAM-4 signals were launched into 0 – 5 km of SSMF. After being amplified by an EDFA, the average received power was kept at 2.15 dBm. A 35-GHz PD with a TIA received the signals, and a DCA was used to obtain the eye diagrams and estimate the BERs. In this experiment, there was no filter applied in the electrical module of the DCA.

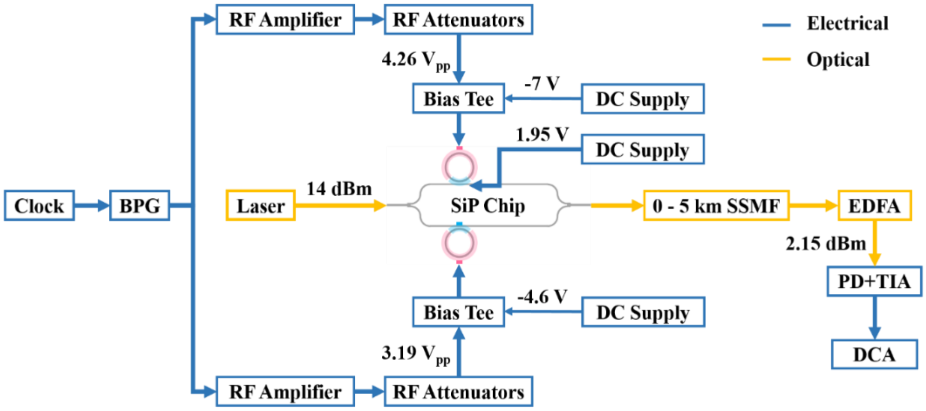

Fig. 5-9. Experimental setup for PAM-4 generation using the RAMZI modulator.

We first investigate the modulated OOK eye diagrams by turning on one of the driving RF signals on each of the MRMs at a time. As analyzed in Section 5.2.2, at the same bias wavelength, the two MRMs have different power transmission and phase responses since their resonant wavelengths and driving signals are both set to be different in the experiment. Therefore, as shown in Figs. 5-10(a) and 5-10(b), the modulation amplitudes of the 15 Gbaud eye disarms in the B2B configuration are 168 mV and 268 mV by the two MRMs, respectively. By turning on the driving RF signals on both the MRMs, the measured 15 Gbaud PAM-4 eye diagram in B2B configuration is shown in Fig. 5-10(c). The listed voltages prove that by combining the modulated signals by the two MRMs, the four levels have reasonable even spacings using the dual-drive operating principle on the RAMZI modulator. In Figs. 5-10(d), 5-10(e) and 5-10(f), the measured eye diagrams at 15 Gbaud after 5 km, at 20 Gbaud after 5 km and at 25 Gbaud after 5 km of SSMF transmission are demonstrated. The listed voltages also show that the four levels of the received signals are almost evenly spaced.

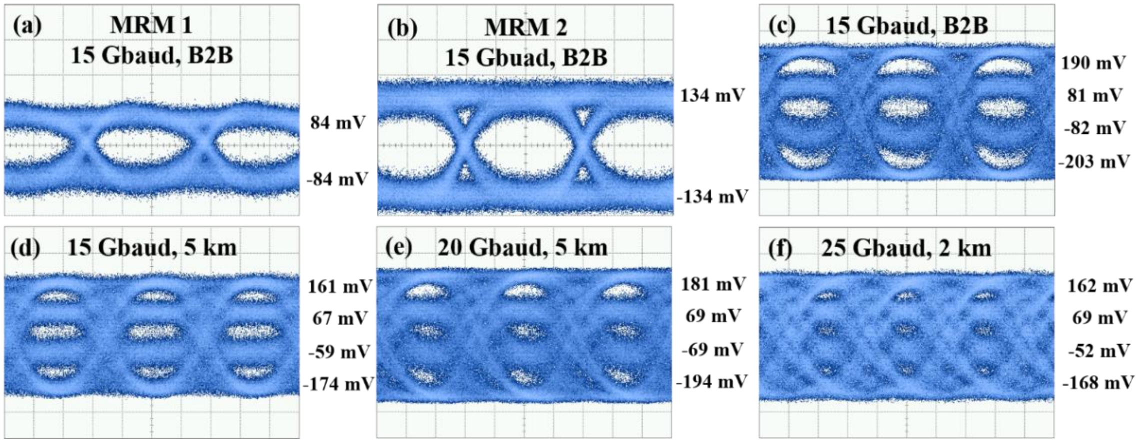

Fig. 5-10. Measured eye diagrams of (a), (b) 15 Gbaud modulated by MRM 1 and MRM 2 in B2B configuration, (c) 15 Baud PAM-4 in B2B configuration, (d) 15 Gbaud PAM-4 over 5 km, (e) 20 Gbaud over 5 km and (f) 25 Gbaud over 2 km of SSMF transmission. [46] (©2017 IEEE)

The BERs of the PAM-4 transmission are estimated using the vertical histograms of the captured eye diagrams by the DCA, based on the assumption that the noise has a Gaussian distribution [124]. The estimation method has been theoretically analyzed in [125] and experimentally applied in [32, 33, 125]. For example, the measured histograms of the 25 Gbaud eye diagrams after 2 km of SSMF transmission are shown in Fig. 5-11, with the mean values and standard deviations σ of each level listed. The calculated BER is 3.297 × 10^{-3}, which is below the HD FEC threshold.

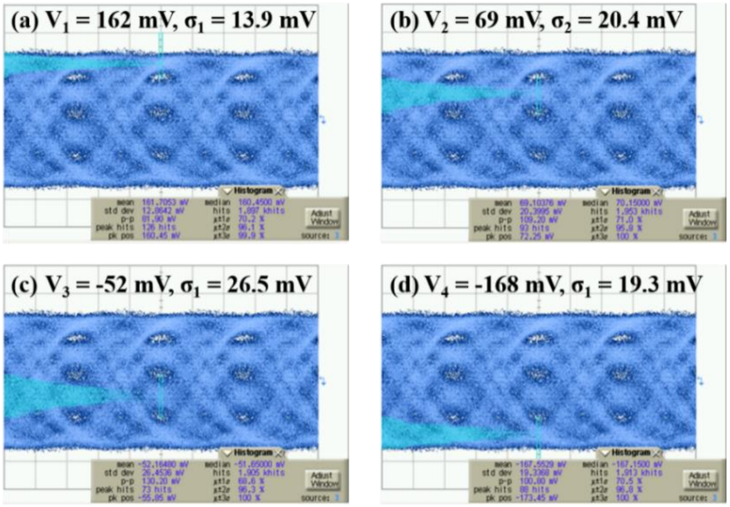

Fig. 5-11. Measured histograms of the 25 Gbaud eye diagrams after 2 km transmission.

Using the method in [32, 33, 125], the estimated BERs are shown in Fig. 5-12. Successful PAM-4 transmissions at 40 Gb/s over 5 km of SSMF and at 50 Gb/s over 2 km of SSMF are achieved, with BERs both below the HD FEC threshold.

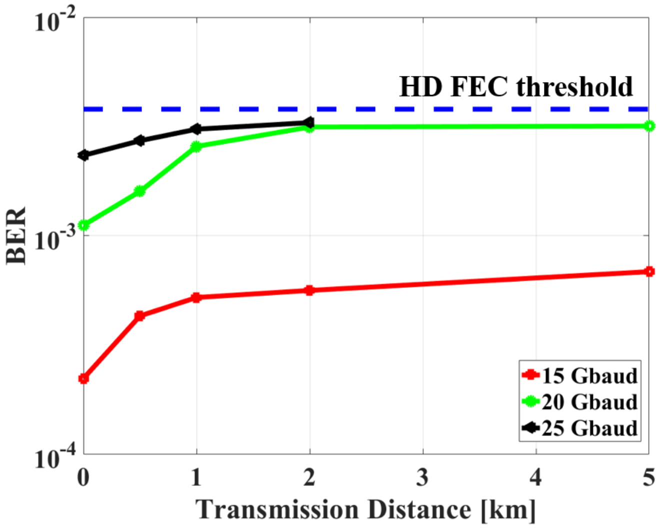

Fig. 5-12. Estimated BERs of PAM-4 transmission. [46] (©2017 IEEE)

It should be noted that the PAM-4 performance of the RAMZI modulator can be further improved by designing the MRMs with larger EO bandwidths and better modulation efficiencies at the working wavelength and bias voltages. In addition, by applying RF components with higher bandwidths and reducing the noise in the system, the dual-drive operating principle of the RAMZI modulator will achieve PAM-4 transmission at a higher bit rate. Implementing DSP also helps the performance enhancement, but it will increase the power consumption and complexity in the transmission link.

5.3 Dual-drive operation of an MIM

In this section, a dual-drive MIM is presented for the DAC-less and DSP-free PAM-4 signals generation and short-reach transmission. Two PN junction designs, one with four asymmetric doping concentrations and the other with six symmetric doping concentrations, are simulated and compared. The devices are designed and fabricated with these two PN junction designs. Then their DC characterizations are analyzed to elaborate on the operating principle for PAM-4 signals generation with reasonable even spacings. The measured EE and EO responses are also demonstrated to further characterize the devices. After 2 km of SSMF transmission, 56 Gb/s PAM-4 is successfully achieved with the measured BER below the HD FEC threshold, and the BER of 50 Gb/s PAM-4 is below the KP4 FEC threshold.

5.3.1 PN junction design and simulation

The asymmetric PN junction design with 4 doping concentrations, which is the same to that reported in [19], is shown in Fig. 5-13(a). The 500-nm × 220-nm rib waveguide is laterally PN doped with a misalignment of 100 nm. The light PN doping concentrations are for reducing the optical scattering loss in the rib waveguide. The widths of the P doped layer and N doped layer in the 90-nm slab waveguide are both 1 μm. There are also P++ and N++ doped regions with a width of 6.35 μm, which are designed for ohmic contact with the metal pads. They are both 1 μm away from the edge of the rib waveguide. The simulated peak doping concentrations in [19] are 7.8×10^{17} cm^{-3} for P, 2.1×10^{18} cm^{-3} for N, 3.9×10^{19} cm^{-3} for P++ and 9.7×10^{19} cm^{-3} for N++. As analyzed in Section 2.2.1, the change in the concentration of holes contribute more to the plasma dispersion effect [50]. Therefore, the PN junction is designed with a 100-nm offset to increase the overlap of the P doping area with the optical mode confide in the rib waveguide. This asymmetric design is expected to improve the modulation efficiency.

However, as reported in [66], the doping concentrations used in the IME MPW fabrication runs are 5×10^{17} cm^{-3} for P, 3×10^{17} cm^{-3} for N, 2×10^{18} cm^{-3} for P+, 3×10^{18} cm^{-3} for N+, and 1×10^{20} cm^{-3} for both P++ and N++. Because the P area has a larger doping concentration than the N area, PN junction design with an offset is not necessary. As the optical mode is confined in the middle of the rib waveguide, we redesign the PN junction to be symmetric, as shown in Fig. 5-13(b). In this case, the carrier depletion region, which is also in the middle of the rib waveguide, has more overlapping with the optical mode. Therefore, when applying reverse bias voltages to deplete the carriers, the effective index of the optical mode in the symmetric PN junction design will change more than that in the asymmetric design. In our design, the lightly doped P and N regions both have 250-nm widths in the rib waveguide and 120-nm widths in the slab-waveguide. The 810-mn P+ and N+ regions are designed for decreasing the junction resistance, which leads to an enhancement in the EO bandwidth of the device. To keep the total width of the PN junction the same to that in Fig. 5-12(a), which is 15.2 μm, the widths of the P++ and N++ layers are 6.42 μm.

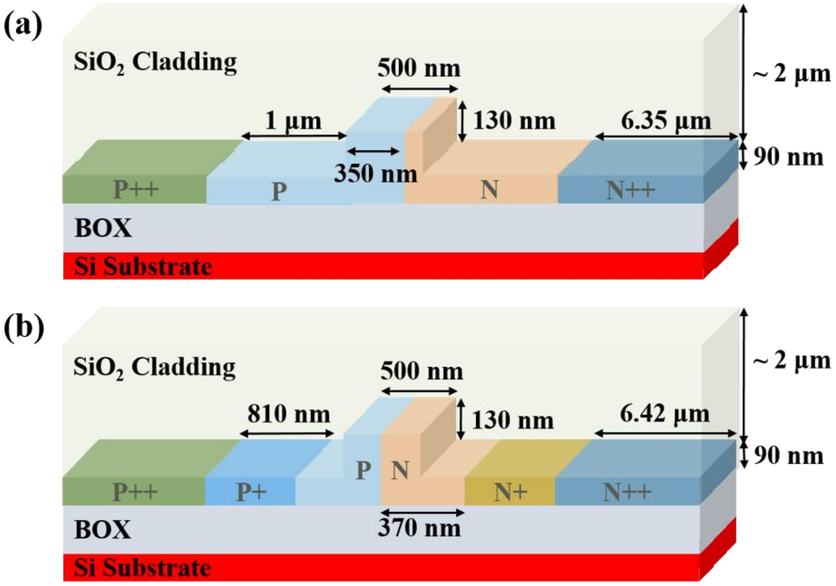

Fig. 5-13. Schematics of the PN junction designs with (a) 4 asymmetric doping concentrations and (b) 6 symmetric doping concentrations. [47]

Based on the doping concentrations in [66], these two PN junction designs are simulated in Lumerical Device [76] and Lumerical MODE Solutions [70] using the methods described in Section 2.2.3. One major difference between these two PN junction designs is the asymmetric lightly PN doped region in the rib waveguide in Fig. 5-13(a) is changed to symmetric design in Fig. 5-13(b). The other difference is the number of the doping concentration levels, which are 4 in Fig. 5-13(a) and 6 in Fig. 5-13(b). To investigate the specific reasons of the differences in their performances, the PN junction shown in Fig. 5-14, which has a symmetric design with 4 doping concentrations, is also simulated using the same method.

Figure 5-15 demonstrates the simulated effective index changes and the propagation losses when applying reverse bias voltages on the three PN junction designs. As shown in Fig. 5-15(a), by designing the PN junction with symmetric light doping concentrations in the rib waveguide, the effective index changes become larger, which results in a better modulation efficiency. As analyzed, this is because the carrier depletion region of the symmetric PN doping has a larger

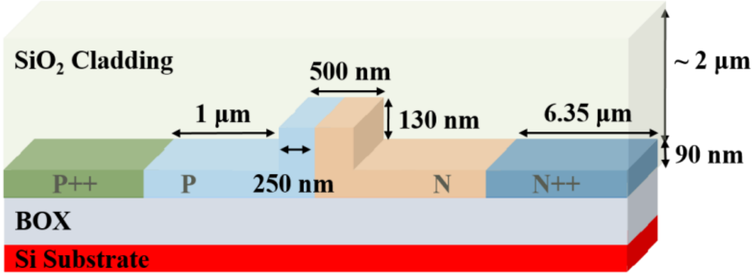

Fig. 5-14. Schematics of the PN junction with 4 symmetric doping concentrations. [47]

overlapping with the optical mode. In addition, implanting two more levels of P+ and N+ in the slab waveguide does not help in the improvement of the modulation efficiency, as shown by the blue and green curves in Fig. 5-15(a).

The propagation losses are reduced by designing the PN junction to be symmetric, as shown by the red and blue curves in Fig. 5-15(b). Since the P doping concentration is larger than the N doping concentration, decreasing the P region from 350 nm to 250 nm results in less optical scattering loss. By adding P+ and N+ regions in the slab waveguide, the propagation losses are larger since there are more carriers in the waveguide. It should be noted that when the applied reverse bias voltage is smaller than 4 V, the PN junction with symmetric 6 doping concentrations has larger losses than that with asymmetric 4 doping concentrations as it has more optical scattering loss. However, beyond 4 V reverse bias voltage, the losses are smaller since the carrier depletion is more effective in the PN junction with 6 doping concentrations than in that with 4 doping concentrations.

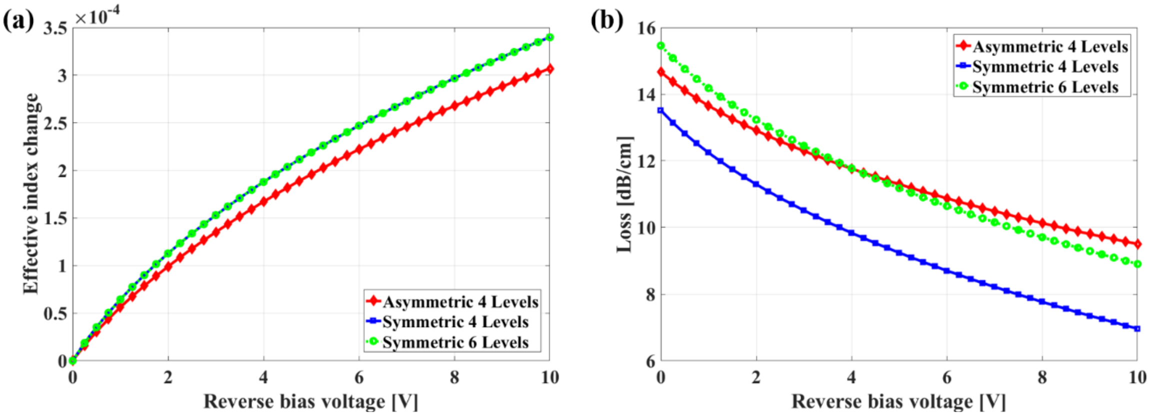

Fig. 5-15. Simulated (a) effective index changes and (b) losses of the PN junctions. [47]

The resistances of the three PN junctions at various reverse bias voltages are also simulated using the method described in Section 2.2.3, and they are summarized in Table 11. Whether the PN junction is designed to be asymmetric or symmetric does not influence much on the simulated junction resistances. However, it is obvious that by adding P+ and N+ doping regions, the junction resistances are decreased by more than 50% compared to those of the PN junctions with 4 doping concentrations. This is beneficial to increase the 3-dB cutoff frequency of the phase shifter, which as a result helps enhance the EO bandwidth of the device.

Table 11. Simulated resistances (Ω-cm) of the three PN junctions. [47]

	-2 V	-4 V	-6 V	-8 V	-10 V
Asymmetric 4 doping concentrations	1.3542	1.3535	1.3525	1.3510	1.3492
Symmetric 4 doping concentrations	1.3373	1.3364	1.3351	1.3335	1.3316
Symmetric 6 doping concentrations	0.6258	0.6236	0.6211	0.6184	0.6158

It should be noted that introducing the P+/N+ doping regions in the slab waveguide results in larger propagation losses and smaller PN junction resistances. As shown in Fig. 2-16(a), the propagation loss increases significantly starting from a P+/N+ region width of approximately 800 nm. However, as shown in Fig. 5-16(b), the PN junction resistance decreases almost linearly with the P+/N+ region width. A P+/N+ doping region width of 810 nm was used in the MIM design so that the propagation losses are no more than 2 dB/cm larger than those without applying P+/N+ doping, meanwhile the PN junction resistance decreases more than 50%.

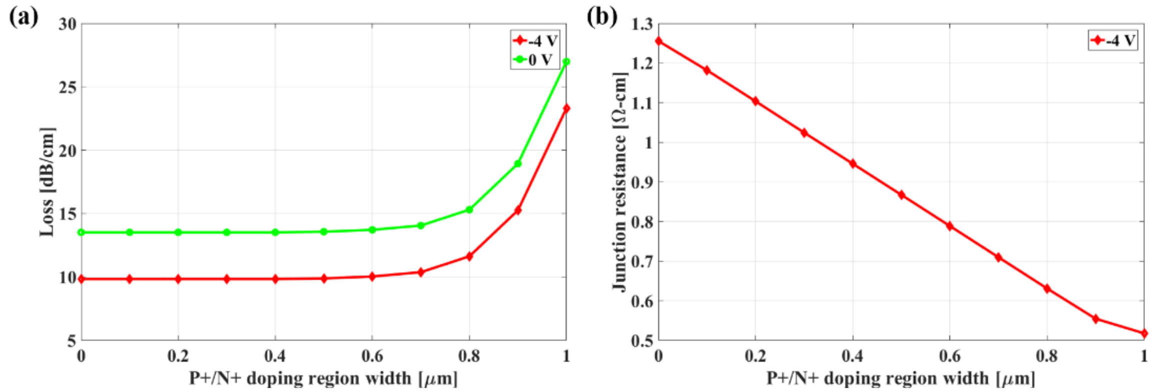

Fig. 5-16. Simulated (a) propagation losses at 0 V and -4 V bias voltages, (b) PN junction resistances at -4 V bias voltage with different widths of the P+/N+ doping regions. [47]

In conclusion, based on the doping concentrations in [66], we redesign the PN junction in [19] to be symmetric in the rib waveguide, and add P+/N+ regions in the slab waveguide. The simulated modulation efficiency is improved and the simulated junction resistance is largely decreased. They are both good for the device to have better modulation performances.

5.3.2 Device design and fabrication

As shown in Fig. 5-17, light is coupled into the device by a vertical GC and then goes through a 2 × 2 3-dB adiabatic coupler [126]. The two arms have an imbalance of approximately 200 μm, and the PN junctions are designed to be identical in the two 500-μm phase shifters. For dual-drive operation, metallization is applied on both phase shifters for applying independent binary RF signals. Since there are loop mirrors at the end of the device, light travels back and goes through the two arms twice. In this case, the modulation efficiency of the device is doubled. After travelling through the adiabatic coupler again, light is coupled out of the device by a vertical GC.

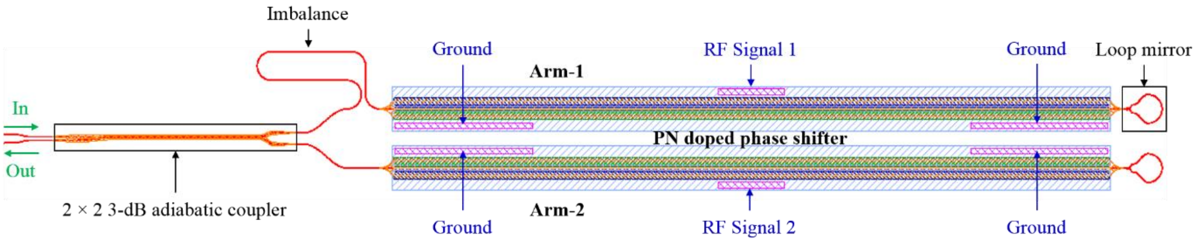

Fig. 5-17. Schematic layout of the dual-drive MIM. [47, 48]

Based on the same structure and geometry parameters, two MIMs are designed with the PN junctions shown in Figs. 5-13(a) and 5-13(b), respectively. The device with asymmetric 4 doping concentrations is named as MIM-1, and that with symmetric 6 doping concentrations is named as MIM-2. They were fabricated in the same MPW run at IME A*STAR. Figure 5-18 presents the micrographs of the fabricated devices. For each MIM, independent RF signals are applied on the two GSG pads, and all the ground pads are connected. The footprint of each device, including the bond pads, is 830 μm × 430 μm.

5.3.3 DC measurement

Figure 5-19 shows the measured DC transmission spectra of MIM-1 by applying reverse bias

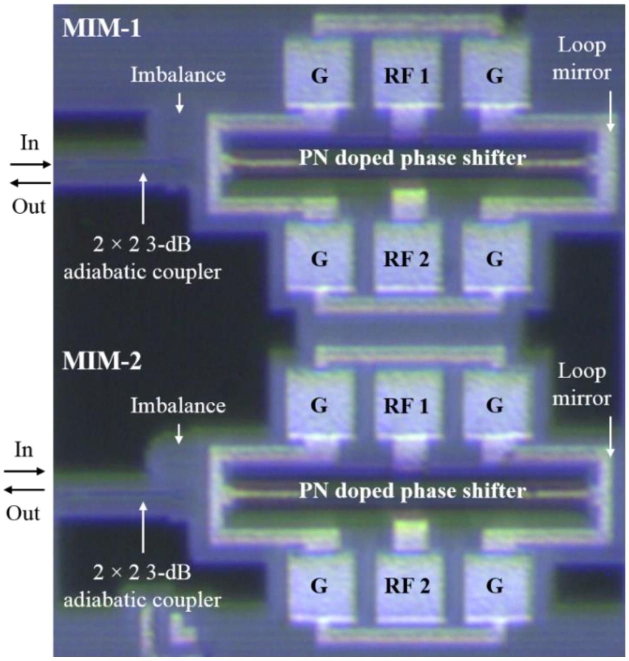

Fig. 5-18. Micrographs of the fabricated two MIMs. [47]

voltages on the two arms respectively. At 0 V bias, the total on-chip IL is 13.73 dB. Excluding the 9.85-dB IL of the GC pair and the 1.30-dB IL of the routing waveguide, the IL of MIM-1 is 2.58 dB. The measured FSR is 1.43 nm, corresponding to an imbalance of 400 μm. This is in good agreement with the design as the imbalance is 200 μm and light goes through the phase shifters twice.

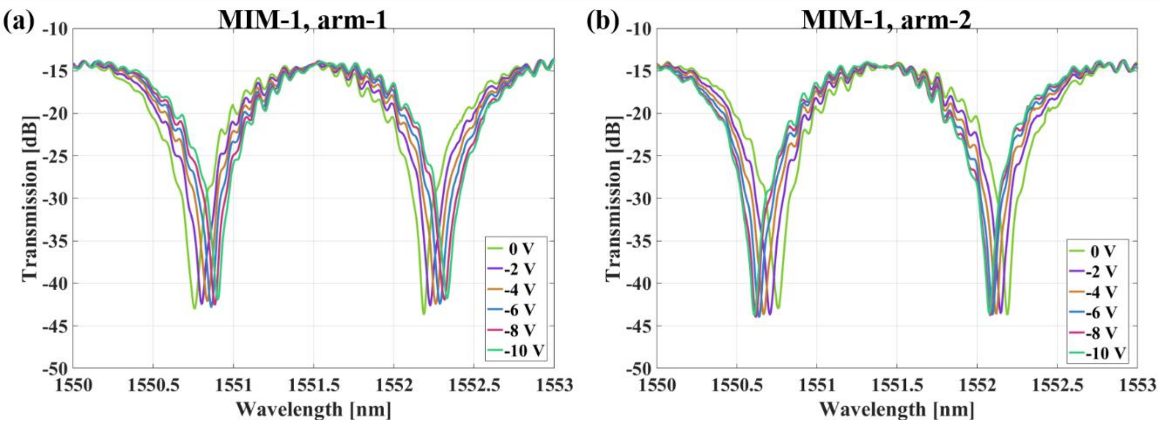

Fig. 5-19. Measured DC transmission spectra of MIM-1 by applying various reverse bias voltages on (a) arm-1 and (b) arm-2. [47]

The measured DC transmission spectra of MIM-2 are shown in Fig. 5-20. At 0 V bias, the total on-chip IL is 13.78 dB, and the device has an IL of 2.83 dB. It is larger than that of MIM-1 because the there is more optical scattering loss in the PN junctions of MIM-2. The resonant wavelengths of MIM-2 are also different from those of MIM-1. This is because the effective indices are different due to the different carrier distributions in the PN junctions. The measured FSR is 1.44 nm, which also corresponds to an effective imbalance of 400 μm, with a group index slightly smaller than that in MIM-1.

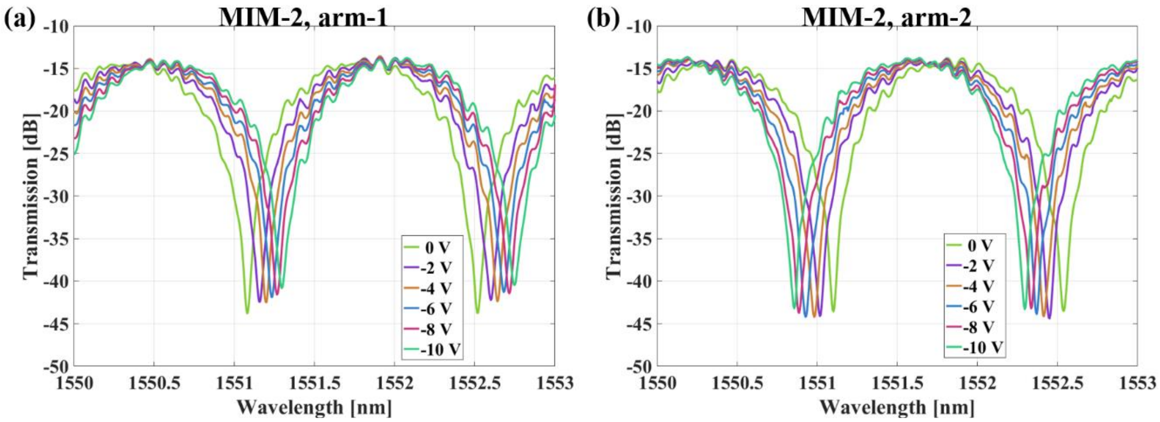

Fig. 5-20. Measured DC transmission spectra of MIM-2 by applying various reverse bias voltages on (a) arm-1 and (b) arm-2. [47]

Compared to those in Fig. 5-19, the resonance shifts in Fig. 5-20 are much larger, which is due to the larger effective index change by designing the PN junction in the rib waveguide to be symmetric, as shown in Fig. 5-15(a). The phase shifts and $V_\pi L_\pi$ are calculated using Eqs. 2.13 and 2.14, and are shown in Fig. 5-21. Under -2 V bias, the $V_\pi L_\pi$ of arm-1 and arm-2 on MIM-1 are 1.6 V-cm and1.4 V-cm, respectively. However, MIM-2 have $V_\pi L_\pi$ of 0.9 V-cm and 0.8 V-cm for the two arms at -2 V bias. Even though the two arms on each MIM are designed to be identical, the differences in the measurement are mainly due to the variations in the fabrication process. Due to the diminishing phase shift, the $V_\pi L_\pi$ becomes larger when at higher reverse bias voltages.

Like the operating principle analyzed in Section 5.2.2, PAM-4 signals are generated by applying independent binary RF signals on both arms of the MIM simultaneously and combining the optical signals modulated by each phase shifter. To achieve reasonable even spacings

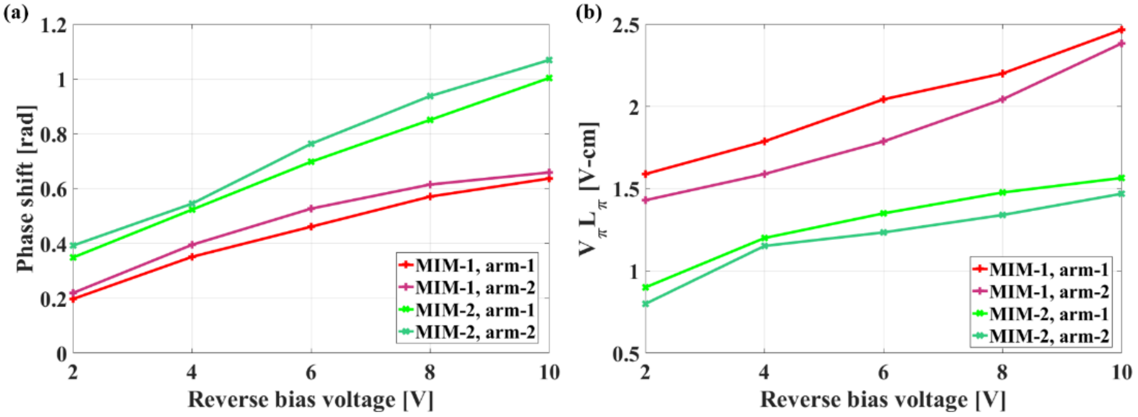

Fig. 5-21. Calculated (a) phase shifts and (b) $V_\pi L_\pi$ of each phase shifter on both MIMs. [47]

between adjacent levels of PAM-4 signals, DC transmission spectra of the device with reverse bias voltages applied on the RF pads of the two shifters are investigated. Figure 5-22 shows the measured output power with a 15.5-dBm input power from an external cavity laser (ECL). For fair comparison, the voltages applied on the two MIMs are the same, and the bias wavelengths are chosen for them to have similar output powers at their '11' levels. As shown in Fig. 5-21(a), the four output powers of MIM-1 are 0.328 mW, 0.303 mW, 0.280 mW and 0.257 mW. For MIM-2, the bias wavelength is chosen to be 1550.9 nm so that the four output power levels are 0.321 mW, 0.258 mW, 0.203 mW and 0.146 mW. Both MIMs can generate PAM-4 signals with reasonable spacings. But as the phase shifters of MIM-2 have larger modulation efficiencies, the average spacing is 0.058 mV for MIM-2, which is much larger than the 0.024 mW for MIM-1.

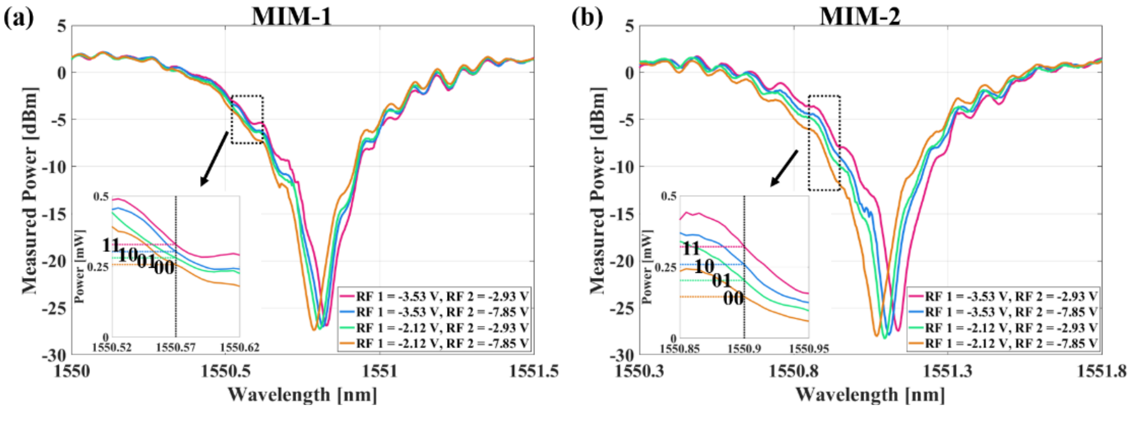

Fig. 5-22. Measured DC output spectra when applying reverse bias voltages on both phase shifters of (a) MIM-1 and (b) MIM-2. [47]

The four voltages listed in Fig. 5-22 are $V_{1,1}$ = -3.53 V, $V_{1,2}$ = -2.12 V, $V_{2,1}$ = -2.93 V, and $V_{2,2}$ = -7.85 V. Therefore, the bias voltages and peak-to-peak voltages of the driving RF signals are chosen to be V_{bias1} = -2.83 V, V_{pp1} = 1.41 V, V_{bias2} = -5.39 V and V_{pp2} = 4.92 V.

As shown in Figs. 5-19, 5-20 and 5-22, there are ripples in the measured transmission spectra of the two MIMs. This is because of a small portion of light may reflect back into the device from the output grating coupler. Together with the 2 × 2 3-dB adiabatic coupler in the MIM structure, a Fabry-Perot resonator is formed. Therefore, to avoid these ripples and to obtain four evenly spaced output powers, the two MIMs are biased at the wavelengths where their dynamic ILs are high, which are approximately 6.7 dB. Using RF signals with higher peak-to-peak voltages can decrease this loss, but a larger power consumption is needed as a trade-off.

5.3.4 Small-signal characterization

Under 0 V bias voltage at the modulation wavelengths shown in Fig. 5-22, i.e. 1550.57 nm for MIM-1 and 1550.9 nm for MIM-2, the EE S_{11} and EO S_{21} responses of each phase shifter on the two MIMs were measured Using an Agilent lightwave component analyzer after calibrating the cables and probes. Figure 5-23 shows the measured results normalized at 1.5 GHz. The 3-dB EE and EO bandwidths of the two MIMs are listed in Table 12.

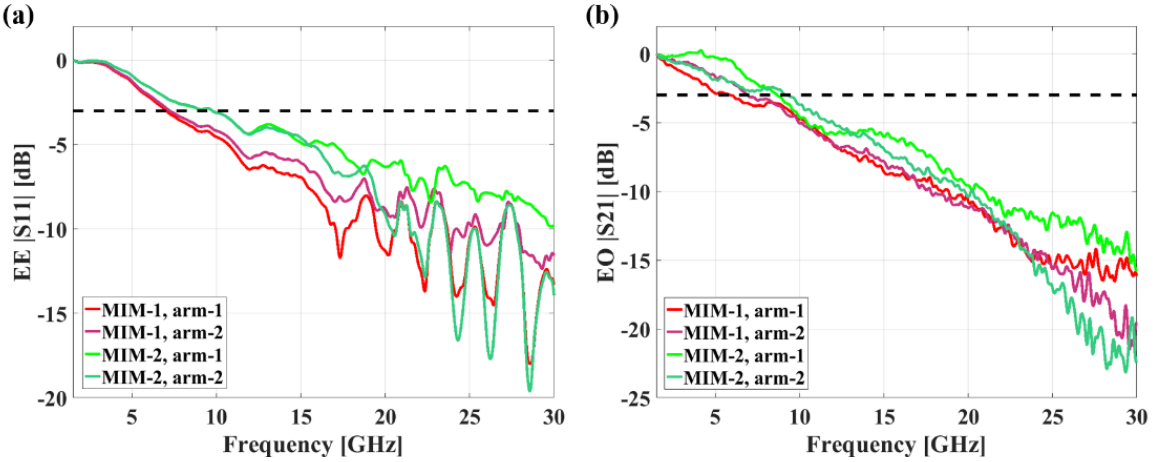

Fig. 5-23. Measured (a) EE S_{11} magnitudes and (b) EO S_{21} magnitudes under 0 V bias. [47]

As PN junction is the only difference in the two designs, the larger EE and EO bandwidths of the phase shifters on MIM-2 are due to the smaller junction resistances. However, the 3-dB EE bandwidths of MIM-2 are not twice of those of MIM-1 even though the PN junction resistances are reduced by more than 50%. This is because the PN junction capacitance and resistance are not the only elements in the small signal model of an MIM [19]. There are also other elements such as the capacitance of the contact pads [19]. Moreover, the measured responses of the phase shifters on each MIM are not identical. For example, as shown in Fig. 5-23(a), more attenuation and fluctuation are observed in the EE responses of arm-2 on MIM-2 at the frequencies above 20 GHz. This leads to the fact that its EO responses has larger attenuation at high frequencies, as shown in Fig. 5-23(b).

To further evaluate the performance of the devices at the operating bias points, their EO responses at -2.83 V bias for arm-1 and -5.39 V bias for arm-2 are investigated. The EO bandwidths are all larger than those at 0 V due to the reduction of junction capacitances at higher reverse bias voltages, as shown in Fig. 6-24 and listed in Table 12.

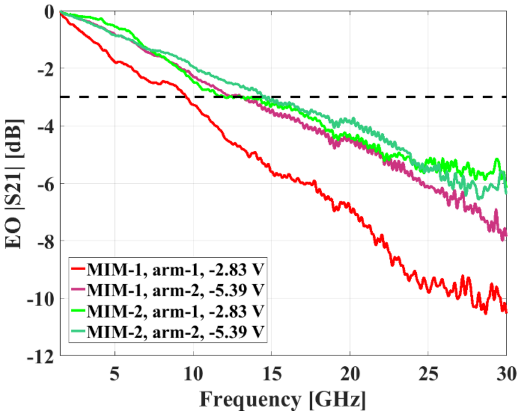

Fig. 5-24. Measured EO S_{21} magnitudes under -2.83 V for arm-1 and -5.39 V for arm-2. [47]

Table 12. Measured 3-dB EE and EO bandwidths. [47]

Device	Phase shifter	EE bandwidth (GHz)	EO bandwidth (GHz)
MIM-1	arm-1	7.0	5.9 (at 0 V) 9.5 (at - 2.83 V)
	arm-2	7.2	6.9 (at 0 V) 13.1 (at -5.39 V)
MIM-2	arm-1	9.8	8.7 (at 0 V) 12.0 (at -2.83 V)
	arm-2	9.8	9.3 (at 0 V) 14.4 (at -5.39 V)

5.3.5 PAM-4

Figure 5-25 illustrates the experimental-setup for the DAC-less and DSP-free PAM-4 signals generation and transmission using the dual-drive MIMs. Two 2^{31}-1 PRBS were generated by two independent channels of a BPG. As the required peak-to-peak voltages are V_{pp1} = 1.41 V and V_{pp2} = 4.92 V, 25-GHz RF amplifiers were applied to amplify the RF signals. Using 65-GHz bias tees, the required bias voltages V_{bias1} = -2.83 V and V_{bias2} = -5.39 V were combined with the RF signals, and then they were applied on the phase shifters by two 40-GHz GSG probes. An ECL at 15.5 dBm was used as light input. The input wavelengths are 1550.57 nm for MIM-1 and 1550.9 nm for MIM-2. After being coupled out from the device, the modulated PAM-4 optical signals were transmitted in B2B configuration or over 2 km of SSMF. Then they were amplified by an EDFA to have an average power of 3 dBm. A DCA was used to obtain the eye diagrams and estimate the BERs based on the same method described in Section 5.2.4. The filter for approximately 43 Gb/s was turned on in the optical module of the DCA.

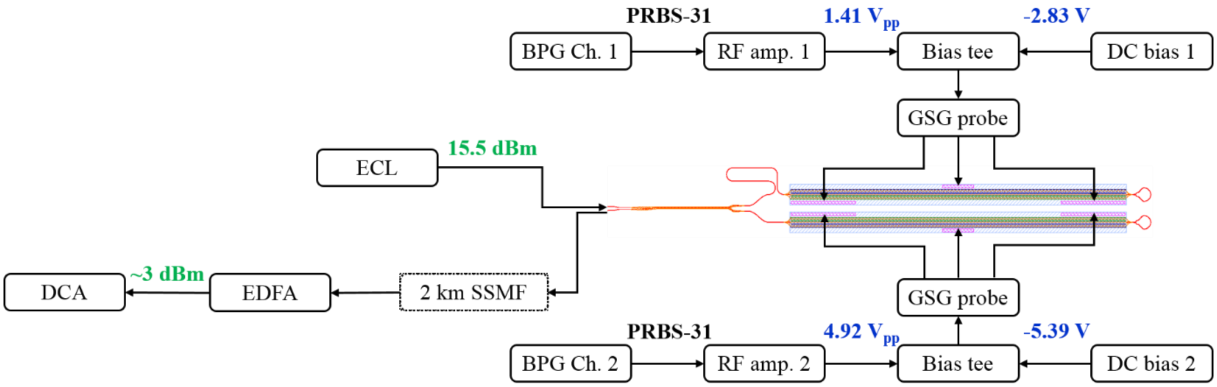

Fig. 5-25. Experimental setup of DAC-less DSP-free PAM-4 using the dual-drive MIM. [47]

First, the performance of MIM-1 is investigated. Same to those presented in Section 5.2.4, the BERs are estimated using vertical histograms of the captured eye diagrams based on the assumption that the noise has a Gaussian distribution [124, 125]. As shown in Fig. 5-26, the estimated BERs from 40 Gb/s to 60 Gb/s are all larger than the KP4 FEC threshold, even in the B2B transmission. At 50 Gb/s in B2B configuration, and at 40 Gb/s after transmission over 2 km of SSMF, the estimated BERs are below the HD FEC threshold.

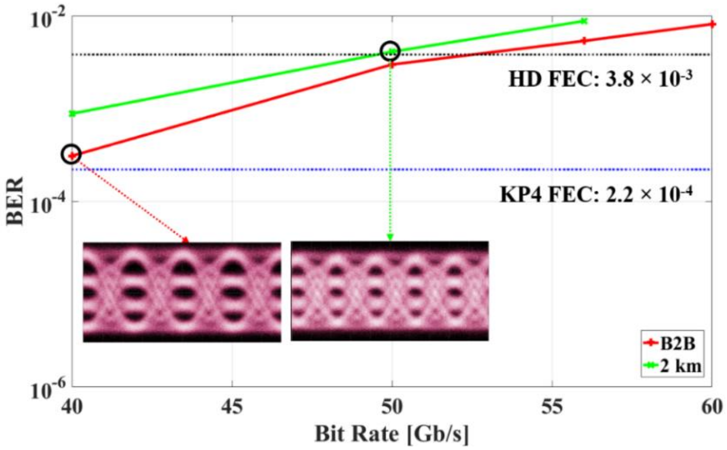

Fig. 5-26. PAM-4 BERs and eye diagrams of MIM-1. [47]

As shown in Fig. 5-27(a), MIM-2 has clearly open eye diagrams at 40 Gb/s in B2B configuration and at 50 Gb/s after transmission over 2 km of SSMF. These two eye diagrams are much better those shown in Fig. 5-26. After 2 km of SSMF transmission, the estimated BER at 50 Gb/s is below the KP4 FEC threshold, and that at 56 Gb/s is below the HD FEC threshold. The measured histograms of every level on the 56 Gb/s eye diagram after 2 km of SSMF transmission are shown in Fig. 5-28. Figures 5-27(b) and 5-27(c) are obtained by turning on only of the RF signals on the phase shifter at a time, and they are at 28 Gbaud after 2 km of SSMF transmission. Their OMAs are different, which are 0.68 mW by arm-1 and 1.20 mW by arm-2.

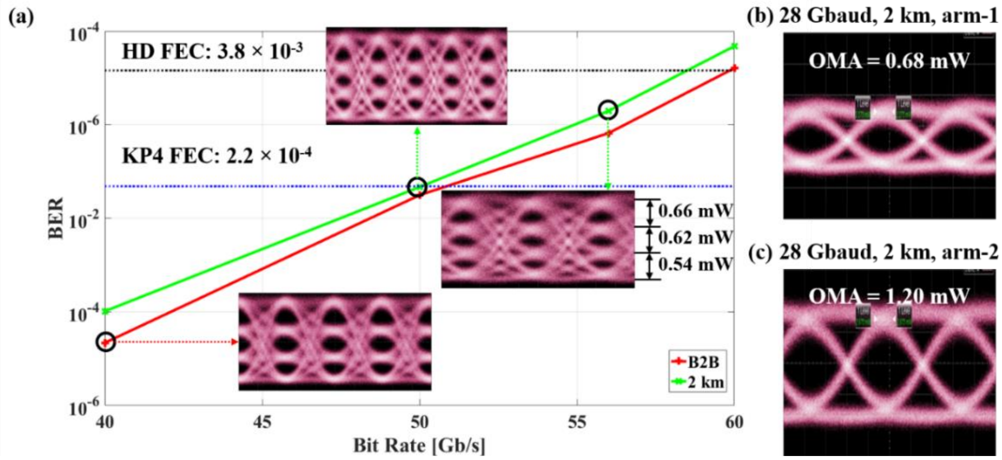

Fig. 5-27. (a) PAM-4 BERs and eye diagrams of MIM-2, 28-Gbaud eye diagrams by turning on the RF signals on (a) arm-1 and (b) arm-2 after 2 km of SSMF transmission. [47, 48]

When combining the binary optical signals modulated by each phase shifter, the device generates PAM-4 signals with reasonable even spacings. The four power levels of the measured 56 Gb/s PAM-4 eye diagram after 2 km of SSMF transmission further prove the feasibility of this operating principle.

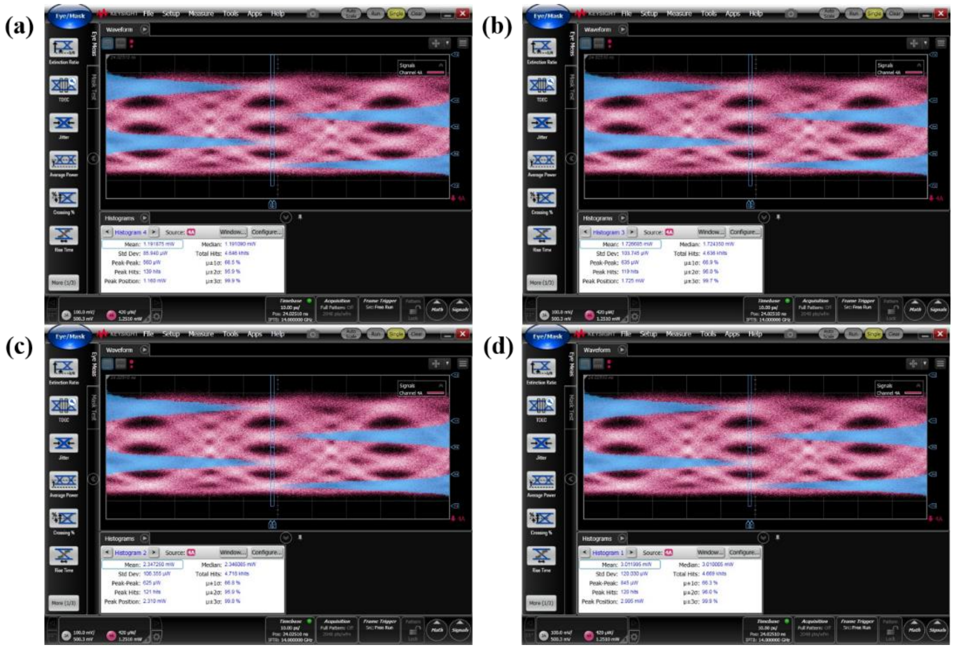

Fig. 5-28. Measured histograms of the 56 Gb/s eye diagrams after 2 km transmission.

As MIM-2 is designed using the PN junctions with 6 symmetric doping concentrations, it has better modulation efficiency and slightly larger EO bandwidths. Therefore, the PAM-4 transmission performance of MIM-2 is better than that of MIM-1.

5.4 Conclusion

In this chapter, we present a dual-drive operation of a RAMZI modulator and an MIM for DAC-less and DSP-free PAM-4 signals generation and short-reach transmission. The operating principle is elaborated by system-level simulation and the measurement DC transmission spectra. The bias wavelength and the parameters of the driving RF signals are carefully chosen to achieve PAM-4 with reasonable even spacings.

The RAMZI modulator achieves PAM-4 transmission at 40 Gb/s over 5 km of SSMF and at 50 Gb/s over 2 km of SSMF, with the estimated BERs below the HD FEC threshold [46]. As the two MRMs are designed to be identical but biased differently, the PAM-4 performance of the RAMZI modulator can be improved by applying better MRM designs in the working conditions.

For the dual-drive MIM, two devices with different PN junction designs are compared. We show by simulation that the PN junction with symmetric 6 doping concentrations has better modulation efficiency and smaller junction resistance than that with asymmetric 4 doping concentrations [47]. These advantages are also confirmed by the measured DC transmission spectra and small-signal modulation performances of two MIMs. The dual-drive MIM with symmetric 6 doping concentrations achieves 56 Gb/s PAM-4 transmission over 2 km of SSMF with estimated BER below the HD FEC threshold [47, 48].

Chapter 6
Conclusion

6.1 Summary

As the intra-data center traffic is increasing tremendously in recent years, high-speed low-cost modulators are in urgent need to fulfill this demand, and thus they have attracted immense research interest. For the fabrication platform of the integrated modulators, silicon photonics offers a promising solution as it is CMOS-compatible and it has a low substrate cost for large volume integration. Various SiP devices, such as modulators [6, 7], photodetectors [8, 9] and passive components [10-12], have been reported, which further prove the suitability of silicon photonics for the data center interconnects. Regarding the modulation formats, higher order intensity modulation is favored. Because there is no local oscillator or complicated DSP implemented in the IM/DD systems, they are cost-saving and thus more suitable than coherent transmission systems for intra-data center applications. Though OOK has been selected for the 40G and 100G Ethernet applications, but it cannot fulfill the bandwidth requirement for the 400G Ethernet. PAM-4 is a good choice among all the intensity modulation formats when considering both the spectral efficiency and the required SNR, and it has been accepted for the next generation 400G Ethernet. Currently, PAM-4 short-reach transmission based on SiP modulators, such as TWMZMs [6, 7, 32, 33] and MRMs [18, 90, 91], have been reported.

In this thesis, three operating principles of PAM-4 optical signals generation using two kinds of SiP modulators are introduced and investigated. It should be noted that all the modulators are polarization dependent and only TE polarized light in modulated. First, using the push-pull operation of dual parallel MRMs, low-chirp modulation is realized. Without using any CD compensation method, PAM-4 transmissions over 1 km of SSMF at 92 Gb/s, over 2 km of SSMF at 80 Gb/s and over 20 km of SSMF at 40 Gb/s are achieved. Second, by assisting a single MRM in a balanced MZI, the static ER is much larger than that of the single MRM. Moreover, by assisting the other MZI arm with a passive MRR and overlapping the resonances of the MRM with the MRR, the ERs and OMAs are further enhanced. Based on this operating principle, 80 Gb/s PAM-4 over 2 km of SSMF transmission is successfully demonstrated. Third, the dual-drive operation is proposed for DAC-less and DSP-free PAM-4 signals generation, which reduces the power consumption in the transmission link. Using the RAMZI modulator, PAM-4 transmissions at 40 Gb/s over 5 km of SSMF and at 50 Gb/s over 2 km of SSMF are achieved. Using the MIM, 56 Gb/s PAM-4 transmission over 2 km of SSMF is presented. All the measured or estimated BERs based on these three operating principles are below the HD FEC threshold of 3.8×10^{-3}. To conclude, the PAM-4 transmission performances by applying the three operating principles on the two SiP modulators are summarized in Table 13. Compared to the performance of SiP MRMs, TWMZMs and those based on a combination of these two structures, as listed in Table 2, 3 and 5 respectively, the modulators demonstrated in this thesis are successful in high speed PAM-4 transmission with compact footprint and novel operating principles.

Table 13. PAM-4 transmission performances by applying the three operating principles on the two SiP modulators.

Operating principle	Advantage	SiP modulator	Bit rate [Gb/s]	Transmission [km]
Push-pull	Low chirp	Dual parallel MRMs	92	1
			80	2
			40	20
Resonances overlap	Large OMA and ER	MRM + MRR + MZI	80	2
Dual-drive	DAC-less, DSP-free and low power consumption	RAMZI modulator	40	5
			50	2
		MIM	56	2

In Chapter 1, the current challenge on the intra-data center traffic and one of the most promising solutions, PAM-4 short reach transmission based on SiP modulators, were introduced. In addition, an overview of various SiP modulator structures was presented to elaborate on the motivations of this thesis. Afterwards, the thesis organization and the author’s original contribution were summarized.

In Chapter 2, the fundamentals of SiP modulators were reviewed. First, the plasma dispersion effect, which is the basic of modulation in the PN doped silicon waveguides, was presented. Afterwards, the designs of silicon waveguide, lateral PN junctions and heaters were studied and analyzed using simulation. Then two widely used SiP modulators, MRMs and TWMZMs, were reviewed, with a focus on their device structures, modulation principles, design methods and FOMs. Other modulator structures were also briefly discussed.

In Chapter 3, the push-pull operation of dual parallel MRMs was demonstrated. After the device design and fabrication method being presented, the operating principle to achieve low-chirp PAM-4 signals generation was elaborated using both system-level modulation and chirp measurement. Afterwards, the device characterization was reported, including the measured DC transmission spectra to show its modulation efficiency, optical bandwidth and other FOMs, as well as the small-signal modulation to analyze its EE and EO bandwidths. Then the OOK modulation using the push-pull operation of the dual parallel MRMs was compared with that of the single MRM, further proving the low-chirp advantage of this operating principle. Finally, PAM-4 transmission, achieving the highest bit rate compared to the previously published SiP MRM-based PAM-4 results [18, 90, 91], was presented.

In Chapter 4, the resonances overlap operation of an MRM with an MRR was studied. First, two device designs were presented for operation in three different configurations. Afterwards, the operating principle was analyzed in two steps. First, the OMA and ER are improved by assisting a single MRM in a balanced MZI. Second, these two FOMs are further enhanced by overlapping the resonances of the MRM with a passive MRR on the other MZI arm. Numerical analysis, simulation results and measured DC transmission spectra were all demonstrated to elaborate on the operating principle. In addition, OOK modulation and PAM-4 transmission were reported and compared to further prove the advantages of the resonances overlap operation. In addition, other resonances overlap conditions were presented to complete the analysis.

In Chapter 5, the dual-drive operation of a RAMZI modulator and an MIM was demonstrated for DAC-less and DSP-free PAM-4 signals generation. For the RAMZI modulator, the device design and fabrication were shown at first. Then the operating principle was explained by system-level simulations of both the individual MRMs and the whole device. The measured DC transmission spectra were presented to show the measured modulation efficiencies and to decide the parameters of the driving RF signals for PAM-4 signals generation with reasonable even spacings. The small-signal modulation of the device at the working conditions were also reported. Afterwards, PAM-4 transmission results were demonstrated and the BER estimation methods were also elaborated. For the MIM, two PN junction designs, one with asymmetric 4 doping concentrations and the other with symmetric 6 doping concentrations, were proposed and compared by simulation. The structure and fabrication of the MIMs designed with these two different PN junctions were then presented. Their DC characterization, small-signal modulation and PAM-4 transmission results were reported and compared one by one, showing the device with symmetric 6 doping concentrations achieved better modulation efficiencies, larger EO bandwidths and PAM-4 at higher bit rates.

6.2 Future work

As reviewed in Chapter 2, in addition to MRMs, there are various SiP modulators that can achieve high-speed modulation. Because MRM is very sensitive to temperature change, modulating MRMs using these operating principles needs a temperature control feedback loop. This largely increases the power consumption [93]. One future work is that we can replace the MRMs in the balanced MZI to other modulator structures, such as GeSi EAM, BGM and TWMZM. For the new structures, the push-pull operation can be applied to achieve low-chirp modulation, and this has been reported using TWMZMs [33]. The resonances overlap operation can also be used to obtain better modulation FOMs in the new structures with TWMZM or BGM. It should be noted that GeSi EAM is not a resonator-based modulator, therefore this operating principle cannot be applied on it. The dual-drive operation for DAC-less and DSP-free PAM-4 generation has been achieved based on dual parallel TWMZMs [33] and dual parallel GeSi EAMs [39]. By replacing the MRMs with BGMs, this operating principle is still feasible to achieve PAM-4 signals generation without the use of DAC or DSP.

PAM-4 transmission of 8λ × 50G over 2 km of SSMF (400GBASE-FR8) and 4λ × 100G over 500 m of SSMF (400GBASE-DR4) have both been accepted for the next-generation 400G Ethernet. Therefore, achieving single wavelength 100 Gb/s PAM-4 is also an important future work. By polishing the designs of the PN junctions and geometry parameters of the device, the modulation bit rate of the MRMs or the phase shifters of the MIM will be increased. Then by applying the three operating principles, the modulation performance can be further improved to achieve a higher bit rate for PAM-4 transmission.

By using both the TE and transverse magnetic (TM) polarizations, the modulation bit rate can be further doubled. In this case, polarization independent GCs [127, 128] should be applied and two groups of modulators should be designed for both in-phase and quadrature modulation [129]. Single wavelength multi-mode modulation implementing several independent modulators [130] is also practical in increasing the transmission bit rate manyfold.

To realize even higher bit rate, e.g. 400 Gb/s per wavelength, for the next-generation 400G Ethernet, 800G Ethernet and even 1.6T Ethernet, intensity modulation formats are no longer suitable because their achievable bit rates are limited by the EO bandwidths of the opto-electronic devices. Therefore, the modulated spectral efficiency should be improved to achieve a higher bit rate. One possible solution is to apply even higher order intensity modulation format, such as eight-level pulse amplitude modulation (PAM-8). But the required SNR will be another limitation. Therefore, coherent modulation formats are favored in this case [131, 132]. By modulating the dual parallel MRMs with independent 4-level RF signals and applying a DC voltage on the MZI heater to achieve a phase difference of $\pi/2$ between the two arms, 16-state quadrature amplitude modulation (16-QAM) can be achieved. In addition, by adding a heater on one arm of the dual-drive MIM and using the same method, coherent modulation can also be realized. In addition, advanced detection methods, such as Stokes vector direct detection [133] and Kramers-Kronig detection [134], can be applied in coherent transmission systems to further increase the achievable bit rate.

Overall, SiP modulators have attracted immense research interest and developed rapidly in the past decade. Currently, they have also been applied in mature commercial products [59-62]. We believe in the future, the transmission performances of SiP modulators will be further improved and they will be more influential in the next-generation high-speed Ethernet applications.

References

[1] Cisco Corp., Cisco Global Cloud Index: Forecast and Methodology, 2015-2020, http://www.cisco.com, 2016.

[2] D. A. B. Miller, "Device requirements for optical interconnects to CMOS silicon chips," in *Photonics in Switching* (Optical Society of America, 2010), paper PMB3.

[3] J. E. Bowers and A. Y. Liu, "A comparison of four approaches to photonic integration," in *Optical Fiber Communication Conference* (Optical Society of America, 2017), paper M2B.4.

[4] J. E. Bowers, J. T. Bovington, A. Y. Liu, and A. C. Gossard, "A path to 300 mm hybrid silicon photonic integrated circuits," in *Optical Fiber Communication Conference* (Optical Society of America, 2014), paper Th1C.1.

[5] M. Hochberg, N. C. Harris, R. Ding, Y. Zhang, A. Novack, Z. Xuan, and T. Baehr-Jones, "Silicon photonics: the next fabless semiconductor industry," IEEE Solid State Circuits Mag. **5**(1), 44-58 (2013).

[6] D. Patel, S. Ghosh, M. Chagnon, A. Samani, V. Veerasubramanian, M. Osman, and D. V. Plant, "Design, analysis, and transmission system performance of a 41 GHz silicon photonic modulator," Opt. Express **23**(11), 14263-14287 (2015).

[7] A. Samani, M. Chagnon, D. Patel, V. Veerasubramanian, S. Ghosh, M. Osman, Q. Zhong and D. V. Plant, "A low-voltage 35-GHz silicon photonic modulator-enabled 112-Gb/s transmission system", IEEE Photon. J. **7**(3), 7901413 (2015).

[8] L. Vivien, A. Polzer, D. Marris-Morini, J. Osmond, J. M. Hartmann, P. Crozat, E. Cassan, C. Kopp, H. Zimmerman, and J. M. Fédéli, "Zero-bias 40Gbit/s germanium waveguide photodetector on silicon," Opt. Express **20**(2), 1096-1101(2012).

[9] A. Novack, M. Gould, Y. Yang, Z. Xuan, M. Streshinsky, Y. Liu, G. Capellini, A. E.-J. Lim, G.-Q. Lo, T. Baehr-Jones, and M. Hochberg, "Germanium photodetector with 60 GHz bandwidth using inductive gain peaking," Opt. Express **21**(23), 28387-28393 (2013).

[10] D. Dai, Z. Wang, J. Peters, and J. E. Bowers, “Compact polarization beam splitter using an asymmetrical Mach-Zehnder interferometer based on silicon-on-insulator waveguides,” IEEE Photon. Technol. Lett. **24**(8), 673-675 (2012).

[11] D. Dai, J. Wang and Y. Shi, “Silicon mode (de)multiplexer enabling high capacity photonic networks-on-chip with a single-wavelength-carrier light,” Opt. Lett. **38**(9), 1422-1424 (2013).

[12] Q. Zhong, V. Veerasubramanian, Y. Wang, W. Shi, D. Patel, S. Ghosh, A. Samani, L. Chrostowski, R. Bojko, and D. V. Plant, “Focusing-curved subwavelength grating couplers for ultra-broadband silicon photonics optical interfaces,” Opt. Express **22**(15), 18224-18231 (2014).

[13] E. El-Fiky, M. Chagnon, M. Sowailem, A. Samani, M. Morsy-Osman, and D. V. Plant, “168-Gb/s single carrier PAM4 transmission for intra-data center optical interconnects,” IEEE Photonics Technol. Lett. **29**(3), 314-317 (2017).

[14] M. Y. S. Sowailem, T. M. Hoang, M. Morsy-Osman, M. Chagnon, M. Qiu, S. Paquet, C. Paquet, I. Woods, Q. Zhuge, O. Liboiron-Ladouceur, and D. V. Plant, “770-Gb/s PDM-32QAM coherent transmission using InP dual polarization IQ modulator,” IEEE Photonics Technol. Lett. **29**(5), 442-445 (2017).

[15] IEEE P802.3bs 40GbE and 100GbE Task Force, http://www.ieee802.org/3/ba/index.html.

[16] IEEE P802.3bs 400GbE Task Force, http://www.ieee802.org/3/bs/index.html.

[17] X. Xiao, X. Li, H. Xu, Y. Hu, K. Xiong, Z. Li, T. Chu, J. Yu and Y. Yu, “44-Gb/s silicon microring modulators based on zigzag PN junctions,” IEEE Photonics Technol. Lett. **24**(19), 1712-1714 (2012).

[18] R. Dubé-Demers, S. LaRochelle, and W. Shi, “Ultrafast pulse-amplitude modulation with a femtojoule silicon photonic modulator,” Optica **3**(6), 622-627 (2016).

[19] D. Patel, V. Veerasubramanian, S. Ghosh, A. Samani, Q. Zhong, and D. V. Plant, “High-speed compact silicon photonic Michelson interferometric modulator,” Opt. Express **22**(22), 26788-26802 (2014).

[20] K. Bédard, A. D. Simard, B. Fillion, Y. Painchaud, L. A. Rusch, and S. LaRochelle, “Dual phase-shift Bragg grating silicon photonic modulator operating up to 60 Gb/s,” Opt. Express **24**(3), 2413-2419 (2016).

[21] S. A. Srinivasan, M. Pantouvaki, S. Gupta, H. T. Chen, P. Verheyen, G. Lepage, G. Roelkens,

K. Saraswat, D. V. Thourhout, P. Absil, and J. V. Campenhout, “56 Gb/s germanium waveguide electro-absorption modulator,” J. Lightw. Technol. **34**(2), 419-424 (2016).

[22] J. Verbist, M. Verplaetse, S. A. Srivinasan, P. De Heyn, T. De Keulenaer, R. Peirco, R. Vaernewyck, A. Vyncke, P. Absil, G. Torfs, X. Yin, G. Roelkens, J. V. Campenhout, and J. Bauwelinck, “First real-time 100-Gb/s NRZ-OOK transmission over 2 km with a silicon photonic electro-absorption modulator,” in *Optical Fiber Communication Conference* (Optical Society of America, 2017), paper Th5C.4.

[23] M. Webster, P. Gothoskar, V. Patel, D. Piede, S. Anderson, R. Tummidi, D. Adams, C. Appel, P. Metz, S. Sunder, B. Dama, and K. Shastri, “An efficient MOS-capacitor based silicon modulator and CMOS drivers for optical transmitters,” in *Proceedings of IEEE 11th International Conference on Group IV Photonics* (IEEE, 2014), paper WB1.

[24] M. Nedeljkovic, R. Soref, and G. Z. Mashanovich, “Predictions of free-carrier electroabsorption and electrorefraction in germanium,” IEEE Photon. J. **7**(3), 2600214 (2015).

[25] S. Akiyama, T. Kurahashi, K. Morito, T. Yamamoto, T. Usuki, and S. Nomura, “Cascaded-ring-resonator-loaded Mach-Zehnder modulator for enhanced modulation efficiency in wide optical bandwidth,” Opt. Express **20**(15), 16321-16338 (2012).

[26] B. Guha, K. Preston, and M. Lipson, “Athermal silicon microring electro-optic modulator,” Opt. Lett. **37**(12), 2253-2255 (2012).

[27] J. Cardenas, P. A. Morton, J. B. Khurgin, A. Griffith, C. B. Poitras, K. Preston, and M. Lipson, “Linearized silicon modulator based on a ring assisted Mach Zehnder interferometer,” Opt. Express **21**(19), 22549-22557 (2013).

[28] D. M. Gill, S. S. Patel, M. Rasras, K.-Y. Tu, A. E. White, Y.-K. Chen, A. Pomerene, D. Carothers, R. L. Kamocsai, C. M. Hill, and J. Beattie, “CMOS-compatible Si-ring-assisted Mach-Zehnder interferometer with internal bandwidth equalization,” IEEE J. Sel. Top. Quantum Electron. **16**(1), 45-52 (2010).

[29] C.-M. Chang, G. de Valicourt, S. Chandrasekhar, and P. Dong, “Differential microring modulators for intensity and phase modulation: theory and experiments,” J. Lightw. Technol. **35**(15), 3116-3124 (2017).

[30] P. Dong, C. Xie, L. L. Buhl, and Y. K. Chen, “Silicon microring modulators for advanced

modulation formats," in *Optical Fiber Communication Conference* (Optical Society of America, 2013), paper OW4J.2.

[31] M. S. Hai, M. M. P. Fard, and O. Liboiron-Ladouceur, "A ring-based 25 Gb/s DAC-less PAM-4 modulator," IEEE J. Sel. Top. Quantum Electron. **22**(6), 3400308 (2016).

[32] D. Patel, A. Samani, V. Veerasubramanian, S. Ghosh, and D. V. Plant, "Silicon photonic segmented modulator-based electro-optic DAC for 100 Gb/s PAM-4 generation," IEEE Photonics Technol. Lett. **27**(23), 2433-2436 (2015).

[33] A. Samani, V. Veerasubramanian, E. El-Fiky, D. Patel, and D. V. Plant, "A silicon photonic PAM-4 modulator based on dual-parallel Mach-Zehnder interferometers," IEEE Photonics J. **8**(1), 7800610 (2016).

[34] L. Zheng, J. Ding, S. Shao, L. Zhang, and L. Yang, "Silicon PAM-4 optical modulator driven by two binary electrical signals with different peak-to-peak voltages," Opt. Lett. **42**(11), 2213-2216 (2017).

[35] S. Shao, J. Ding, L. Zheng, K. Zou, L. Zhang, F. Zhang, and L. Yang, "Optical PAM-4 signal generation using a silicon Mach-Zehnder optical modulator," Opt. Express **25**(19), 23003-23013 (2017).

[36] O. Dubray, M. A. Seyedi, C. H. Chen, B. Charbonnier, A. Descos, M. Fiorentino, R. G. Beausoleil, and S. Menezo, "30Gbit/s PAM-4 transmission by modulating a dual silicon ring resonator modulator," in *Proceedings of IEEE Optical Interconnects Conference* (IEEE, 2016), pp. 6-7.

[37] A. Roshan-Zamir, B. Wang, S. Telaprolu, K. Yu, C. Li, M. A. Seyedi, M. Fiorentino, R. Beausoleil, and S. Palermo, "A two-segmented optical DAC 40 Gb/s PAM4 silicon microring resonator modulator transmitter in 65nm CMOS," in *Proceedings of IEEE Optical Interconnects Conference* (IEEE, 2017), pp. 5-6.

[38] M. Webster, K. Lakshmikumar, C. Appel, C. Muzio, B. Dama, and K. Shastri, "Low-power MOS-capacitor based silicon photonic modulators and CMOS drivers," in *Optical Fiber Communication Conference* (Optical Society of America, 2015), paper W4H.3.

[39] J. Verbist, J. Lamprecht, M. Verplaetse, J. Van Kerrebrouck, S. A. Srinivasan, P. De Heyn, T. De Keulenaer, X. Yin, J. V. Campenhout, G. Roelkens, and J. Bauwelinck, "DAC-less and

DSP-free PAM-4 transmitter at 112 Gb/s with two parallel GeSi electro-absorption modulators," in *Proceedings of European Conference and Exposition on Optical Communications* (2017), paper. Th.PDP.C.5.

[40] R. Dubé-Demers, S. LaRochelle, and W. Shi, "Low-power DAC-less PAM-4 transmitter using a cascaded microring modulator," Opt. Lett. **41**(22), 5369-5372 (2016).

[41] R. Li, D. Patel, E. El-Fiky, A. Samani, Z. Xing, M. Morsy-Osman, and D. V. Plant, "High-speed low-chirp PAM-4 transmission based on push-pull silicon photonic microring modulators," Opt. Express **25**(12), 13222-13229 (2017).

[42] R. Li, D. Patel, E. El-Fiky, A. Samani, Z. Xing, L. Xu, and D. V. Plant, "A C-band push-pull dual-ring silicon photonic modulator for 20 km SSMF transmission without CD compensation," in *Conference on Lasers and Electro-optics* (Optical Society of America, 2017), paper SM2O.3.

[43] R. Li, D. Patel, A. Samani, E. El-Fiky, Y. Wang, Z. Xing, and D. V. Plant, "Analysis and experimental study of a silicon photonic single MRM-assisted MZI PAM-4 modulator," IEEE Photonics J. **9**(6), 4900607 (2017).

[44] R. Li, A. Samani, E. El-Fiky, D. Patel, Q. Zhong, and D. V. Plant, "56-Gbps OOK transmission using silicon microring assisted Mach-Zehnder interferometer," in *Conference on Lasers and Electro-optics* (Optical Society of America, 2016), paper STu4G.4.

[45] R. Li, D. Patel, A. Samani, E. El-Fiky, Z. Xing, M. Sowailem, Q. Zhong and D. V. Plant, "An 80 Gb/s silicon photonic modulator based on the principle of overlapped resonances," IEEE Photonics J. **9**(3), 4900311 (2017).

[46] R. Li, D. Patel, A. Samani, E. El-Fiky, Z. Xing, M. Morsy-Osman, and D. V. Plant, "Silicon photonic ring-assisted MZI for 50 Gb/s DAC-less and DSP-free PAM-4 transmission," IEEE Photonics Technol. Lett. **29**(12), 1046-1049 (2017).

[47] R. Li, D. Patel, E. El-Fiky, A. Samani, Z. Xing, and D. V. Plant, "Silicon photonic dual-drive MIM based 56 Gb/s DAC-less and DSP-free PAM-4 transmission," Opt. Express **26**(5), 5395-5407 (2018).

[48] R. Li, D. Patel, E. El-Fiky, A. Samani, Z. Xing, Y. Wang, and D. V. Plant, "56 Gb/s DAC-less and DSP-free PAM-4 using a silicon photonic dual-drive Michelson interferometric

modulator," in *Optical Fiber Communication Conference* (Optical Society of America, 2018), paper W4D.1.

[49] R. A. Soref, "All-silicon active and passive guided-wave components for λ = 1.3 and 1.6 μm," IEEE J. Quantum Electron. **22**(6), 873-879 (1986).

[50] R. A. Soref and B. R. Bennett, "Electrooptical effects in silicon," IEEE J. Quantum Electron. **23**(1), 123-129 (1987).

[51] R. A. Soref, "Silicon-based optoelectronic," Proc. IEEE **81**(12), 1687-1706(1993).

[52] R. A. Soref, J. Schmidtchen, and K. Petermann, "Large single-mode rib waveguides in GeSi-Si and Si-on-SiO_2," IEEE J. Quantum Electron. **27**(8), 1971-1974 (1991).

[53] U. Fischer, T. Zinke, and K. Petermann, "Integrated optical waveguide switches in SOI," in *Proceedings of 1995 IEEE International SOI Conference* (IEEE, 1995), pp. 141-142.

[54] P. D. Trinh, S. Yegnanarayanan, and B. Jalali, "Integrated optical directional couplers in silicon-on-insulator," Electron. Lett. **31**(24), 2097-2098 (1995).

[55] C. Z. Zhao, G. Z. Li, E. K. Liu, Y. Gao, and X. D. Liu, "Silicon on insulator Mach–Zehnder waveguide interferometers operating at 1.3 μm," Appl. Phys. Lett. **67**(17), 2448–2449(1995).

[56] P. D. Trinh, S. Yegnanarayanan, F. Coppinger, and B. Jalali, "Silicon-on-insulator (SOI) phased-array wavelength multi/demultiplexer with extremely low-polarization sensitivity," IEEE Photonics Technol. Lett. **9**(7), 940-942 (1997).

[57] A. Liu, R. Jones, L. Liao, D. Samara-Rubio, D. Rubin, O. Cohen, R. Nicolaescu, and M. Paniccia, "A high-speed silicon optical modulator based on a metal-oxide-semiconductor capacitor," Nature **427**, 615-618(2004).

[58] J. M. Shainline, J. S. Orcutt, M. T. Wade, K. Nammari, B. Moss, M. Georgas, C. Sun, R. J. Ram, V. Stojanović, and M. A. Popović, "Depletion-mode carrier-plasma optical modulator in zero-change advanced CMOS," Opt. Lett. 38(15), 2657-2659 (2013).

[59] Intel, Intel® Silicon Photonics 100G PSM4 Optical Transceiver Brief, https://www.intel.com/content/www/us/en/architecture-and-technology/silicon-photonics/optical-transceiver-100g-psm4-qsfp28-brief.html.

[60] Luxtera, Luxtera delivers world's first single chip 100Gbps integrated opto-electronic transceiver, http://www.luxtera.com.

[61] Ranovus, Ranovus announces availability of world's first 200G CFP2 direct detect optical transceiver to enable 38.4 terabits per data center interconnect rack, http://ranovus.com.

[62] Mellanox, Mellanox doubles silicon photonics ethernet transceiver speeds to 200Gb/s, http://ir.mellanox.com.

[63] R. A. Soref, and B. R. Bennett, "Kramers-Kronig analysis of electro-optical switching in silicon," Proc. SPIE **0704**, 32-37(1987).

[64] G. T. Reed, G. Mashanovich, F. Y. Gardes, and D. J. Thomson, "Silicon optical modulators," Nature Photonics **4**, 518-526(2010).

[65] M. Nedeljkovic, R. Soref, and G. Z. Mashanovich, "Free-carrier electrorefraction and electroabsorption modulation predictions for silicon over the 1-14-μm infrared wavelength range," IEEE Photonics J. **3**(6), 1171-1180 (2011).

[66] R. Ding, Y. Liu, Q. Li, Y. Yang, Y. Ma, K. Padmaraju, A. E.-J. Lim, G.-Q. Lo, K. Bergman, T. Baehr-Jones, and M. Hochberg, "Design and characterization of a 30-GHz bandwidth low-power silicon travelling-wave modulator," Opt. Commun. **321**, 124–133 (2014).

[67] R. F. Pierret, *Semiconductor Fundamentals* (Addison-Wesley, 1988).

[68] S. J. Spector, M. W. Geis, M. E. Grein, R. T. Schulein, J. U. Yoon, D. M. Lennon, F. Gan, G.-R. Zhou, F. X. Kaertner, and T. M. Lyszczarz, "High-speed silicon electro-optical modulator that can be operated in carrier depletion or carrier injection mode," in *Optical Fiber Communication Conference* (Optical Society of America, 2008), paper CFH4.

[69] A. Novack, Y. Liu, R. Ding, M. Gould, T. Baehr-Jones, Q. Li, Y. Yang, Y. Ma, Y. Zhang, K. Padmaraju, K. Bergmen, A. E.-J. Lim, G.-Q. Lo, T. Baehr-Jones, and M. Hochberg, "A 30 GHz silicon photonic platform," in *Proceedings of IEEE 10th International Conference on Group IV Photonics* (IEEE, 2013), pp. 7-8.

[70] MODE Solutions, Lumerical Solutions Inc., https://www.lumerical.com/tcad-products/mode.

[71] E. Palik, *Handbook of Optical Constants of Solids* (Elsevier, 1998).

[72] L. Tong, J. Lou, and E. Mazur, "Single-mode guiding properties of subwavelength-diameter silica and silicon wire waveguides," Opt. Express **12**(6), 1025-1035(2004).

[73] L. Chrostowski, and M. Hochberg, *Silicon Photonics Design: From Devices to Systems*

(Cambridge University, 2015).

[74] FDTD Solutions, Lumerical Solutions Inc., https://www.lumerical.com/tcad-products/fdtd.

[75] E. Dulkeith, F. Xia, L. Schare, W. M. J. Green, and Y. A. Vlasov, “Group index and group velocity dispersion in silicon-on-insulator photonic wires,” Opt. Express **14**(9), 3853-3863(2006).

[76] DEVICE, Lumerical Solutions Inc., https://www.lumerical.com/tcad-products/device.

[77] R. Dubé-Demers, J. St-Yves, A. Bois, Q. Zhong, M. Caverley, Y. Wang, L. Chrostowski, S. LaRochelle, D. V. Plant, and W. Shi, “Analytical modeling of silicon microring and microdisk modulators with electrical and optical dynamics,” J. Lightw. Technol. **33**(20), 4240-4252 (2015).

[78] Z. Xuan, Y. Ma, Y. Liu, R. Ding, Y. Li, N. Ophir, A. E.-J. Lim, G.-Q. Lo, P. Magill, K. Bergman, T. Baehr-Jones, and M. Hochberg, “Silicon microring modulator for 40 Gb/s NRZ-OOK metro networks in O-band,” Opt. Express **22**(23), 28284-28291 (2014).

[79] L. Pavesi, and G. Guillot, *Optical Interconnects: The Silicon Approach* (Springer, 2006).

[80] B. J. Frey, D. B. Leviton, and T. J. Madison, “Temperature-dependent refractive index of silicon and germanium,” Proc. SPIE **6273**, 62732J (2006).

[81] Macom, Laser photonic integrated circuits, https://www.macom.com/products/photonic-solutions/l-pic.

[82] A. Yariv, “Universal relations for coupling of optical power between microresonators and dielectric waveguides,” Electron. Lett. **36**(4), 321–322 (2000).

[83] D. G. Rabus, Integrated Ring Resonators (Springer, 2007).

[84] J. C. Rosenberg, W. M. J. Green, S. Assefa, D. M. Gill, T. Barwicz, M. Yang, S. M. Shank, and Y. A. Vlasov, “A 25 Gbps silicon microring modulator based on an interleaved junction,” Opt. Express **20**(24), 26411-26423 (2012).

[85] J. Müller, F. Merget, S. S. Azadeh, J. Hauck, S. R. García, B. Shen, and J. Witzens, “Optical peaking enhancement in high-speed ring modulators,” Sci. Rep. **4**(1), 6310 (2014).

[86] H. Yu, D. Ying, M. Pantouvaki, J. V. Campenhout, P. Absil, Y. Hao, J. Yang, and X. Jiang, “Trade-off between optical modulation amplitude and modulation bandwidth of silicon micro-ring modulators,” Opt. Express **22**(12), 15178–15189 (2014).

[87] G. Li, X. Zheng, H. Thacker, J. Yao, Y. Luo, I. Shubin, K. Raj, J. E. Cunningham, and A. V. Krishnamoorthy, “40 Gb/s thermally tunable CMOS ring modulator,” in *Proceedings of IEEE*

9th International Conference on Group IV Photonics (IEEE, 2012), pp. 1-3.

[88] D. J. Thomson, F. Y. Gardes, D. C. Cox, J.-M. Fédéli, G. Z. Mashanovich, and G. T. Reed, "Self-aligned silicon ring resonator optical modulator with focused ion beam error correction," J. Opt. Soc. Am. B **30**(2), 445-449 (2013).

[89] D. Marris-Morini, C. Baudot, J.-M. Fédéli, G. Rasigade, N. Vulliet, A. Souhaité, M. Ziebell, P. Rivallin, S. Olivier, P. Crozat, X. Le Roux, D. Bouville, S. Menezo, F. Boeuf, and L. Vivien, "Low loss 40 Gbit/s silicon modulator based on interleaved junctions and fabricated on 300 mm SOI wafers," Opt. Express **21**(19), 22471-22475 (2013).

[90] L. Wang, R. Hu, M. Li, Y. Qiu, D. Chen, X. Xiao, Z. Li, Y. Yu, J. Yu, Q. Yang, and S. Yu, "Transmission of 24-Gb/s PAM-4 over 150-km SSMF using a driverless silicon microring modulator," in *Asia Communications and Photonics Conference* (Optical Society of America, 2014), paper ATh4D.7.

[91] O. Dubray, S. Menezo, B. Blampey, P. Le Maitre, J. F. Carpentier, B. Ben Bakir, M. Fournier, and S. Messaoudène, "20Gb/s PAM-4 Transmission from 35 to 90°C by modulating a silicon ring resonator modulator with $2V_{pp}$," in *Optical Fiber Communication Conference* (Optical Society of America, 2015), paper W2A.31.

[92] R. Ding, Y. Liu, Q. Li, Z. Xuan, Y. Ma, Y. Yang, A. E.-J. Lim, G.-Q. Lo, K. Bergman, T. Baehr-Jones, and M. Hochberg, "A compact low-power 320-Gb/s WDM transmitter based on silicon microrings," IEEE Photonics J. **6**(3), 6600608, 2014.

[93] C. Sun, M. T. Wade, Y. Lee, J. S. Orcutt, L. Alloatti, M. S. Georgas, A. S. Waterman, J. M. Shainline, R. R. Avizienis, S. Lin, B. R. Moss, R. Kumar, F. Pavanello, A. H. Atabaki, H. M. Cook, A. J. Ou, J. C. Leu, Y.-H. Chen, K. Asanović, R. J. Ram, M. A. Popović, and V. M. Stojanović, "Single-chip microprocessor that communicates directly using light," Nature **528**, 534-538(2015).

[94] P. Dong, J. Lee, Y.-K. Chen, L. L. Buhl, S. Chandrasekhar, J. H. Sinsky, and K. Kim, "Four-channel 100-Gb/s per channel discrete multitone modulation using silicon photonic integrated circuits," J. Lightw. Technol. **34**(1), 79-84 (2016).

[95] S. Agarwal, M. Ingels, M. Rakowski, M. Pantouvaki, M. Steyeart, P. Absil, and J. V. Campenhout, "Wavelength locking of a Si photonic ring transmitter using a dithering-based

OMA stabilizing feedback loop," in *Optical Fiber Communication Conference* (Optical Society of America, 2016), paper Th1F.5.

[96] X. Tu, T.-Y. Liow, J. Song, X. Luo, Q. Fang, M. Yu, and G.-Q. Lo, "50-Gb/s silicon optical modulator with travelling-wave electrodes," Opt. Express **21**(10), 12776-12782(2013).

[97] H. Xu, X. Li, X. Xiao, P. Zhou, Z. Li, J. Yu, and Y. Yu, "High-speed silicon modulator with band equalization," Opt. Lett. **39**(16), 4839-4842(2014).

[98] H.-W. Chen, J. D. Peters, and J. E. Bowers, "Forty Gb/s hybrid silicon Mach-Zehnder modulator with low chirp," Opt. Express **19**(2), 1455-1460(2011).

[99] P. Dong, L. Chen, and Y.-K. Chen, "High-speed low-voltage single-drive push-pull silicon Mach-Zehnder modulators," Opt. Express **20**(6), 6163-6169(2012).

[100] K. Okamoto, *Fundamentals of Optical Waveguides* (Academic Press, 2000).

[101] H. Yu, M. Pantouvaki, J. V. Campenhout, D. Korn, K. Komorowska, P. Dumon, Y. Li, P. Verheyen, P. Absil, L. Alloatti, D. Hillerkuss, J. Leuthold, R. Baets, and W. Bogaerts, "Performance tradeoff between lateral and interdigitated doping patterns for high speed carrier-depletion based silicon modulators," Opt. Express **20**(12), 12926-12938(2012).

[102] J.-M. Liu, *Photonic Devices* (Cambridge University, 2005).

[103] R. Ding, Y. Liu, Y. Ma, Y. Yang, Q. Li, A. E.-J. Lim, G.-Q. Lo, K. Bergman, T. Baehr-Jones, and M. Hochberg, "High-speed silicon modulator with slow-wave electrodes and fully independent differential drive," J. Lightw. Technol. **32**(12), 2240-2247 (2014).

[104] D. Marris-Morini, L. Virot, C. Baudot, J.-M. Fédéli, G. Rasigade, D. Perez-Galacho, J.-M. Hartmann, S. Olivier, P. Brindel, P. Crozat, F. Boeuf, and L. Vivien, "A 40 Gbit/s optical link on a 300-nm silicon platform," Opt. Express **22**(6), 6674-6679(2014).

[105] Y. Yang, Q. Fang, M. Yu, X. Tu, R. Rusli, and G.-Q. Lo, "High-efficiency Si optical modulator using Cu travelling-wave electrode," Opt. Express **22**(24), 29978-29985 (2014).

[106] A. D. Simard, B. Filion, D. Patel, D. V. Plant, and S. LaRochelle, "Segmented silicon MZM for PAM-8 transmissions at 114 Gb/s with binary signaling," Opt. Express **24**(17), 19467-19472 (2016).

[107] L. Zhang, J.-Y. Yang, M. Song, Y. Li, B. Zhang, R. G. Beausoleil, and A. E. Willner, "Microring-based modulation and demodulation of DPSK signal," Opt. Express **15**(18), 11564–

11569 (2007).

[108] M. Kuschnerov, F. N. Hauske, K. Piyawanno, B. Spinnler, M. S. Alfiad, A. Napoli, and B. Lankl, “DSP for coherent single-carrier receivers,” J. Lightwave Technol. **27**(16), 3614–3622 (2009).

[109] N. Eiselt, J. Wei, H. Griesser, A. Dochhan, M. H. Eiselt, J.-P. Elbers, J. J. Vegas Olmos, and I. Tafur Monroy, “First real-time 400G PAM-4 demonstration for inter-data center transmission over 100 km of SSMF at 1550 nm,” in (Optical Society of America, 2016), paper W1K.5.

[110] C.-M. Chang, P. Dong, C. Gui, and G. de Valicourt, “Low-chirp push-pull microring modulators,” in *Optical Fiber Communication Conference* (Optical Society of America, 2016), paper Th4H.2.

[111] Z. Wang, Y. Gao, A. S. Kashi, J. C. Cartledge, A. P. Knights, “Silicon microring modulator for dispersion uncompensated transmission applications,” J. Lightw. Technol. **34**(16), 3675-3681 (2016).

[112] C. Galland, A. Novack, Y. Liu, R. Ding, M. Gould, T. Baehr-Jones, Q. Li, Y. Yang, Y. Ma, Y. Zhang, K. Padmaraju, K. Bergmen, A. E.-J. Lim, G.-Q. Lo, and M. Hochberg, “A CMOS-compatible silicon photonic platform for high-speed integrated opto-electronics,” in SPIE Microtechnologies (SPIE, 2013), pp. 87670G.

[113] INTERCONNECT, Lumerical Solutions Inc., https://www.lumerical.com/tcad-products/interconnect.

[114] F. Koyama and K. Iga, “Frequency chirping in external modulators,” J. Lightwave Technol. **6**(1), 87–93 (1988).

[115] N. Courjal, H. Porte, J. Hauden, P. Mollier, and N. Grossard, “Modeling and Optimization of low chirp $LiNbO_3$ Mach-Zehnder modulators with an inverted ferroelectric domain section,” J. Lightwave Technol. **22**(5), 1338–1343 (2004).

[116] J. C. Cartledge, “Comparison of effective α-parameters for semiconductor Mach-Zehnder optical modulators,” J. Lightwave Technol. **16**(3), 372–379 (1998).

[117] APEX Technologies, Optical complex spectrum analyzer application notes, http://www.apex-t.com/optical-complex-spectrum-analyzer-application-notes/.

[118] Y. Zhang, S. Yang, A. E.-J. Lim, G.-Q. Lo, C. Galland, T. Baehr-Jones, and M. Hochberg, "A compact and low loss Y-junction for submicron silicon waveguide," Opt. Express **21**(1), 1310-1316(2013).

[119] G. Li, A. V. Krishnamoorthy, I. Shubin, J. Yao, Y. Luo, H. Thacker, X. Zheng, K. Raj, and J. E. Cunningham, "Ring resonator modulators in silicon for interchip photonic links," IEEE J. Sel. Top. Quantum Electron. **19**(6), 3401819 (2013).

[120] ITU-T Recommendation G.975.1, Forward error correction for high bit-rate DWDM submarine systems, https://www.itu.int/rec/T-REC-G.975.1-200402-I/en.

[121] IEEE P802.3bj, 100 Gb/s backplane and copper cable task force, http:// www.ieee802.org/3/bj.

[122] M. Chagnon, M. Morsy-Osman, M. Poulin, C. Paquet, S. Lessard, and D. V. Plant, "Experimental parametric study of a silicon photonic modulator enabled 112-Gb/s PAM transmission system with a DAC and ADC," J. Lightwave Technol. **33**(7), 1380–1387 (2015).

[123] L. G. Cohen, "Comparison of single-mode fiber dispersion measurement techniques," J. Lightwave Technol. **3**(5), 958-966 (1985).

[124] G. Agrawal, *Lightwave Technology: Telecommunication Systems* (John Wiley, 2005).

[125] M. Chagnon, M. Morsy-Osman, M. Poulin, C. Latrasse, J.-F. Gagné, Y. Painchaud, C. Paquet, S. Lessard, and D. V. Plant, "Experimental study of 112 Gb/s short reach transmission employing PAM formats and SiP intensity modulator at 1.3 μm," Opt. Express **22**(17), 21018-21036 (2014).

[126] H. Yun, W. Shi, Y. Wang, L. Chrostowski, and N. A. F. Jaeger, "2×2 adiabatic 3-dB coupler on silicon-on-insulator rib waveguides," Proc. SPIE, Photonics North 2013 **8915**, 89150V (2013).

[127] D. Taillaert, H. Chong, P. I. Borel, L. H. Frandsen, R. M. De La Rue, and R. Baets, "A compact two-dimensional grating coupler used as polarization splitter," IEEE Photon. Technol. Lett. **15**(9), 1249-1251 (2003).

[128] F. Boeuf, C. Crémer, N. Vulliet, T. Pinguet, A. Mekis, G. Masini, L. Verslegers, P. Sun, A. Ayazi, N.-K. Hon, S. Sahni, Y. Chi, B. Orlando, D. Ristoiu, A. Farcy, F. Leverd, L. Broussous, D. Pelissier-Tanon, C. Richard, L. Pinzelli, R. Beneyton, O. Gourhant, E. Gourvest, Y. Le-Friec,

D. Monnier, P. Brun, M. Guilleermet, D. Benoit, K. Haxaire, J. R. Manouvrier, S. Jan, H. Petiton, J. F. Carpentier, T. Quémerais, C. Durand, D. Gloria, M. Fourel, F. Battegay, Y. Sanchez, E. Batail, F. Baron, P. Delpech, L. Salager, P. De Dobbelaere, and B. Sautreuil, "A multi-wavelength 3D-compatible silicon photonics platform on 300nm SOI wafers for 25Gb/s applications," in *Proceedings of IEEE International Electron Devices Meeting* (IEEE, 2013), pp. 13.3.1-13.3.4.

[129] P. Dong, C. Xie, L. Chen, L. L. Buhl, and Y.-K. Chen, "112-Gb/s monolithic PDM-QPSK modulator in silicon," Opt. Express **20**(26), B624-B629 (2012).

[130] X. Wu, C. Huang, K. Xu, W. Zhou, C. Shu, and H. K. Tsang, "3 × 104 Gb/s single-λ interconnect of mode-division multiplexed network with a multicore fiber," J. Lightw. Technol. **36**(2), 318-324 (2018).

[131] M. O'Sullivan, "Progress of digital coherent optical communication systems," in Conference on Lasers and Electro-optics (Optical Society of America, 2017), paper STu3M.5.

[132] C. Doerr, J. Heanue, L. Chen, R. Aroca, S. Azemati, G. Ali, G. McBrien, L. Chen, B. Guan, H. Zhang, X. Zhang, T. Nielsen, H. Mezghani, M. Mihnev, C. Yung, and M. Xu, "Silicon photonics coherent transceiver in a ball-grid array package," in *Optical Fiber Communication Conference* (Optical Society of America, 2017), paper Th5D.5.

[133] P. Dong, X. Chen, K. Kim, S. Chandrasekhar, Y.-K. Chen, and J. H. Sinsky, "128-Gb/s 100-km transmission with direct detection using silicon photonic Stokes vector receiver and I/Q modulator," Opt. Express **24**(13), 14208-14214 (2016).

[134] Z. Xing, D. Patel, T. Hoang, M. Qiu, R. Li, E. El-Fiky, M. Xiang, and D. V. Plant, "100Gb/s 16-QAM transmission over 80 km SSMF using a silicon photonic modulator enabled VSB-IM/DD system," in *Optical Fiber Communication Conference* (Optical Society of America, 2018), paper M2C.7.